MULTISCALE CHARACTERIZATION OF ALPHA-BETA TITANIUM ALLOYS USING HIGH-THROUGHPUT SPHERICAL INDENTATION TEST PROTOCOLS

A Dissertation
Presented to
The Academic Faculty

By

Natalia Millan Espitia

In Partial Fulfillment
of the Requirements for the Degree
Doctor of Philosophy in the
Georgia W. Woodruff School of Mechanical Engineering

Georgia Institute of Technology

December 2021

MULTISCALE CHARACTERIZATION OF ALPHA-BETA TITANIUM ALLOYS USING HIGH THROUGHPUT SPHERICAL INDENTATION TEST PROTOCOLS

Approved by:

Dr. Surya R. Kalidindi, Advisor
George W. Woodruff School of Mechanical Engineering
Georgia Institute of Technology

Dr. Richard W. Neu
George W. Woodruff School of Mechanical Engineering
Georgia Institute of Technology

Dr. David L. McDowell
George W. Woodruff School of Mechanical Engineering
Georgia Institute of Technology

Dr. Adam L. Pilchak
Materials Resources, LLC

Dr. Hamid Garmestani
School of Materials Science and Engineering
Georgia Institute of Technology

Date Approved: December 2nd, 2021

Dedicado a mi Bela y mamá, por siempre ser mi más grande apoyo y ejemplo.

Acknowledgements

I would like to express my deep gratitude to my research advisor, Dr. Surya Kalidindi, for giving me the honor of doing research under his guidance. His sincerity, motivation and scientific approach were crucial elements of inspiration in the accomplishment of this task. I also wish to thank the rest of my committee, Dr. McDowell, Dr. Garmestani, Dr. Neu and Dr. Pilchak for their contribution and feedback on my work. My gratitude to the National Science Foundation FLAMEL program, and the Air Force Research Laboratory MLP program, for supporting this research.

Especially thankful with Dr. Adam Pilchak for sharing with me part of his vast knowledge on titanium and titanium alloys, with Glenda Johnson from the Mechanical Engineering Department for her invaluable support beyond her duties, and with Dr. Ali Khosravani and Dr. Soumya Mohan for their countless hours of guidance by my side. I extend my appreciation to all the Mined group members who, in one way of another, made of this experience a memorable one.

Lastly, I am forever beholden to my family for their prayers and caring towards my education and future. Whether on earth or heaven, they have always provided me with the continuing love, support and momentum to keep dreaming.

Table of Contents

List of Tables

List of Figures

Summary

Traditionally, new materials follow well stablished paths from their manufacturing beginnings to their final application. Development, evaluation, certification and deployment are some of the steps in these processes. However, some of these stages are characterized for very specialized protocols, resulting in prolonged timelines from beginning to end. The design process of materials can sometimes be defined as ambiguous due to the lack of fundamental knowledge at salient length-scales. This can be attributed to the absence of trustworthy testing methods that provide meaningful and reliable knowledge on the behavior of materials at length-scales over different orders of magnitude. In addition to this characteristic, cost and time efficiency are also crucial attributes in the materials design field, as large amounts of data covering wide ranges or parameters provide stronger bases for physics-based models that can reverse-engineer the whole process.

This work presented in this dissertation evaluates spherical nano-indentation protocols as a high-throughput approach for the mechanically characterization of several α- and α/β titanium alloys at the grain-scale level. Chapter 3 explores the mechanical response of primary-α grains, and their dependence on the HCP lattice orientation and the corresponding grain chemical composition. Chapter 4 delves into the mechanical behavior of single grains in fully basket-weave titanium microstructures. By looking into the grain responses, a reduction on the multiple microstructural features in this type of morphologies is accomplished, leading to better statements of the influence of lath-microstructure and α-lath orientations on the indentation properties. This work is accompanied by a thorough microstructural characterization/quantification of the basket-weave morphology that is

later subjected to a dimensionality reduction for a simplified understanding. And finally, Chapter 5 aims to bridge multiresolution indentation measurements form a bimodal titanium microstructure for the subsequent evaluation of composite theories in the prediction of the effective indentation yield.

CHAPTER 1 Introduction

1.1. Titanium Alloys and its Applications

The critical need for innovative materials with higher strength-to-weight ratios led to an innate interest in the study of titanium and its alloys. Apart from the exceptional specific strength of this group of alloys, corrosion and creep resistance, fatigue strength, biocompatibility and high melting temperatures open a wide range of applications. About 40% of titanium is used in aerospace industry, with the rest of it having important roles in the automobile, chemical plants and medical industries. For structural components with holes, threads, and sharp edges, titanium's notch sensitivity is certainly a property of interest. Additionally, the low ductile-to-brittle transitions temperatures of titanium alloys have also made of titanium a key resource for cryogenic vessels and components.

With up to 70% of steel's strength, but only 60% of its density, and better corrosion resistance and thermal conductivity, titanium alloys often outpace steels, aluminum and magnesium alloys in performance scenarios where low-weight/high-strength and cost-effective attributes are desired. It can be said with good confidence that the performance and service life of titanium, usually surpasses the overall cost of its processing. The use of titanium alloys has been growing at a remarkable rate, not only due to their outstanding properties, but also because of the more recent advances in the extraction and processing of pure titanium, which for a long time, made the use of this metal a very expensive option [8, 9].

Figure 1 compares the specific strength and fatigue properties of titanium alloys, among a variety of structural and metal alloys, where this metal is observed to excels in both

properties. However, titanium alloys cover a bast range of properties combinations, which can be attributed to their complex multiphase microstructures and the many possible alloying elements.

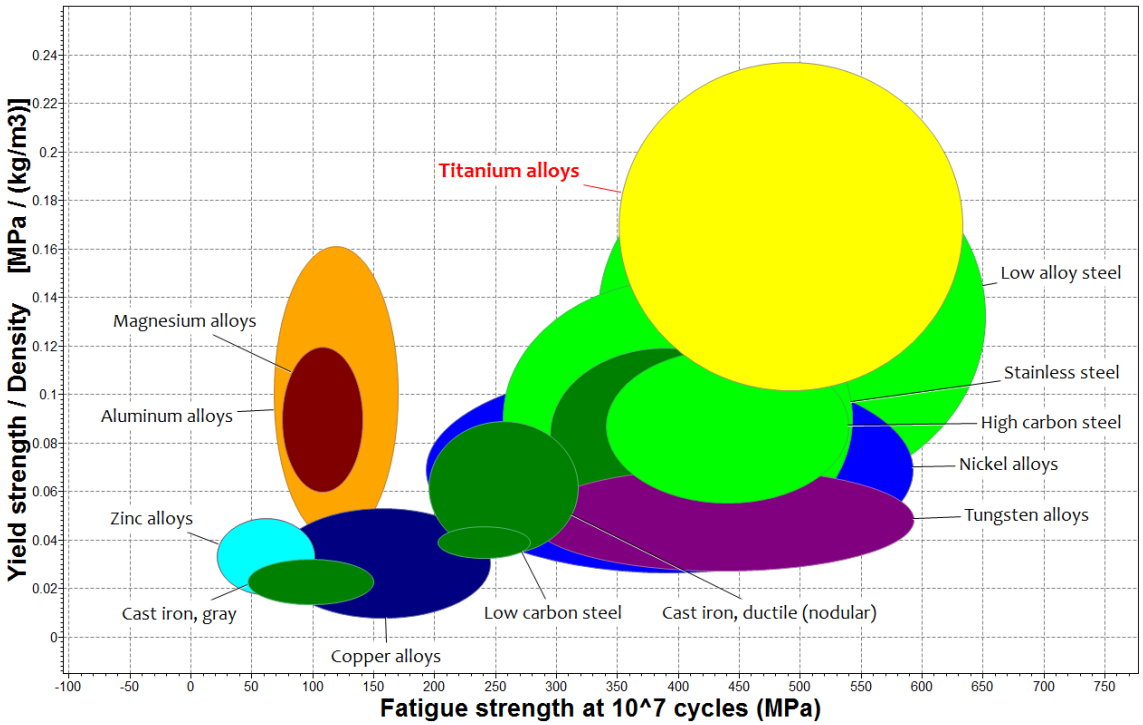

Figure 1. *Ashby plot comparing the specific strength and fatigue properties for different structural metals.*

The key to understanding and manipulating the outstanding properties of titanium, lays is deciphering how the morphology, volume fraction and individual properties of the two phases α and β influence the resulting behavior of the material. The present work aims to strengthen and build new paths for such knowledge by measuring, quantifying and visualizing mechanical and microstructure characteristics for varying ranges of chemical compositions, morphologies and length scales. A variety of recently developed experimental protocols, data analysis approaches and computational models will be conveniently employed to achieve this objective.

1.2. Hierarchical Structure of Advanced Materials

Structure and performance hierarchy is a common characteristic of biological and advanced structural materials. This refers to the recognition of salient features at different length scales of the material, which are associated with their respective set of performance properties [10]. One of the great advantages of this type of microstructures is the ability to engineer their properties for a specific application by modifying the processing history and therefore their underlying microsuede features at different length scales [11, 12]. In the case of titanium alloys, of relevance in this dissertation, the length scale classification starts at the atomic scale with the crystal structure arrangement of atoms constituting each individual phase. Subsequently, the continuous assembly of large number of same-type-lattices into volumes, forms either α or β grains which, arranged one next to the other in the form of laths, constitute regions of uniform of phase orientations known as colonies. Finally, the distribution of multiple orientation colonies forms the largest of the length scales in these metallic alloys. A schematic of a titanium alloy microstructure hierarchy can be observed in ***Figure 2***.

Above certain length scale, which we'll refer to as the Representative Volume Element (RVE) of a microstructure, the material is observed to exhibit stable values of the mechanical properties. At this point we can assume the microstructure to behave as a homogeneous medium.

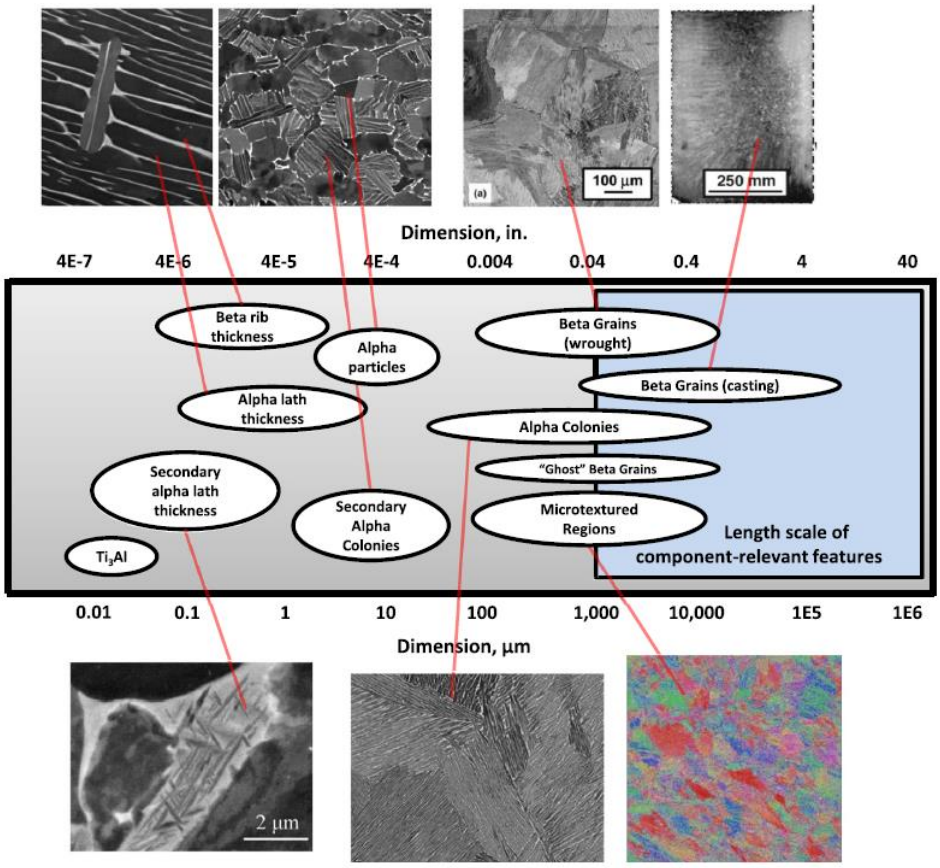

Figure 2. *Illustration of the hierarchical microstructure of a titanium alloy [3].*

1.3. Mechanical Characterization of Structural Alloys

Traditional mechanical testing of structural materials comprise tension, compression, bending, hardness and fatigue testing, among many others. Many of these protocols have been utilized at different length scales from the nano-constituent to the macroscale levels [13-16].

Micropillar compression testing for example [17-21], resembles a uniaxial compression test in the stress field imposed on the sample. The small testing specimens (dimensions in microns)are fabricated with highly specialized (i.e., cost and timely expensive) Focused

Ion Beam (FIB) processes, which have been associated with process induced surface damage that lessens the veracity of the results [22].

On the other hand, hardness measurement require very standard sample preparation protocols (i.e., grinding and polishing) that are wide used in various metallography processes. Several types of hardness testing protocols have been established, for which their main difference relies on the tip geometry and the analysis protocols (e.g., Vickers, Berkowich, Brinell, Rockwell, Knoop) [23]. These experiments are based in the measurement of load and displacement from a monotonic deformation test on the sample. Differences in the analysis protocols lay on the calculation of contact area [24, 25], associations between hardness and uniaxial strength values [26] and between the load-displacement curves and the equivalent uniaxial properties [27-29]. The main deficiency with the hardness measurements is that they do not represent an intrinsic material property (e.g., the measured values depend on the imposed load/displacement levels [30-33]). In general, they correspond to the material flow stress after some non-standard amount of plastic deformation has been applied to the material. Additionally, the use of sharp indenters (i.e., Vickers, Berkowich) occurs in large stress fields in the material, resulting in the rapid induction of permanent deformation. This leads to an enormous difficulty in capturing elastic properties, such as the elastic modulus, from these testing procedures. Thus, the representation of a materials behavior by a unique harness measurement, could be seen as an oversimplification.

A special case in these nanoindentation methods are the spherical indentation protocols developed by Kalidindi and Pathak [34] in which the whole load-displacement curve is converted into an indentation stress-strain (ISS) curve (detailed explanation of this protocol

is presented in section 2.1) and will be used for the mechanical characterization of the here presented work results. These protocols have been shown to provide equivalent properties to those obtained from uniaxial tensile testing at the nano and micro scales. Results from these protocols have been observed to be consistent and highly efficient as they are considered of high-throughput fashion.

More recently, the newly developed Small Punch Testing (SPT) protocols by Leclerc et al. [35], coupled with Finite Element Model (FEM) simulations of the experiment, have demonstrated to predict stress-strain curves of a variety of materials all the way to failure. This capability is of great interest as it captures ultimate tensile strength and ductility properties which indentation analysis lacks. Additionally, these experiments and predictions are very cost and time efficient due to the simple sample preparation steps and short time required for the experiment and analysis.

1.4. Research Objectives

The present study has as objective the multiscale mechanical and microstructure characterization of alpha, near-alpha and alpha-beta titanium alloys for the exploration of their dependence on crystal orientation, chemistry and lath microstructure at different length scales. Milestones for the achievement of this goal are of this objective are organized into three tasks as follows.

1.4.1 Task 1

High-Throughput Grain-Scale Mechanical Characterization of Primary-α Phase

Tasks 1 will evaluate the high-throughput mechanical properties (i.e., indentation modulus and indentation yield) of the primary-alpha phase grains for five different titanium alloys. Spherical nano-indentation, accompanied by Electron Backscattered Diffraction (EBSD), will be used for the crystal lattice orientation and crystal specific chemical composition on the mechanical behavior of the alloys of interest, and to enhance our current understanding of the solid solution strengthening mechanisms.

- Design of heat treatment for each chemistry to produce large α-phase grains.
- Grain-scale characterization of elastic and plastic properties as a function of the crystal orientation.
- Measurement of the α-phase chemical composition with special attention to oxygen content.

1.4.2 Task 2

High-Throughput Grain-Scale Mechanical and Microstructure Characterization of Fully Basket-Weave Morphologies

Task 2 also employs spherical nano-indentation for the mechanical characterization of fully basket-weave microstructures, and conducts microstructure characterization/ quantification by means of digital image segmentation, spatial correlations and Principal Component Analysis (PCA). This work will present a refinement of the current knowledge on the role played by the lath microstructure onto the mechanical behavior of basket-weave morphologies.

- Design of heat treatment to obtain a variety of basket-weave lath microstructures for all alloys.
- Grain-scale mechanical characterization of basket-weave crystals using nanoindentation protocols.
- Microstructure characterization and quantification of the different lath structures using digital image segmentation techniques and spatial correlations.

1.4.3 Task 3

Multiresolution Spherical Indentation of a Bimodal Titanium Alloy

Task 3 will comprise the macro-scale mechanical characterization of one bimodal microstructure (primary-α and basket-weave grains) using spherical nano-indentation with two different indenter tips for the measurement of constituent level and bulk mechanical properties. In conjunction with the corresponding microstructure characterization and quantification, a series of data-based composite theories will be considered for the prediction of the indentation yield of the specimen.

- Design of heat treatment that simulate the processing conditions leading to common microstructures used in industry.
- Mechanical characterization of the individual constituents in the bimodal microstructure using spherical nanoindentation.
- Mechanical characterization of the bulk/macro-scale properties using spherical indentation protocols.

- Microstructure characterization and quantification of the bimodal structures using digital image segmentation techniques and spatial correlations.
- Evaluation of a composite theorie for the prediction of effective properties based on the grain-level measurements.

CHAPTER 2 Background

2.1 Mechanical Characterization

2.1.1 Kalidindi and Pathak's Indentation Stress-Strain Protocols

In an effort to address the mechanical characterization difficulties described above, Kalidindi and Pathak [34, 36] have developed and demonstrated novel measurement and analysis protocols based on the Hertzian theory of contact [37], for the extraction of the normalized mechanical response of the material in the form of indentation stress-strain curves that exhibit a linear elastic regime and a clear transition to the elastic-plastic regime [34]. With smoother stress fields compared to sharp indentation, these protocols have been shown to successfully capture the normalized elastic-plastic responses of the material (in the form of meaningful indentation stress-strain curves) at multiple material length scales [5, 38-44]. For grain-scale measurements, these protocols have been shown to produce highly consistent and reproducible measurements that can be correlated to the grain orientation in selected cubic metals [39, 43, 44] and hexagonal metals [5, 41]. And for macro-scale measurements, comparable to tensile experiments, their versatility has been demonstrated by their application over a wide variety of materials groups such as ceramic composites, metals, bulk metallic glass composites, polymer composites, among many others [45-48]. Furthermore, in a few cases, the indentation properties extracted from these measurements have been successfully used to estimate the intrinsic grain-scale material properties such as the single crystal elastic stiffness parameters as well as the CRSS values [49-51].

These capabilities are possible due to the accurate determination of the load-displacement segment corresponding to the elastic deformation of the material. This is accomplished by applying a zero-point correction to the data where the values corresponding to the zero-load and zero-displacement represents the beginning of the deformation in accordance with the Hertzian theory. This step is necessary as unavoidable artifacts on the surface of the material, such as surface roughness or oxide layers, result in the very initial portion of the curve to significantly deviate from the ideal deformation behavior, leading to an erroneous value of the elastic property. This value is crucial in the calculation of the contact radius along the deformation process, and therefore for the corresponding indentation stress and strain values. Calculation of the contact area has been of great importance in the calculation of hardness values in an effort to predict more standard strength properties. Several methods have been previously explored in which power-laws [52-55] and second order polynomials [56, 57] are fit to the initial segments of the load-displacement, and others that propose experimental setups [58-60] in order to accurately measure the evolving contact radius.

The protocols proposed by Pathak and Kalidindi [34] rely on a series of unloading cycles along the load-displacement indentation curve for the measurement of the contact radius. These loading-unloading cycles can be systematically applied by the equipment, or manually set up by the user depending on the devise being used for the experiment. The Nano-indenter G200 by Keysight (formerly Agilent) for example, offers an independent measurement known as the Continuous Stiffness Measurement (CSM) [36] which superimposes sinusoidal loading-unloading cycles and outputs the slope of those unloading segments ($S = dP/dh$, where P and h denote the measured load and measure

displacement). Additional details on the analysis protocol using this signal are provided in the following section. When using other nanoindentation machines that lack such capability, elastic unloading segments are manually imposed along the deformation experiment [61]. These segments are then carefully analyzed using Hertz's theory to determine the contact radius at that specific point. During the first part of the analysis, where the elastic segment of the material is estimated, the radius of the material is assumed to be infinite. However, when analyzing the unloading portions of the experiment, this assumption is no longer valid as some degree of plastic deformation has already been imposed on the sample. Each unloading segments is fit to the Hertz relationship between the total indentation depth, h_t, and the load, P.

$$h_e = h_t - h_r = kP^{2/3} \quad 1)$$

From Eq. (4), h_e is the elastic indentation depth, h_r is the residual (or plastic) indentation depth, which are found by regression analysis on the unloading segments. In this protocol, each unloading curve produces only one point on the indentation stress-strain curve, meaning that a considerable number of load-unload cycles is needed to build a complete description of the deformation process of the sample.

The versatility and fidelity of these protocols have been demonstrated by conducting experiments with different tip sizes when geometrically possible [5, 41, 44, 62, 63], by comparing the results to data from other testing protocols [40, 46, 48, 64], as well as with simulations of the spherical indentation experiments [65, 66].

2.1.2 Nanoindentation

As previously mentioned, these protocols are largely based on Hertz's theory [37], which describes the relationship between the indentation load (P) and the elastic indentation depth (h_e) as

$$P = \frac{4}{3} E_{eff} R_{eff}^{1/2} h_e^{3/2} \quad (2)$$

$$\frac{1}{E_{eff}} = \frac{1}{E_{ind}} + \frac{1 - \nu_i^2}{E_i} \quad (3)$$

$$\frac{1}{R_{eff}} = \frac{1}{R_s} + \frac{1}{R_i} \quad (4)$$

where E_{eff} and R_{eff} denote the effective indentation modulus and radius of the indenter-sample system, respectively, and E_{ind} denotes the sample's effective indentation modulus. In Eq. (2), E_i and ν_i denote the indenter's Young's modulus and Poisson ratio, respectively, while R_s and R_i denote the radii of the sample and indenter surfaces, respectively (see ***Figure 1(a, b)*** for some of the definitions).

A distinctive feature of the ISS protocols employed in this work is that the very small elastic regime in the initial contact is analyzed to establish the sample's effective indentation modulus (i.e., E_{ind}). Reliable estimation of this parameter is critical for the successful application of the spherical indentation stress-strain protocols discussed here. For this analysis, the sample surface is assumed to be initially flat, i.e., $R_s = \infty$ and $R_{eff} = R_i$. The central challenges in the application of Hertz's theory (Eqs. (1)-(3)) to the initial elastic loading regime come from the tremendous difficulties associated with reliably

identifying a segment of the load-displacement curve corresponding to this initial purely elastic regime. In fact, our interest is only in identifying a segment in this initial elastic regime, not necessarily the entire initial elastic loading segment. Specifically, the following challenges are encountered: (i) this segment is very small in many, (ii) unavoidable sample surface conditions such as oxide layers and surface roughness make it very difficult to precisely identify the start of this segment, and (iii) the transition from the elastic regime to the elastic-plastic regime is extremely smooth in the load-displacement curves making it impossible to visually discern an endpoint of this initial elastic segment.

The analyses of the initial elastic loading starts with a zero-point correction [36, 48, 52, 56, 59, 67], which identifies an effective point of initial contact from which the measured load-displacement curve conforms well with Hertz's theory (). It should be noted that the point of actual contact between the indenter and the sample surface shows high sensitivity to sample surface characteristics such as roughness and oxide layers, and therefore is not reliable for analyses with Hertz's theory. Instead, we identify a segment of the initial loading segment (highlighted in red in ***Figure 3(b)***) that is consistent with Hertz's theory by requiring that the zero-point corrected signals of load and displacement are consistent with the independent CSM (continuous stiffness measurement) signal , which is unaffected by the zero-point correction. This requirement is expressed as

$$S = \frac{3P}{2h_e} = \frac{3\left(\tilde{P} - P^*\right)}{2\left(\tilde{h} - h^*\right)} \qquad 5)$$

where $\tilde{P}$ and $\tilde{h}$ denote the measured indentation load and indentation displacement, respectively, P^* and h^* denote their corresponding zero-point corrections, respectively, and S denotes the CSM signal. In the modern nanoindenters, CSM is performed by superimposing sinusoidal loading-unloading cycles of 2 nm amplitude and 45 Hz frequency on the monotonic loading [68, 69]. Values of P^* and h^* are established using standard regression techniques to fit the measurements to Eq. (4). This regression fit also identifies a suitable initial elastic segment [34] that is fully consistent with Hertz's theory, which is then analyzed using Eq. (1) to estimate E_{eff}.

The next step in the extraction of the ISS curves is the estimation of the evolving contact radius a (see ***Figure 3(a)***) in the entire loading segment (including the elastic-plastic regime) [34, 36]. Several studies in current literature [70-72] have utilized calibrated area functions that implicitly ignore the dependence of the contact area on the elastic properties of the sample material. This leads to a fundamental inconsistency in the application of Hertz's theory. In the protocols used in this work, the contact radius is estimated using Hertz's theory on the unloading elastic stiffness measured by the CSM. This is accomplished using the following expression:

$$a = \frac{S}{2E_{eff}} \tag{6}$$

where the value of E_{eff} is assumed to be constant throughput the entire loading history. This is a reasonable assumption because the averaged plastic strain in the deformation zone under the indenter is typically very small, and such small plastic strains under the indenter will not significantly alter the effective elastic properties in the deformation zone under the

indenter within the single grain. The estimation of the evolving contact radius throughout the imposed elastic-plastic indentation history allows for the continuous estimations of indentation stress, σ_{ind}, and indentation strain, ε_{ind} [73, 74], as

$$\sigma_{ind} = \frac{P}{\pi a^2} \quad 7)$$

$$\varepsilon_{ind} = \frac{4}{3\pi}\frac{h_t}{a} \approx \frac{h_t}{2.4a} \quad 8)$$

It should be noted that the indentation strain defined in Eq. (7) is the total (averaged) indentation strain in the primary deformed zone under the indenter. For the initial elastic loading, Eqs. (6) and (7) convert the Hertz's original nonlinear relationship between the indentation load and indentation displacement (see Eq. (1)) into a linear relationship between indentation stress and indentation strain with a slope of E_{ind}. Beyond the initial elastic loading, these definitions produce a normalized material response in the form of an ISS curve (see ***Figure 3(b)-(e)***) that exhibit the expected features. For example, there is a clear transition from the elastic response to an elastic-plastic response. This allows us to define an indentation yield strength, Y_{ind}, as the indentation stress at 0.2% offset indentation plastic strain. The application of this protocol has been widely reported in previous studies [5, 39, 41, 44, 75, 76] and can be visualized in ***Figure 3(c)***. Due to the very small volumes undergoing the initial plastic deformation in these tests and the annealed condition of the tested samples, pop-ins [30, 44, 77-81] are seen in some of the tests.

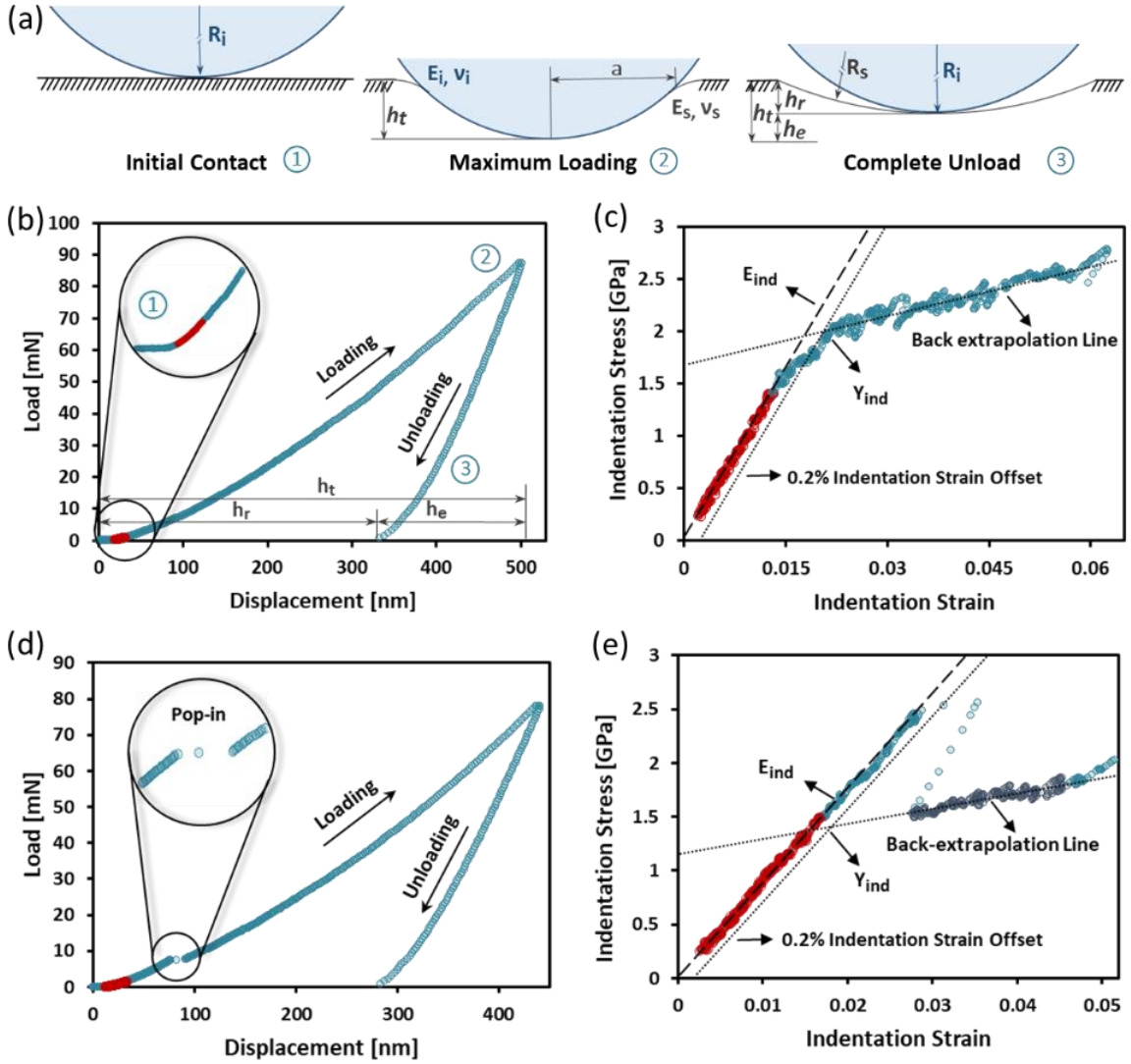

Figure 3. *a) Schematic description of the spherical indentation experiment at three different stages along the loading-unloading process. b) Measured load-displacement curve from a typical spherical indentation measurement, with a zoomed view of the early loading segment. c) Indentation stress-strain (ISS) curve corresponding to the load-displacement measurement in (b). d) Measured load-displacement curve from a spherical indentation measurement showing a clear pop-in. e) ISS curve corresponding to the load-displacement measurement in (d). The segments in the load-displacement curves selected for the elastic analyses are shown in red.*

Pop-ins cause sudden strain bursts and have been attributed to the difficulty of establishing potent dislocation sources (e.g., Frank-Reed sources) within the very small deformation zone under the indenter; these are essential for initiating plastic strain under the indenter. These are often unavoidable in annealed metal samples and make difficult the estimation of the indentation yield strength from the measured ISS responses. Prior work [44, 63] has shown that the likelihood of the occurrence of pop-ins decreased with larger indentation zone sizes (larger indenter radius), and with the higher dislocation densities in the sample (deformed materials, different surface finish). In prior work [5, 39, 43, 44, 48, 62, 63, 75], a back-extrapolation protocol (see ***Figure 3(e)***) was employed to facilitate the robust estimation of the indentation yield strength for small pop-ins. This protocol has been validated in prior work [44, 63]. For consistency, the same back-extrapolation approach is used in the present work on all samples, irrespective of whether pop-ins occurred or not.

2.2 Microstructure Characterization

A crucial part in the understanding of the physics involved in the deformation of materials, is the role of the material's microstructure. Microstructure of metals, for example, typically depicts features of interest such as grains, grain boundaries, thermodynamic phases, precipitates, among many other. These features normally span over a few length scales, and are associated with their unique set of mechanical properties. The quantities of the features present in a specific microstructure, their geometries, and their spatial arrangements, have been found to determine the properties of different material

systems [47, 82-86]. Microstructure is typically captured by means of optical or electron microscopy [87-89] and later processed over a series of computational steps to label each relevant feature of interest and to obtain important statistical information [90-93]. This process is referred to as Image Segmentation, and is more specifically defined as the process of designating each pixel (in 2D microstructures) or voxel (in 3D microstructures) as an element of a feature of interest or a local state. The sequence of steps used during the segmentation process substantially influences the resulting quantification of microstructure, and therefore the understanding of the deformation behavior itself. This type of information is later used for the construction of physics-based models such as composite theories, or more computational models such as structure-process-property linkages, which will carry with them any inaccurate information that was induced over any of the image processing steps [38, 64, 94-96].

2.2.1 Image Acquisition

The main objective in the image acquisition process, is to optimize the data collection parameters to minimize the digital processing of the images during the segmentation step. We can identify three main topics of interest in this task. The first topic refers to the selection of the microscopy technique that will provide the best quality and the larger amount of useful microstructural information. Each approach provides a different type of information regarding the material's internal or topographical structure, depending on the interaction with the specimen. Some of these techniques are optical microscopy, electron microscopy, scanning probe microscopy, x-ray, among many others.

Optical microscopy for example is one of the most common and simple techniques, however, spatial resolution is quite poor compared to other approaches (about 1μm). Scanning electron microscopes (SEM) on the other hand, provide a much better resolution due to the implementation of an electron beam to image the sample instead of a beam of light. Withing this group, three different detectors are frequently used: Secondary electron detector (SE), which provides a topographic image of the sample, backscattered electron detector (BSE), provides more of a relative mass comparison between the different components or constituents and their respective compositions, and electron backscatter diffraction detector (EBSD), that gives crystallographic information about the microstructure of the specimen [97]. From these techniques, the one that provides a stronger contrast between the features of interest must be selected. Something important to mention is that, for any of the previously mentioned techniques, sample preparation, user experience (calibration of the equipment and adjustments of the image collection specifications) and equipment type, are very important parameters that will directly impact the quality of the resulting micrographs.

The second topic pertain to the correct selection of the spatial resolution of the images, where resolution can be understood as the number of pixels representing one particular feature, or as the physical length represented by a single pixel in the image [98]. For our purpose, we wish to collect images with high resolution (e.g., larger number of pixels per feature, or smaller physical representation of a pixel) to increase accuracy and quality in the segmented images and to decrease the amount of detail lost in the process. Examples of a high-resolution image depicting very detailed microstructure features (to the left)

compared to a lower resolution one (to the right) are presented in ***Figure 4(a)*** and ***Figure 4(b)***.

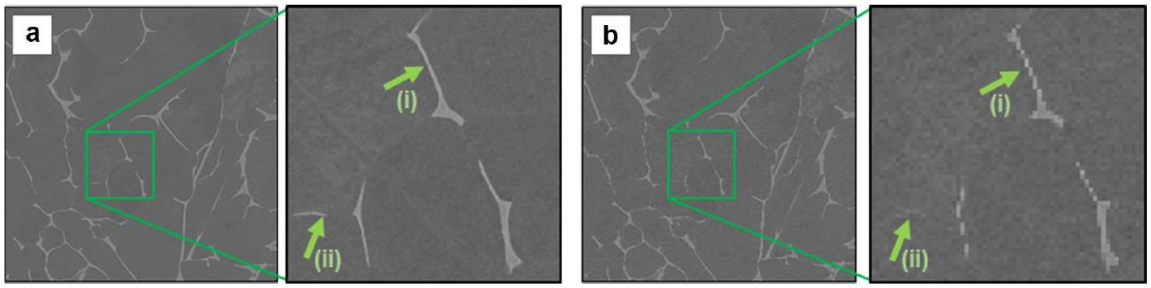

Figure 4. *Comparison between images of the same area and view-fields but with different resolutions. a) High-resolution image (0.05 µm/pixel) and b) low-resolution image (0.2 µm/pixel). [4].*

The third and last topic refers to a proper selection of the image view-field that is representative of the material's microstructure (i.e., physical area captured in the image). In this process, the microstructure statistics such as volume fractions of precipitates and phases, should be captured in such a way that they become insensitive to the view-field selection. Ideally, the selection protocol of the view-field should be systematic and assisted by more sophisticated statistics such as 2-point spatial correlations [99]. In addition to the size of the image, these scans should also capture the microstructural variations across the overall sample surface. Generally, these images should be collected randomly for a more complete statistical representation of the specimen [99, 100].

An important task for the equipment operator is the ability to simultaneously optimize all of the previously mentioned tasks. Due to the scanning nature of electron microscopes for example, a higher spatial resolution implicates that the electron beam spends a larger amount of time to scan a fixed area. In addition to this, the scanning of representative

volumes of material incurs is significant amounts of time that may not be seen as practical from the experimental point of view.

2.2.2 Image Segmentation

The main objective in image segmentation is the correct labeling of each pixel (or voxel in 3D) in a microscopy image with a microstructural local state. Due to the many image processing tools, sequences in which they can be arranged, microstructure types, and users' expertise, it is very challenging to select an image segmentation algorithms that can be applied to large numbers or data sets [4, 88, 91, 92, 101, 102]. For this reason, segmentation is commonly associated to be a quite tedious and time-consuming step in microstructure characterization, and are commonly custom-made for a specific material or group of specimens.

Current approaches employ many of the functions available in image processing toolboxes from widely available software packages such as MATLAB [103] and Python [104]. Many of these function are specially designed to solve some of the most common challenges with this kind of micrographs, and ultimately, the familiarity and expertise of the user with these functions is what determines the accuracy and results from the segmentation process.

The microstructure characterization protocol adopted for the present work is based on the segmentation framework by Iskakov and Kalidindi [4] that proposes five sequential steps with certain degree of adaptation for each microstructure type. These steps are sample preparation, image acquisition, segmentation, post-processing and evaluation/validation of the segmentation process, and a deeper explanation of the last three steps is presented next.

Inadequate sample preparation techniques and deficient equipment use/capabilities may result in microscopy images to contain different levels of noise and/or poor contrast due to artifacts such as surface roughness and resolution limits [91, 92, 97, 98, 101, 105-108]. Noise can be subdivided into global noise and local noise, where the former is frequently caused by equipment setup and protocol and be identified as a shadow across the whole image. This kind of noise can be removed by subtracting an approximated global noise function (e.g., polynomial function, second-order polynomial or Fast Fourier Transform (FFTs) filtering) from the original image or by estimating the global noise that minimizes the entropy in the amended image [109-111]. Local noise refers to the noise randomly dispersed all over the image (e.g., salt-and-pepper- noise). The main goal here is then to successfully remove such noise without unintentionally discarding valuable microstructural detail contained in the image (e.g., tiny precipitates). Different algorithms have been proposed to address these challenges in effective ways [112-115], and vary depending on the pixel-neighborhood being analyzed. Pixel-based filtering refers to a situation in which the value of a single pixel can be modified based on the pixels immediately surrounding it (gaussian, bilateral, median filters), and patch-based filters utilize information collected from different neighborhoods of the same size from different locations over the image, to modify a smaller patch of pixels (non-local means, NLM) [116]. Some of the MATLAB functions that will accomplish the previously mentioned approaches are `imgaussfilt`, `imbilatfilt`, `medfilt2` and `imnlmfilt` [103].

The next step in preparation for segmentation is the contrast enhancement of the microstructure image. This step is specifically targeted towards the enhancement of the features of interest to improve the segmentation results. Similar to the previous step, global

and local corrections are also available. Global adjustments are accomplished by modifying the range over which the histogram of the original image spans, and can be of contrast stretching or histogram equalization type [117]. Contrast stretching adjustment first expands the histogram into a wider range, and then "saturates" a specified percentage of the extremes in this new range. By widening the histogram range, we are increasing the intensity difference between different pixels in the image, while saturation accentuates the extremes of the range even more to enhance the distinction between the main features in the microstructure. One disadvantage is that this contrast enhancement is applied to the whole image, meaning than any remaining noise will be accentuated as well. One way to avoid this issue is with the implementation of localized methods in which both intensities and spatial context in the image are taken into account in the adjustment. Contrast-limited adaptive histogram equalization (CLAHE) [118] for example, modifies the histogram from a subregion in the image to match a predetermined histogram distribution. This approach protects relatively uniform areas of the image from getting affected by the undesired noise intensification. Some of the MATLAB functions commonly used for this step are `imadjust`, `histeq`, `adapthisteq` and `imsharpen` [103].

During the segmentation process, the objective is to identify and assign each label to a microstructure constituent or local state [119]. Although numerous segmentation protocols have been proposed [90, 91, 120-124], in general this task is generally achieved by applying one or several thresholding operations to reach the expected results. Generally, each thresholding process will generate two unique regions, meaning that, k threshold values will classify the image into $k + 1$ discrete levels, in which each level represents areas of pixels with similar intensity in the original image. Automatic calculation of

thresholding values is typically accomplished by one of many available algorithms such as the Otsu method [125], k-means clustering [126], and the entropy thresholding[127].

A modification to the above-mentioned thresholding methods are the local adaptive thresholding algorithms which continuously change the threshold based on the intensity values of the neighborhood around the pixel of interest [111, 128]. These options offer great advantages in the segmentation of images with undesired intensity variations. User inputs for these type of models usually are the sensitivity and the neighborhood size values. These parameters are based on the features size and the intensity variation on the images; however, user expertise will ultimately determine the segmentation results. `Adaptthresh` is the MATLAB function that computes a local adaptive threshold for 2D grayscale images (or 3D grayscales volumes).

Once the thresholding step (or steps) is completed, post-processing of the binarized image may be required to improve the results. In some cases, the segmented features need to go through morphological alterations such as dilation and erosion to expand or contract the regions [129]. Different sequences of these dilation and erosion transformations can be employed depending on the specific needs [130]. On the other hand, cleanup of some undesired features is necessary. These "extra" features can pertain to residual noise particles captured by the thresholding process, or to objects in contact with the boundary of the image that should not contribute to the statistical analysis, which in both cases, should be removed from the segmented image.

Validation process of the segmented images is constantly being implemented all along to check the results and to determine the necessary adjustments to the sequence. The lack of a ground truth for every image (which is simply impossible) makes the validation

process quite challenging. Validation can be categorized into two groups: qualitative and quantitative segmentation validation. The first one is typically performed by a domain expert who visually compares the original and the segmented images to detect evident segmentation errors. This type of validation serves always as first approach and techniques such as outline, overlay and labeling can assist in the process [101, 131, 132]. Although this methods has been successfully implemented in many previous studies [90, 102, 106], it can be recognized as a very time and cost inefficient method due to the very manual nature of it and the user subjectivity that it carries.

On the other hand, quantitative validation utilizes microstructural statistics such as volume fractions, precipitate and/or grain size distributions, as well as higher-order statistics for the verification of the segmentation results. Despite the fact that quantitative validation is always preferred, it is not always possible to obtain such statistics. Some non-image-based characterization methods are X-ray diffraction (XRD) [133, 134], analytical calculations [135], numerical simulations and thermodynamic equilibrium software [136]. There also exist image-based methods among which point count [137] and precession/recall scores are examples.

2.2.3 2-Point Statistics

A very important effort from the scientific community has been put into the quantification of microstructural features that exhibit a strong correlation with the material's properties of interest. The metrics defining these features are usually inputs in the design process and models of materials that target specific property values [99, 138-144]. Due to the limited knowledge that we have on the physics that governs deformation

processes and their interaction with salient features, relatively simple measures are preferred for the simplification of the mathematical representation of such interactions. Widely used microstructure metrics are volume fractions of phases, average size, aspect rations and crystallographic texture. However, significant microstructural information is lost in the process, and therefore a perfect reconstruction of the original microstructure is naturally not possible.

n-point spatial correlation have been proposed as alternative approaches for a more thorough microstructure quantification [99, 145-148]. They have been successfully implemented as microstructural measures in recent homogenization models of effective properties [149, 150]. The most basic form of n-point spatial correlations refers to the one-point spatial correlation. This is commonly known as the volume fraction f of the distinct microstructure constituent h (denoted here as a local state), and it's typically expressed as f^h. The discrete representation of a microstructure function is given by m_s^h, where h can take any integer value up to H number of local states of interest, and s denotes the discretized spatial bins (pixels for 2D microstructure images) and can be expressed as $s = \{s_x, s_y\}$ [6]. The next tier of spatial correlations is the 2-point statistics, which represents the probability of finding two pixels, each of them with local states h and h', separated by a vector r (defined by magnitude and orientation values). These relation is expressed by $f^{hh'}(r)$ and contain important amounts of information regarding the spatial distributions of the local states including their directionality. These statistics have played key roles in the construction of structure-property linkages [95, 151, 152], and process-structure linkages [38, 94, 152] for a wide range of material groups. The mathematical representation of the 2-point statistics is expressed as:

$$f_r^{hh'} = \frac{1}{|S_r|}\sum_s m_s^h m_{s+r}^h \quad 9)$$

In equation (9), $|S_r|$ is a normalization factor that contains the number of valid trials for each unique vector r where a trial is considered valid if both s and $s+r$ lie as completely withing the area (or volume for 3D microstructures) of the image being analyzed [6, 64, 153]. It has been determined that discrete Furrier transforms (DFTs) present as an efficient approach for the computation of the convolution on the right side of equation (9). A special case of these statistical representations occurs when $h = h'$, in which case they are called autocorrelations; all the other cases are known as cross-correlations. In the autocorrelation map, such as the ones presented in ***Figure 5(b, d)***, the center pixel corresponds to the vector of length 0. The value of this pixel depicts the volume fraction of the phase upon which the statistics are being calculated. These maps also contain other morphological information such as the average precipitate/grain size, and the average distance to their neighboring regions.

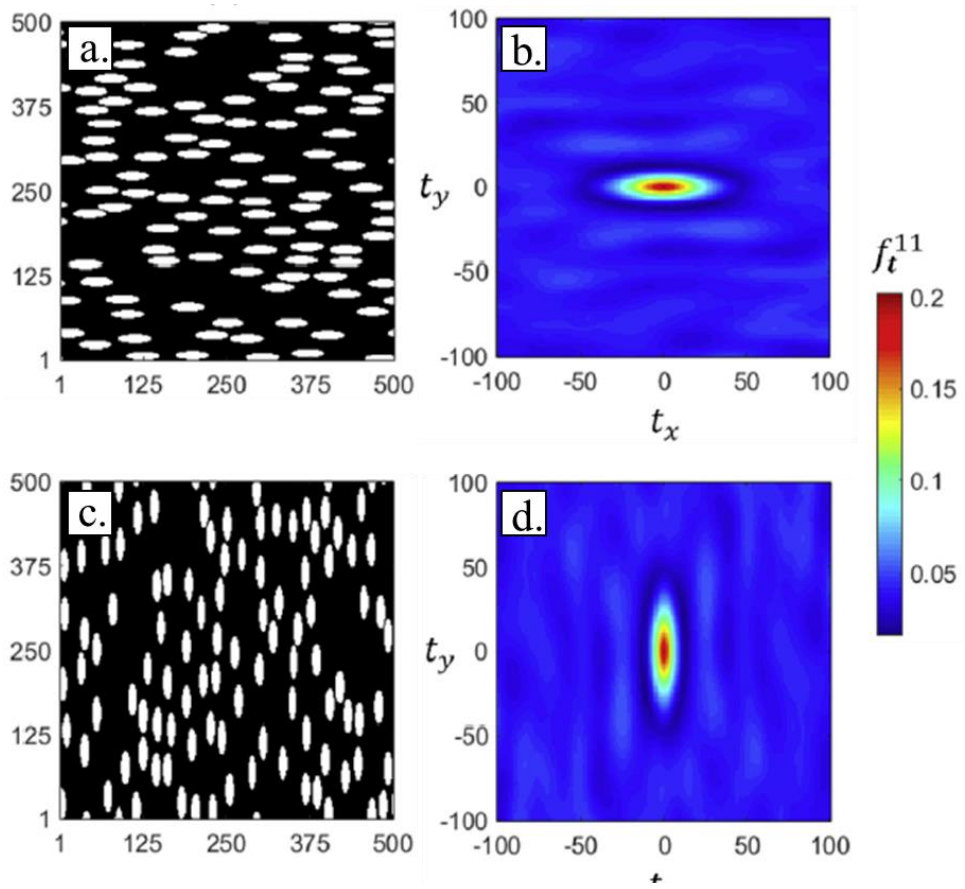

Figure 5*. Synthetic images of two different microstructures with their respective 2-point statistics plots of the white phase on the right. (a) and (b) microstructure of randomly distributed nonoverlapping horizontal ellipses. (c) and (d) 90° rotation of the microstructure immediately above [6].*

As mentioned before, the 2-point statistical representation of a microstructure, contains the directionality information of the constituents. This capability incurs in a inherit sensitivity to the observer's reference frame which is not always desired. For example, the microstructural images presented in ***Figure 5(a, c)*** may refer to the exact same laboratory specimen, with the only difference being the viewer's perspective. However, their 2-point statistical representations in ***Figure 5(b, d)*** show the 90° rotation between the ellipse axes,

which from a statistical point of view, refer to completely different microstructures. During the construction of a structure-property relationship, although the mechanical properties (e.g., from spherical indentation) from both cases would be exactly the same, the differences between the statistical representation would incur in significant erroneous results. There are many situations where the spatial correlations should capture the anisotropy from the constituents, but insensitivity to the observer's reference frame is needed. For example, titanium microstructures containing lamellar or basket-weave morphologies where different grains present distinct lath directionality (always keeping the same relative misorientation between laths), but due to the geometrical symmetry of the spherical indenter, the mechanical behavior will be independent to this directionality.

In an effort to address these needs, Cecen et al. [6] proposed the rotationally invariant 2-point spatial correlations protocols where the original Cartesian coordinate frame, $f_{t_x,t_y}^{hh'}$, is now transformed into polar coordinates, $f_{|t|,\theta}^{hh'}$, in order to facilitate periodic shifts of the statistics in the θ direction in order to adjust the reference frames of the microstructures. The next step in the process is the application of a DFT operation along the angular dimension of the 2-point statistics in polar form (Eqn. (10)).

$$\tilde{f}_{|t|,k_\theta}^{hh'} = \Im\left(f_{|t|,\theta}^{hh'}\right)_\theta \qquad 10)$$

However, this also translates the statistics into frequency space. Therefore, an inverse DFT in the k_θ direction is needed to convert back into original space [6]. The mathematical form of this operation is:

$$\tilde{f}^{hh'}_{|t|,\psi} = \Im^{-1}\left(\left|\tilde{f}^{hh'}_{|t|,k_\theta}\right|\right)_{k_\theta} \qquad 11)$$

This is now the final form of the rotationally invariant 2-point statistics where the dominant information of the microstructure is aligned with $\psi = 0$. A very important benefit of this representation, is that we are still capturing the relative angular differences between the salient morphological features of interest [6].

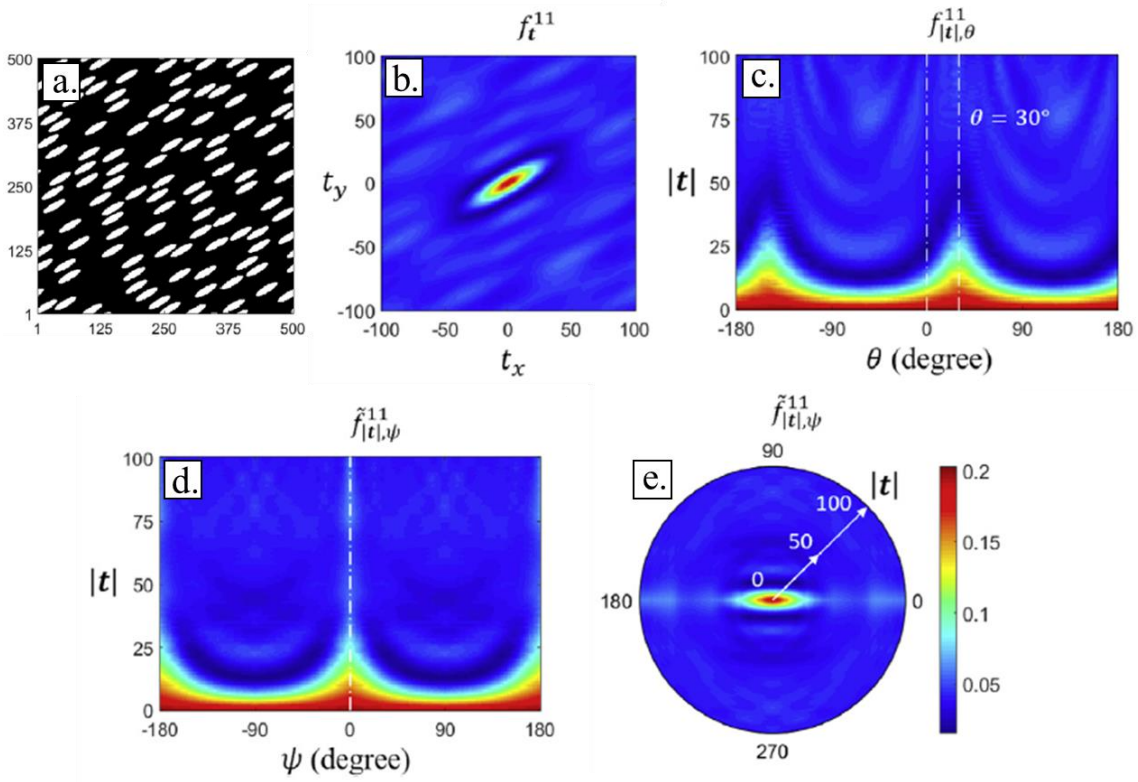

Figure 6. *Visual schematic of the transformation process from 2-point correlations into rotationally invariant 2-point correlations of a two-phase synthetic microstructure in (a). (b) Conventional 2-point statistics map in cartesian coordinates. (c) 2-point stat statistics in their respective polar coordinates. (d) Rotationally invariant 2-point statistics in polar coordinates. (e) Final form of the rotationally invariant statistics in polar visualization [6].*

Figure 6 presents a step-by-step schematic of the transformations involved in the process of removing the reference frame directionality from the 2-point correlations of a simulated two-phase microstructure. ***Figure 6(a)*** is the 2-dimentional image of a microstructure with randomly placed ellipses with their major axes oriented at 30° from the horizontal. ***Figure 6(b)*** corresponds to the 2-point autocorrelation of the white phase of the microstructure in cartesian coordinates. ***Figure 6(c)*** 2-point statistics in a polar representation from which we can see the peak being located at $\theta = 30°$ and $\theta = 150°$ corresponding to the preferred orientations of the ellipses. Both ***Figure 6(d)*** and ***Figure 6(e)*** present the rotationally invariant 2-point statistics in polar coordinates. The dominant information is observed to be aligned with $\psi = 0°$ and $\psi = 180°$, in accordance with the $30°$ shift in the directional direction [6].

2.3 Extraction of Intrinsic Properties

Most crystal elastic-plastic theories use intrinsic single-crystal properties as model parameters. This means that, grain-level experimental measurements that capture crystal anisotropy such as the ones from micro-hardness, compression on micro-pillars or nano-indentation, cannot be used directly for this purpose. Instead, a significant amount of work has been put into the extraction of intrinsic properties from the measured grain-scale experimental data and the crystal orientation. Pertinent to the present work, a two-step Bayesian framework has been successful at extracting intrinsic material properties from spherical indentation tests on polycrystalline cubic and hcp metal specimens [49, 51, 154, 155].

The first step in this framework requires a high fidelity reduced-order model (i.e., surrogate) that predicts the indentation property based on the crystal-level intrinsic properties and lattice orientation information. For the case of the hcp α-titanium grains, the elastic stiffness parameters, $\{C_{11}, C_{12}, C_{44}, C_{13}, C_{33}\}$, are used to predict the indentation modulus, and the slip resistances from the possible slip systems, $\{S_{pr}, S_{ba}, S_{pyr-a}, S_{pyr-ac}\}$, will determine the indentation yield strength. The second step in this process is the calibration of a physics based finite element (FE) model of the indentation test by using experimentally collected data [154]. It is worth mentioning that for the specific case of spherical indentation, it is preferred to use the normalized indentation stress-strain curves instead of the load-displacement data [49, 65, 66], due to the tedious process involved in determining the elastic segment from the raw information (see section 2.1 for a deeper explanation).

The reduced-order model capturing the dependence of the indentation properties on the intrinsic crystal-level material properties and crystallographic lattice orientation in the deformation zone, is constructed using Bayesian linear regression (BLR) making them very computational efficient [51, 156, 157], and is calibrated to high-fidelity physics-based finite element simulations. These simulations are based on crystal-plasticity theories [158-160] and conducted on the widely available ABAQUS finite element analysis software, and the theories assume crystallographic slip on the available slip systems [161] to be the sole crystal deformation mode. A discrete representation of this model can be given by Eq. (12), where P^*_{sim} denotes the simulated indentation property (e.g., indentation modulus or indentation yield strength), $\boldsymbol{p}$ represents the single-crystal intrinsic property and $\boldsymbol{g}$

corresponds to the crystallographic orientation (see section 3.3 for explanation on the Bunge-Euler orientation convention).

$$P_{sim}^{*} \approx \hat{P}^{*}(\boldsymbol{p},\boldsymbol{g}) = \sum_{l=0}^{L}\sum_{m=1}^{M(l)}\sum_{\boldsymbol{q}}^{\boldsymbol{Q}} A_l^{m\boldsymbol{q}}\, K_m^l(\Phi,\varphi_2)\tilde{P}^{\boldsymbol{q}}(\overline{\boldsymbol{p}}) \qquad 12)$$

Here, $K_m^l(\Phi,\varphi_2)$ specifies the orientation space of interest over which the surface spherical harmonics (SSH) basis is symmetrized, the values Q and L denote different truncation levels implemented in the equation, and the model coefficients given by A are obtained by application of a Bayesian linear regression on the FE experiment simulations database [7, 51]. The application of this BLR is of enormous importance since it allows for the calculation of the variance in the new predictions. As a result from these variances, it is possible to determine the parameters of the new predictions that would specifically maximize the potential for improving the model reliability [7] and therefore optimizing the computational resources utilized in the process.

The second step of the framework is the calibration of the reduced-order model built in the first step, by using the actual results from the grain-scale spherical indentation experiments on polycrystalline specimens. This step can be interpreted as an inverse estimation in which the intrinsic materials properties are estimated from the crystal-level mechanical behavior. This calibration is accomplished by using a Markov Chain Monte Carlo (MCMC) sampling strategy [7, 51, 162-164]. Minimization of the difference between the measured and the predicted indentation properties is a key in the model

optimization and can be interpreted as Eq. (13), where P^* refers to the measured indentation property.

$$P^* = P^*_{sim}(\boldsymbol{p}, \boldsymbol{g}) + \epsilon \quad (13)$$

2.4 Titanium alloys

2.4.1 Microstructure

The predominant constituent in titanium alloys is the α-phase, which presents a hexagonal closed packed (HCP) crystal structure. This phase is stable at temperatures lower than the beta-transus temperature, which is an alloy-dependent value. At 882.5 °C, pure titanium presents an allotropic transformation. From that hexagonal close-packed structure, the atoms rearrange into a body-centered cubic (BCC) crystal structure known as β-phase. The transformation temperature changes with the addition of alloying elements which can be categorized as either α- or β- stabilizers, resulting in the transformation temperature moving up or down as alloying elements for one category are added. The properties of titanium alloys are mainly governed by the morphology, volume fraction and individual properties of the two phases α and β [2]. With properly designed heat treatments (i.e., carefully selected temperatures, times and cooling rates), it is possible to obtain a variety of titanium alloy microstructures with diverse phase morphologies (e.g., equiaxed, colony bimodal, and basket-weave) [9, 165, 166]. Additionally, chemical composition will have a significant effect on the resulting microstructure. As shown in ***Figure 7***, the same heat treatment process for two different alloys, will produce very distinct microstructures.

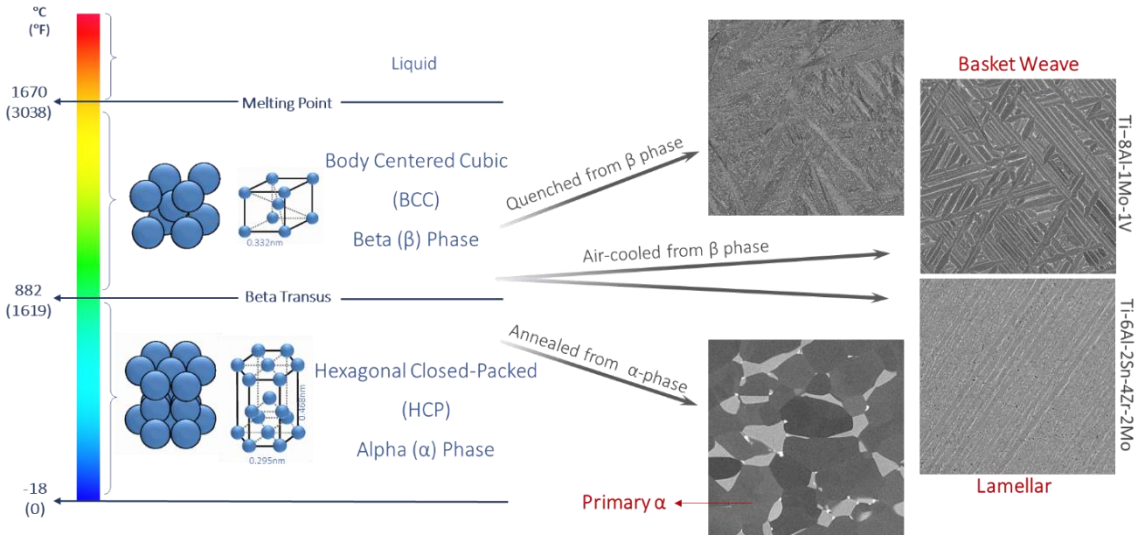

Figure 7. *Crystal structure of titanium alloys and the resulting microstructures for different heat treatments. (Temperatures values refer to pure titanium).*

Globular microstructure consists of roughly equiaxed primary-α grains, with irregular β phase, ***Figure 8(a),*** resulting from alloys worked and annealed in the α phase field [2]. This microstructure exhibits high levels of anisotropy, primarily due to the alpha phase being the dominant constituent. This behavior is strengthened as texture is sharpened with mechanical work.

The most important phase transformation in titanium alloys is perhaps the β→α transformation in microstructure evolution. Lamellar morphology for example, is formed from an originally annealed beta grain. At relatively low cooling rates and aging treatment, continuous and parallel layers of the same α orientation will develop inside the prior β grain as observed in ***Figure 8(b).*** The Burger's Orientation Relationship (BOR) states that there exist a relationship between the orientation of the original beta grain and the newly formed alpha lamellae. Parallelism between the respective closest packed slip planes $((101)_{\beta} \parallel$

$(0001)_\alpha$) permits the dislocation gliding on any of the three basal slip systems to pass through the α/β interphases. Fully lamellar microstructures are of great interest due to their close-to-ideal balance of properties.

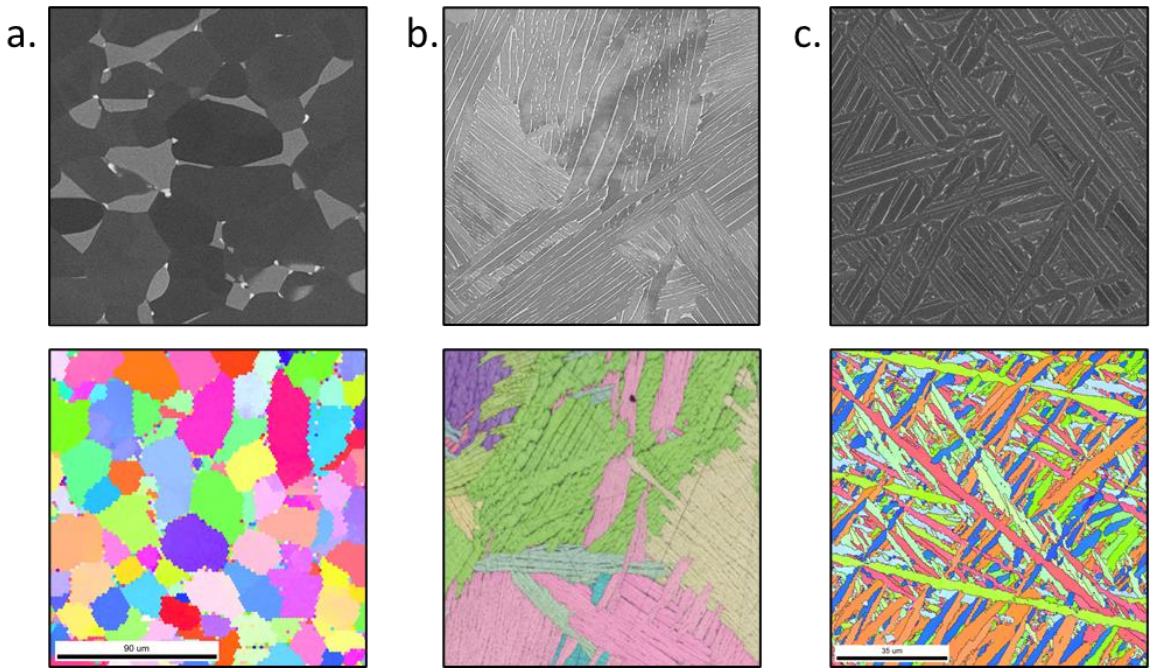

Figure 8. *SEM and EBSD images for the three most important morphologies present in titanium microstructures. a) Globular, b) lamellar and c) basket-weave.*

The most important phase transformation in titanium alloys is perhaps the β→α transformation in microstructure evolution. Lamellar morphology for example, is formed from an originally annealed beta grain. At relatively low cooling rates and aging treatment, continuous and parallel layers of the same α orientation will develop inside the prior β grain as observed in ***Figure 8(b).*** The Burger's Orientation Relationship (BOR) states that there exist a relationship between the orientation of the original beta grain and the newly formed

alpha lamellae. Parallelism between the respective closest packed slip planes ($(101)_\beta \parallel (0001)_\alpha$) permits the dislocation gliding on any of the three basal slip systems to pass through the α/β interphases. Fully lamellar microstructures are of great interest due to their close-to-ideal balance of properties.

On the other hand, if the cooling rate is increased, the formation of laths with larger aspect ratio, defined as the lath length over the thickness, are promoted, ***Figure 8(c)***. The higher cooling rate results in the increase of the transformation driving force, leading to the nucleation and growth of α-colonies from within the prior-β grain, and also from the boundaries of the newly formed α colonies. The resulting morphology is known as basket-weave [2] and is characterized for its α-laths arranged in crisscross patterns, and for presenting more than one α-orientation variant in same region of the prior-β grain. This represents a significant increase in the complexity of the microstructure. This newly formed α-phase presents the same hcp lattice structure and similar lattice parameters as the primary-α; therefore, the lattice distortion is generally considered as negligible.

The presence of lamellae/laths results in high density of semi-coherent lamellae boundaries affecting the dislocation motion which results in the enhancement of mechanical properties such as strength and fracture toughness. Prior-β grain size, volume fraction of the present phases and lath thickness, apart from the chemistry itself, are the main parameters to control the mechanical behavior at various length scales. All of these parameters can be controlled by an optimized heat treatment to improve and achieve the desired microstructure.

As a consequence, a unique set of macro-scale properties will be associated with each particular microstructure. Examples of these relationships are provided by Sieniawski et

al. [167] and G. Lutjering [82], where the yield strength and fatigue properties vary as the cooling rates of Ti-6Al-4V, Ti-6Al-2Mo-2Cr and Ti-5.8Al-4Sn-3.5Zr-0.7Nb-0.5Mo-0.35Si-0.06C are changed.

Titanium alloys can be heat treated for a variety of reasons. The relatively low temperature range of 480 to 650°C (for Ti-6Al-4V) is usually used for stress relieving processes. Sub-transus annealing (below β-transus temperature) is generally used for enhancement of creep resistance, strength-ductility combinations and phase stability at high temperature applications. Au contraire, β-annealing (isothermal hold into the β-phase field) leads to improved fracture toughness and a decrease in the notch sensitivity. If the objective is to achieve excellent fatigue strength and high tensile yield strength with reasonable ductility properties, ageing processing in a common option in the toolbox. Mill annealing refers to an isothermal hold in the temperature range 700-800°C for Ti-6Al-4V (or 704-843°C for Ti-6Al-2Sn-4Zr-2Mo) and it is considered an incomplete annealing treatment used to retain the wrought-state microstructure. Other treatments such as recrystallization, duplex, stabilization, and stress-relief annealing are also employed depending on the alloy and desired properties.

2.4.2 Chemistry

Titanium is a transition metal that forms solid solutions with most substitutional elements that fall in the ±20% atomic size ratio. Typical substitutional elements of titanium alloys include Al, Sn, Ga, Ag, V, Zr, Hf, Nb and Ta. Solubility of interstitials elements into a titanium matrix can be significant. Oxygen for example, can dissolve up to 14.25% at

600°C, and Nitrogen up to 7.6% at 1083°C, which is not necessarily common with other metals [2].

Titanium alloys broadly divided into two groups, commercially pure (CP) titanium and titanium-based alloys [2, 9]. CP titanium refers to materials with ≥99% titanium content, and are categorized as grades 1, 2, 3 or 4 based on their oxygen, nitrogen, carbon, iron and hydrogen contents. In the case of titanium-based alloys, alloying elements with electron/atom ratios of <4 stabilize the α-phase, elements with a ratio of 4 are considered neutral, sand those for which the ratio larger than 4 are β-phase stabilizers. Depending on the alloy element combination present in a particular alloy, the material is fit into a α, near-α, α-β, near-β, metastable-β, or β-titanium alloy category [2, 168].

Phase diagrams depicting the phase transformations for different titanium-based alloys are complex and many of them are yet to be completed. The phase diagrams of the Ti-Al and Ti-Mo systems are observed in ***Figure 9(a-b)*** for reference. Elements such as aluminum and oxygen, nitrogen, carbon and gallium, tent to favor solution into the α-phase and therefore rise the α/β-transus. Tin and silicon are usually regarded as neutral as they don't exhibit a notorious preference towards any of the phases. On the other hand, molybdenum, vanadium, chromium, iron, copper, manganese and hydrogen, stabilize the β-phase and depress the α/β-transus.

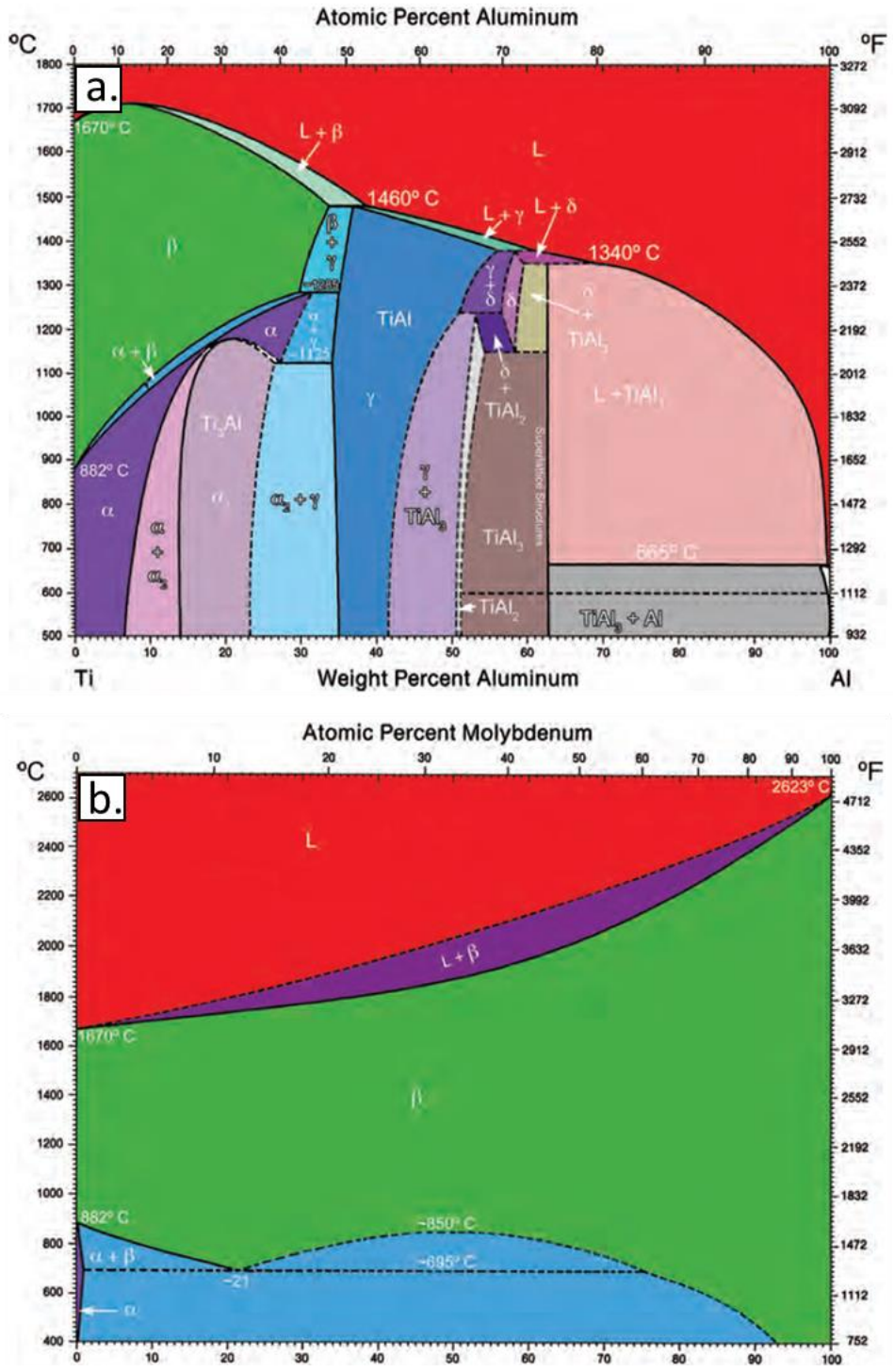

Figure 9. *Phase diagrams of the a.) titanium-aluminum and b.) titanium-molybdenum alloy systems [1].*

CHAPTER 3 High-Throughput Grain-Scale Mechanical Characterization of Primary-α Phase

3.1 Introduction

The key to understand the impressive properties of titanium alloys lies on the knowledge about their complex microstructures and the properties associated with each of the constituents. Crystal plasticity theories [169-171] allow one to systematically capture and explore the precise roles of the different slip system activities on the effective (macroscale) response of Ti alloy samples at large plastic strains. However, such studies have been largely hindered by the lack of reliable information on the grain-scale mechanical properties (e.g., single crystal elastic stiffness parameters, critical resolved shear strengths (CRSS) of different families of slip systems) of the individual phase constituents. This is evident from the fact that the reported polycrystal simulation studies in current literature [169, 172-177] use widely varying room temperature CRSS values for the different slip families in α-Ti. For example, the ratio of CRSS values for basal slip to prismatic <a> slip in α-Ti of Ti64 have been assigned values ranging between 1 and 5 in current literature [175-177]. Similarly, the ratios of CRSS values for pyramidal <a> and pyramidal <c+a> slip systems to prismatic <a> slip have been assigned values in the range of 1-5 and 1.25-15, respectively [175-177]. Clearly, grain-scale measurements of mechanical responses are critically needed to support the further refinement of the crystal plasticity theories being developed to predict the overall mechanical properties of Ti alloy samples.

Since α-phase forms in lenticular shaped grains in most Ti alloys, metalworking is typically used to obtain a more globular configuration (this form of the α-phase is generally referred as primary α). This offers opportunities for easier evaluation of its grain-scale mechanical properties compared to the α-phase. However, the hcp structure of the α-phase exhibits high levels of anisotropy in its mechanical properties at the single crystal scale, especially those related to its plastic response. Consequently, in order to evaluate critically the role of phase chemical composition on the mechanical response, one needs to characterize the grain-scale mechanical response of α-phase that accounts rigorously for the effects of the hcp crystal lattice orientation. Logically, this requirement can be pursued using two different approaches: (i) growing and testing large single crystals using standardized (macroscale) test methods, or (ii) developing and employing suitable small-scale testing methods that allow us to probe the grain-scale mechanical response in the individual grains of a polycrystalline sample. While it is possible to grow large single crystals of α-phase Ti [178-181], it places stringent limits on the chemical compositions that can be evaluated; this approach also incurs significant time and cost.

A variety of small-scale testing approaches have been explored for the evaluation of mechanical response of the α-phase component in Ti alloys. These have included compression tests on micropillars [17-21] and bending tests on micro-cantilever beams [182, 183]. Although these techniques have allowed the identification of the activated slip systems and the estimation of single crystal properties (e.g., critical resolved shear strengths (CRSS)), they have also raised questions on the potential effects from the use of the Focused-Ion Beam (FIB) for the fabrication of the specimen on the measured values of the properties [22]. Furthermore, there appears to be high levels of variance in the reported

values in the literature, sometimes even within a single study. For example, Gong et al. [182] reported CRSS values for prismatic $\langle a \rangle$ slip in the range of 140 MPa to 590 MPa from tests conducted on micro-cantilever beams of single crystal α-Ti, while Sun et al. [19] reported values between 150 MPa and 450 MPa for the same parameters estimated from compression tests on single crystal micropillars.

Nano-indentation using Berkowich and Vickers indenters offers an alternative approach for characterizing the grain-scale response of Ti alloys. For example, Mante et al. [184] have reported hardness measurements of 1.6 GPa and 1.9 GPa in Berkowich indentations conducted parallel and perpendicular to the c-axis, respectively, in a CP-Titanium sample. A more recent study by Merson et al. [185], however, reported hardness measurements of 2.73 GPa and 1.34 GPa, respectively, for very similar sample and test conditions. These studies clearly point to the lack of consistency in the indentation protocols and/or the subsequent analyses of the raw data obtained from the measurements. The main deficiency with the hardness measurements is that they do not represent an intrinsic material property (e.g., the measured values depend on the imposed load/displacement levels [31-33, 186]). In general, they correspond to the material flow stress after some non-standard amount of plastic deformation has been applied to the material.

The work from this task builds on the recent advances in spherical indentation stress-strain protocols and demonstrates their viability on a collection of five different Ti alloys with varying α-phase chemical compositions, where a large number of grains were studied for each alloy composition. The dataset assembled in this study represents the largest such dataset available today, comprising a total of 311 datapoints, where each datapoint

represents an indentation stress-strain curve corresponding to a distinct combination of grain orientation and chemical composition of α-phase Ti. Previously reported measurements on CP-Ti and Ti64 from Weaver et al. [5] were added to the dataset to enhance the comparisons presented in this work between the different Ti alloys. Where needed, especially in the case of Ti64, additional indentations were performed. The study strongly attests the claim that the spherical indentation stress-strain protocols represent the best of currently available high throughput protocols for grain-scale evaluation of mechanical responses in polycrystalline metal samples. This dataset is expected to provide new insights into the role of chemical composition and crystal orientation on grain-scale response of α-Ti.

3.2 Methods and Materials

3.2.1 Materials and Sample Preparation

Materials for this study were selected to represent a range of near-alpha and alpha-beta Ti alloys. Specifically, Ti8Al-1Mo-1V, Extra Low Interstitials (ELI) Ti5Al-2.5Sn, Ti6Al-4V, Ti6Al-2Sn-4Zr-6Mo and Ti6Al-2Sn-4Zn-2Mo were selected because of their importance to the automotive, aerospace and gas turbine industries. Specimens of these materials of sizes ranging from $5.0\ \text{mm} \times 8.0\ \text{mm} \times 5.0\ \text{mm}$ to $10.0\ \text{mm} \times 20.0\ \text{mm} \times 15.0\ \text{mm}$ were cut from larger bulk samples, and were individually heat treated to produce large primary-α grains. Large grains are desired to ensure that the indentation measurements within individual grains are not affected by the neighboring grains. Details of the heat treatments conducted for the different alloys are provided in ***Table 1***. In order to minimize the oxidation layers formed in the heat treatments, all specimens were

encapsulated in quartz tubes with vacuum up to about 10^{-6} torr. All heat treatments were performed in a Thermo Fisher Scientific, Lindberg/Blue 1100 °C Box Furnace.

Table 1. *Summary of the heat treatments applied on the different alloys to produce the specimens used in this study.*

	Heat Treatment	
Alloy	**Primary Treatment**	**Secondary Treatment**
Ti811	1028 °C - 2 hours - Air Cooled	800 °C - 24 hours - Air Cooled
Ti5-2.5	800 °C - 2 hours - Air Cooled	-
Ti6242	970 °C - 12.5 hours - Furnace Cooled	-
Ti6246	915 °C - 24 hours - Furnace Cooled	-
Ti64	825 °C - 4 hours - Water Quenched	700 °C - 4 hours - Air Cooled
CP-Ti	800 °C - 2 hours - Furnace Cooled	-

Sample preparation plays an important role in the quality and accuracy of the indentation measurements, especially for the spherical indentation stress-strain protocols [187]. The samples were prepared using standard metallography procedures to obtain relatively flat and undisturbed material surfaces in order to ensure that the indentation measurements reflect the true response of material (i.e., removing any oxide layer or other disturbed layers produced due to how the samples are cut from the larger bulk specimen and handled during the various heat treatments). The chemo-mechanical preparation of samples consisted of two stages: first, grinding using silicon carbide papers down to 4000 grade, followed by polishing with 3 μm and 1 μm diamond suspension, and second, vibro-polishing with 1 part of 0.06 μm colloidal silica, 4 parts of water and 1 part of hydrogen peroxide for 12 hours.

3.2.2 Microstructure and Mechanical Characterization

Microstructures in the sample were characterized using back-scattered electron (BSE) and electron back-scattered diffraction (EBSD) imaging using a Tescan Mira3 field emission scanning electron microscope (FE-SEM). These maps were used to identify the grains and locations where the indentation measurements were carried out. High voltage of 10 kV and 20 kV was used on all specimens for the BSE and EBSD scans, respectively.

Mechanical characterization by spherical indentation stress-strain protocols [34, 36] was conducted at room temperature on a Nano-indenter G200 by Keysight (formerly Agilent). This equipment is capable of obtaining a continuous stiffness measurement (CSM) in addition to the measurements of the raw load and displacement signals in the indentation tests. This capability allows for a much more reliable extraction of the indentation stress-strain curves (detailed further in section 2.3). An indenter with a diamond spherical tip of radius 15.2 μm was selected for this study. This tip size was selected to ensure that the ratio of grain size to contact diameter $(2a)$ at yield would be higher than or equal to 10. This criterion is designed to ensure that the measurements in individual grains are not influenced by any of its neighbors. However, since we are not documenting the microstructure under the indentation surface, one should note that some effects from the neighboring grains are unavoidable in the experiments reported here. Of course, larger the ratio of the grain size to the contact diameter, the lesser the likelihood of the influence of the neighboring grains in the characterized responses. The average grain sizes in the samples tested were in the range of 15 μm - 30 μm. In our experiments the contact diameter estimated using Hertz's theory (details provided later) was estimated to be less than 1.5 μm for the 15.2 μm tip radius, when significant plastic deformation has

been initiated under the indenter. Therefore, the indentations reported in this study can be treated as contained within individual grains. A typical residual impression in the grain is shown in ***Figure 10***, in which the calculated contact area at yield is indicated by a red circle. Because of the very low indentation depths at indentation yield, pile-up/sink-in effects are minimal. Furthermore, Taljat and Pharr [188] showed that for an elastic/plastic material with $\frac{E}{\sigma_y} \approx 100$ subjected to spherical indentation, very small amounts of pile-up/sink-in were predicted for the very low indentation depths. Although indenter tips of smaller radius are available, they were not selected because they exhibit a higher tendency to produce pop-ins [5, 44, 77, 187, 189]. The maximum indentation depth was kept constant for all tests at 500 nm. All indentation tests were performed at a nominal strain rate of about 0.05 s^{-1}.

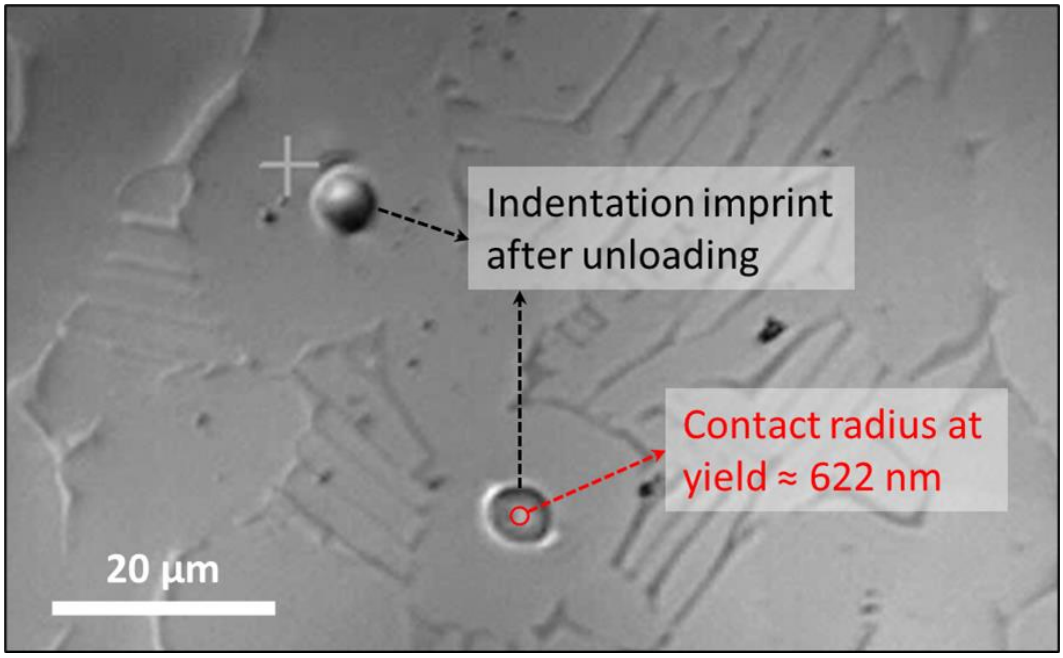

Figure 10. *Optical micrograph of indentation imprints in the Ti6262 polycrystalline sample from this study, showing the size of the contact area at yield (highlighted by the red circle) and at maximum load (indicated by black arrows) relative to the grain size.*

3.2.3 Chemical Composition Analysis

Chemical composition analysis of all substitutional alloying elements in the α-phase was performed in all the samples using electron microprobe analysis (EPMA) on a Cameca SX-100 electron probe microanalyzer. Standards used for analysis are from SPI Supplies, West Chester, PA, catalog number 02752-AB. All samples were coated with 20 nm carbon prior to analysis using pulsed cord evaporation protocol on a Quorum Q150 ES. Calibration on pure metal standards was performed prior to testing on samples, using accelerating voltage of 20 kV and current of 20 nA. Chemistry analysis of oxygen (average composition as opposed to only alpha phase) was performed by the inert gas diffusion technique in accordance with the ASTM E1409-13 standard [190].

3.3 Results and Discussion

Results from the chemical composition analysis performed on the α-phase components of all the alloys studied in this work are summarized in ***Table 2***. Aluminum is the primary solute in the α-phase, and its content varied from 9.23 to 13.8 at.% (5.35 to 8.28 wt.%) across the different alloys studied. Because this composition range is not expected to promote the formation of the intermetallic compound Ti_3Al (referred to as α_2) [191] under the heat treatment conditions conducted in this study (e.g., no low temperature age for a long duration), Transmission Electron Microscopy (TEM) was not employed to confirm the absence of this compound. The tin content ranged from 0 to 0.95 at.% (0 to 2.43 wt.%), while the zirconium content ranged from 0 to 1.91 at.% (0 to 3.72 wt.%). Both tin and zirconium are neutral stabilizers, and their distribution is expected to be roughly the same in both phases in the alloys that have them. The vanadium content ranged from 0.00 to 1.45

at.% (0 to 1.62 wt.%), while molybdenum content varied from 0 to 0.31 at.% (0 to 0.64 wt.%). Both vanadium and molybdenum are known isomorphous β-stabilizers, and hence partition preferentially to the beta phase, explaining their low content in the α-phases studied in this work. Regarding interstitial elements, carbon, oxygen and nitrogen tend to partition to the primary alpha phase, whereas hydrogen prefers the beta phase. However, the presence of carbon and nitrogen is expected to be negligible in these alloys. Due to the difficulties associated with EPMA-WDS in measuring the amount of trace and light elements [192], the inert gas fusion standard was employed, which indicated oxygen content varying from 0.15 to 0.51 at.% (0.05 to 0.20 wt.%).

Table 2*. Chemical compositions of the primary-α phases in the titanium alloys studied in this work. Amount of oxygen was determined in accordance with ASTM E1409-13 by Inert Gas Fusion. All other elemental compositions were measured using Electron Probe Micro analysis (EPMA) technique.*

	Chemical Composition (at. %) of Ti α-Phase						
Alloy	**Ti**	**Al**	**Mo**	**V**	**Sn**	**Zr**	**O***
Ti6246	83.83	12.70	0.31	0.05	0.80	1.91	0.40
Ti6242	85.07	11.74	0.14	0.00	0.75	1.80	0.51
Ti811	85.39	13.75	0.08	0.41	0.00	0.00	0.38
Ti64	86.16	11.83	0.00	1.44	0.00	0.00	0.57
Ti5-2.5	89.68	9.22	0.00	0.00	0.95	0.00	0.15
CP Ti	99.54	0.00	0.00	0.00	0.00	0.00	0.46

The lattice orientation of a HCP crystal with respect to the sample (indentation) frame can be defined by the set of Bunge-Euler angles $\{\varphi_1, \Phi, \varphi_2\}$ [193], as described in ***Figure 11(a-d)***. Of these angles, φ_1 denotes a rotation about the indentation axis (selected as the sample e_3-axis). Because of the axial symmetry of the spherical indenter, the measured indentation load-displacement responses (and all extracted properties from these responses) are expected to be independent of φ_1. This is because a simple in-plane rotation of the sample is not expected to change the measured indentation load-displacement response even when the sample exhibits significant anisotropy in its mechanical response (as expected in the present case). Furthermore, because of the transverse symmetry of the elastic response of the hcp crystal with respect to its c-axis, the measured elastic indentation responses on hcp crystals are also expected to be independent of φ_2. As a consequence, the indentation moduli measured in this work are expected to show only a dependence on Φ, while the measured indentation yield strengths are expected to show a dependence on both Φ and φ_2. Physically, Φ corresponds to the angle between the indentation direction and the crystal c-axis and is also referred as the declination angle. The high sensitivity of the indentation properties to the declination angle in hcp crystals has already been reported in prior work [5, 63, 154, 155, 194, 195].

Examples of measured indentation load-displacement curves from three different grains in the Ti6242 sample with declination angles close to $\Phi = 0°$, $45°$ and $90°$, respectively, are presented in ***Figure 12(a).*** Even though only small differences exist in the initial elastic portions of the measured load-displacement curves, these differences are magnified and become much more clear in the corresponding ISS curves presented in ***Figure 12(b)***. As expected, the declination angle is seen to have a significant influence on

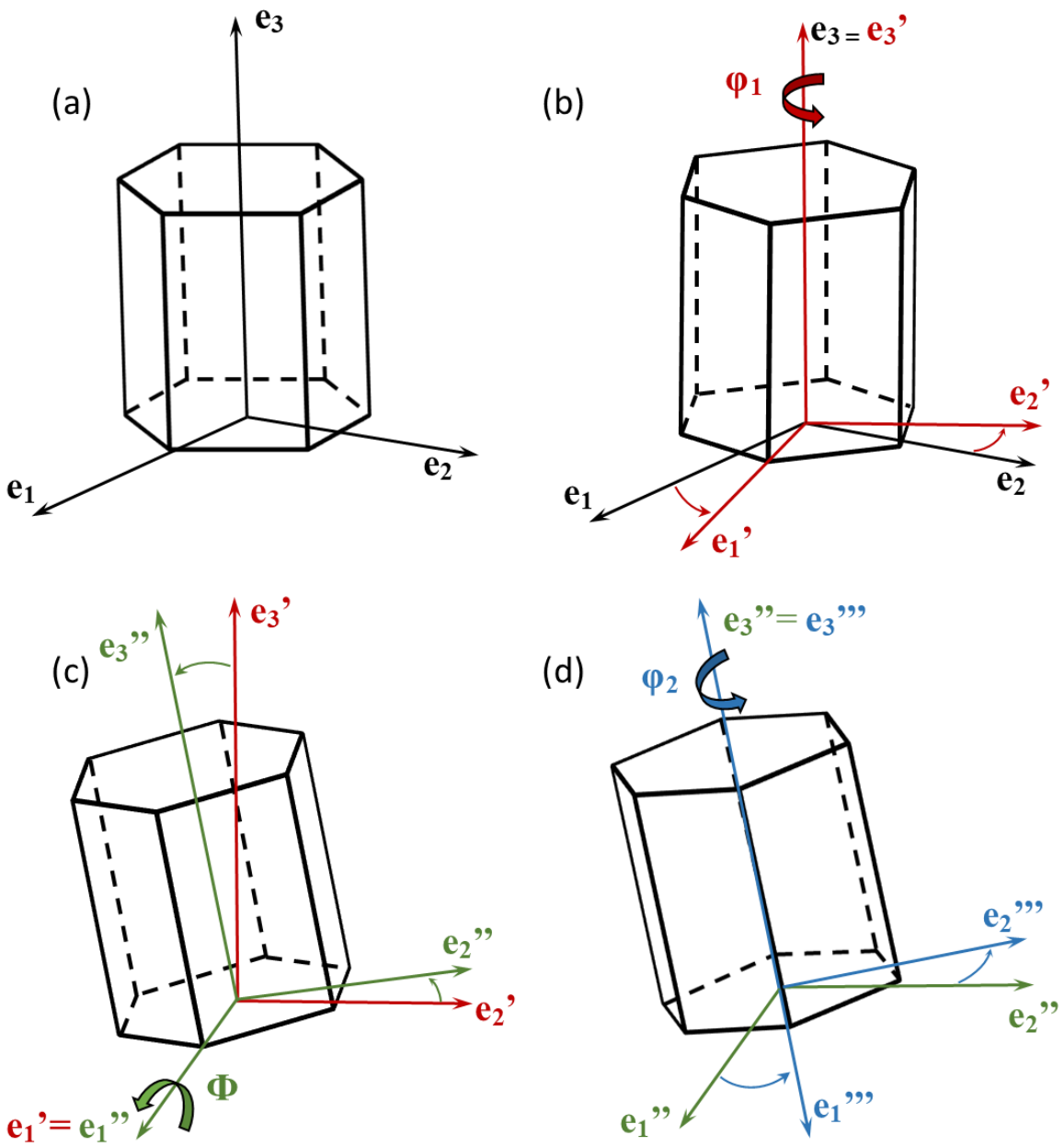

Figure 11. *Depiction of the Bunger-Euler angles used to describe the hcp crystal orientation with respect to the sample reference frame. This relationship is described through a sequence of three rotations, where the hcp crystal is initially oriented parallel to the sample reference frame (denoted by* $\{e_1, e_2, e_3\}$*) and brought into coincidence with the crystal reference frame. (a) Initial alignment of the hcp crystal with the sample reference frame. (b)-(d) The sequence of three rotations* $\{\varphi_1, \Phi, \varphi_2\}$ *to bring the crystal in alignment with the crystal reference frame.*

both E_{ind} and Y_{ind}, although the effect is significantly larger on the latter. It is clearly seen that the c-axis is the stiffer and harder direction in the spherical indentation of hcp crystals. These observations are in agreement with prior reports on the anisotropy of hexagonal crystals [5, 185, 196], and can be attributed largely to the required activation of pyramidal $\langle c + a \rangle$ slip systems in the indentations parallel to the c-axis.

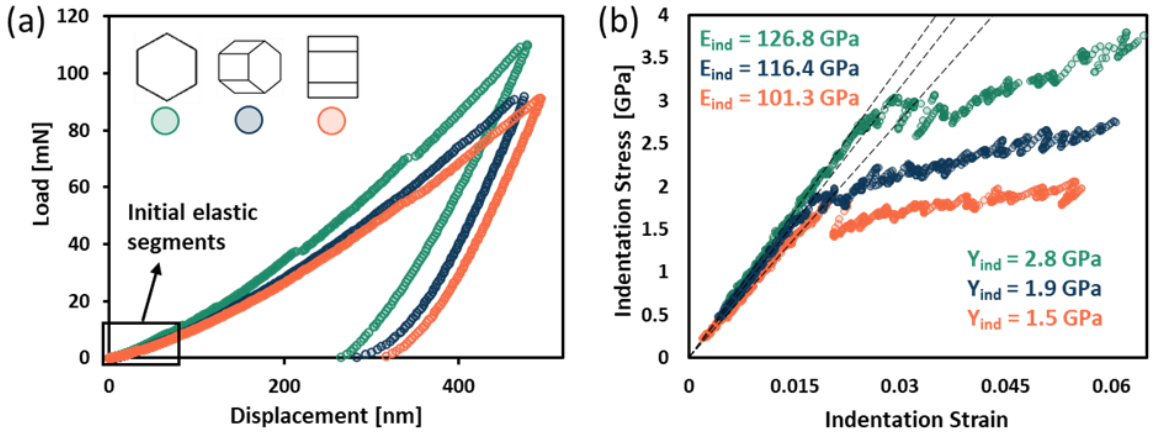

Figure 12. *a) Load-displacement curves from selected primary-a grains in Ti6242 with lattice orientations expressed in Bunge-Euler angles as [0.1˚, 1.7˚, 266.5˚], [282.8˚, 48.7˚, 305.7˚] and [261.2˚, 85.4˚, 176.2˚]. b) Corresponding ISS curves reflecting the effect of the c-axis orientation on the indentation response.*

Figure 13(a, b) summarize all of the measured primary-α indentation moduli as a function of the declination angle (recall that this is the only orientation related variable influencing the indentation modulus) for all alloy compositions studied in this work. It is clearly seen, especially in the trendline plots shown in ***Figure 13(b)*** that the indentation modulus decreases with an increase in declination angle, suggesting that the c-axis

continues to be the stiffest direction for all of the alloys studied. On an average the indentation modulus along the c-axis is about 24% higher than the indentation modulus perpendicular to the c-axis for these alloys. It is also noted that the addition of different alloying elements (the main one being Al) decreases the elastic stiffness of the different primary-α phases studied in this work. It is difficult to isolate the effects of the individual alloying elements on the indentation moduli from these results, because of the relatively small changes in the moduli with changes in both the declination angle as well as the changes in the alloy compositions.

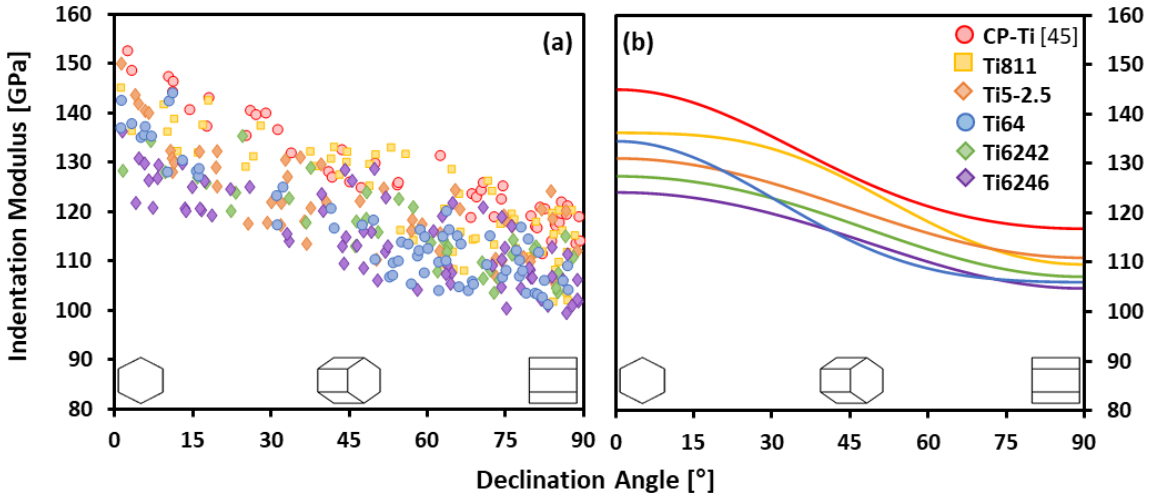

Figure 13*. Indentation modulus as a function of the declination angle for all titanium alloys studied in this work. (a) Measured values. (b) Regression analysis on experimental data. Results from Weaver et al. [5] for CT-Ti have been added to facilitate comparison with the results from this study.*

It is clear from ***Figure 13*** that there is significant noise in the measured indentation moduli (similar observations can be made subsequently for the measurements of indentation yield strengths). This noise arises from various uncontrolled factors in the measurements and analyses protocols described earlier. These may include the presence of

grain boundaries close to the indenter below the sample surface, improperly prepared sample surfaces, deviations in indenter shape from the ideal spherical shape, frictional contact between the sample and the indenter, and errors in the analysis protocols described earlier (e.g., incorrect identification of the initial elastic regime on the measured load-displacement curve). The central advantage of the high-throughput protocols employed in this work is that we can generate a significantly large dataset (e.g., see ***Figure 13***) and estimate reliable values of material intrinsic parameters (as shown in Part II of this series) using advanced statistical techniques that extract and utilize the underlying trends, while accounting for the noise.

Williams et al. [197] demonstrated that the presence of oxygen and aluminum in titanium alloys (specially above 5 wt.% Al) effectively suppressed twinning as the primary deformation mechanism in compression tests performed parallel to the c-axis. Weaver et al. [5] did not find evidence of deformation twinning in their spherical indentations on CP-Ti grains with indenter tips of radii 16 μm and 100 μm. Observations from the present work are in agreement with the previous analysis as no evidence of deformation twinning was observed in or near the residual indents. Since similar grain-scale indentations on polycrystalline zirconium and magnesium showed twin markings in and around the residual indentation [63, 198], it is clear that slip was the dominant deformation mechanism in all of the tests reported here.

The variation of the measured indentation yield strengths with Φ and φ_2 are presented in ***Figure 14*** as contour maps on an Inverse Pole Figure (IPF). The actual measurements are also shown in these plots as colored circles. The contours shown were obtained by regressing the data to a Fourier representation using generalized spherical harmonics as a

basis, and then using the Fourier representation as an interpolator over the IPF domain [5]. It is clear from these plots that the measurements exhibit low sensitivity to φ_2, but a strong dependence on Φ. As expected, c-axis represents the hardest indentation direction for all the alloys studied. As already mentioned, this is because compression along c-axis requires activation of the hard pyramidal $\langle c+a \rangle$ slip. As the declination angle is increased, the easy prismatic $\langle a \rangle$ slip systems [5, 41, 183, 195, 197, 199] become more active, resulting in lower indentation yield strengths. It is also noted that the influence of φ_2 on the indentation yield strength is highest for CP-Ti. This points to a higher contrast in the slip resistances of prism and basal systems in this alloy compared to the others and confirmed by the estimations by Castillo et al. [7].

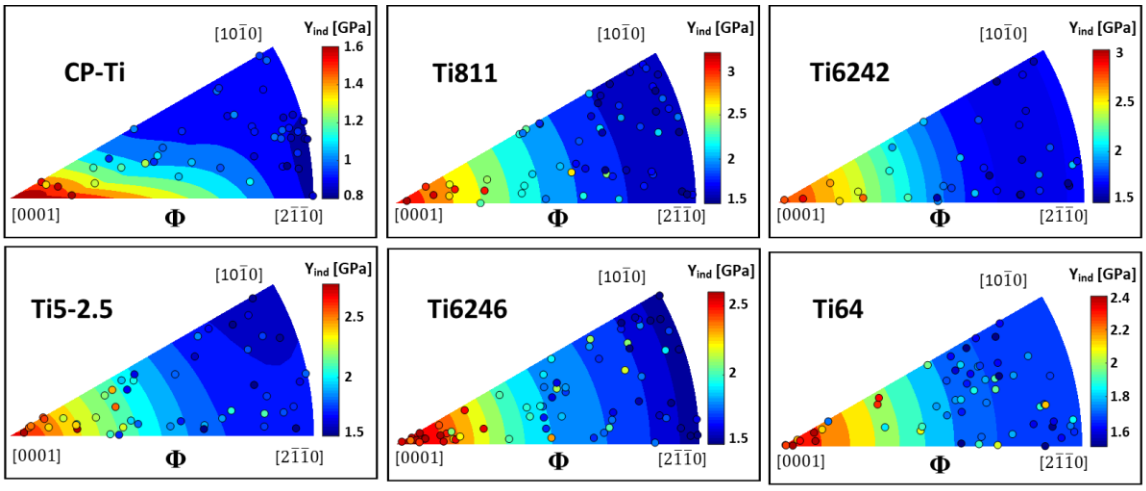

Figure 14. *IPF Contour plots depicting the dependencies of measured indentation yield strengths on the Bunge-Euler angles Φ and φ2. These plots were produced using fits to Fourier representations based on generalized spherical harmonics.*

In order to compare the indentation strengths of the different α-phases, it is much more convenient to plot the measurements as a function of the declination angle Φ (as already noted the dependence of the measurements on φ_2 is quite weak). The measured indentation yield strengths for all the alloys are presented in ***Figure 15(a)*** along with the trend lines obtained from the regression analyses mentioned earlier. From ***Figure 15(a),*** it is clear that the indentation yield strengths perpendicular to the c-axis exhibit much lower sensitivity to the alloy compositions compared to the indentation yield strengths measured parallel to the c-axis. Specifically, it is instructive to look at the increases in the indentation strength compared to CP-Ti, which provides a good baseline for understanding the effects of the different alloy compositions. Implicitly, in such analyses, the overall slip resistance is assumed to be the sum of the contributions from the different solid solutions present in the alloy. The indentation yield strength parallel to the c-axis was observed to increase between 0.8 GPa (for Ti64) and 1.6 GPa (for Ti811), with respect to CP-Ti, while the corresponding increase in the indentation yield strengths perpendicular to the c-axis was ~0.7 GPa for all of the alloys. It should be noted that indentations parallel to the c-axis are expected to be dominated by pyramidal $\langle c+a \rangle$ slip, while those at large declination angles will be dominated by combinations of prismatic $\langle a \rangle$ and basal slip systems. These expectations are indeed confirmed in the CPFEM simulations [7]. Utilizing these insights, the observations made earlier form ***Figure 15(a)*** clearly suggest that all of the different alloying elements in the alloys studied in this work produced a bigger increase in the resistance to the pyramidal $\langle c+a \rangle$ slip compared to the increase in the resistances to the prismatic $\langle a \rangle$ and basal slip systems. Therefore, we can conclude that the resistance to the pyramidal $\langle c+a \rangle$ slip system exhibits a higher sensitivity to the variations in alloy

chemistry compared to the resistances to the prismatic $\langle a \rangle$ and basal slip systems in the alloys studied.

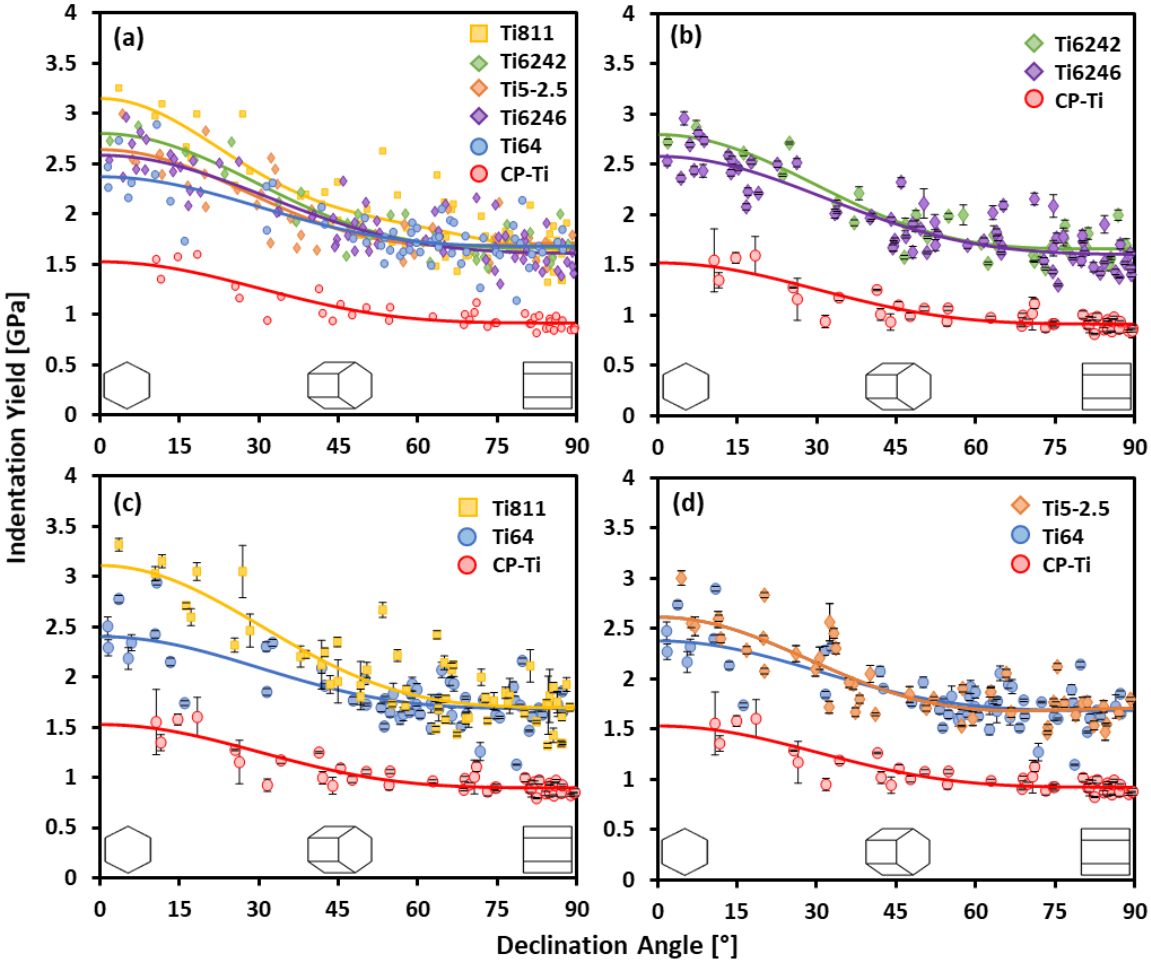

Figure 15. *Variation of the indentation yield strength with the declination angle. The solid lines represent regression fits. The comparisons are presented in different groupings. (a) All Ti alloys studied in this work. (b) Comparison of Ti6242 and Ti6246 to elucidate the effect of Mo. (c) Comparison of Ti811, Ti64, and CP-Ti to elucidate the effect of Al. (d) Comparison of Ti5-2.5, Ti64, and CP-Ti to elucidate the effect of Sn. The CP-Ti results are taken from [5].*

Additionally, we observe from ***Figure 15(a)*** that the different α-phases exhibit different levels of anisotropy in their single crystal responses. Plastic anisotropy plays an important role in multiscale materials modeling, both in the predictions of the effective anisotropic properties (e.g., effective yield strength [200-202]) as well as local responses (e.g., grain-scale responses controlling fatigue performance of the alloy [203, 204]). The ratio of the indentation yield strength parallel to the c-axis to the indentation yield strength perpendicular to the c-axis serves as a good indicator of the single crystal plastic anisotropy in the α-phases. It is seen from the results presented in ***Figure 15(a)*** that this ratio varies from 1.4 (for Ti64) to 2.0 (for Ti811). A statistical analysis of the data presented in ***Figure 15(a)*** did not reveal any strong correlations between the single crystal plastic anisotropy and the substitutional elemental compositions. The same analyses suggested that there is potentially an inverse correlation between the single crystal plastic anisotropy and the oxygen content. This observation is consistent with prior reports where it was hypothesized that the presence of interstitial oxygen contributes roughly equally to all of the potential slip systems in α-Ti. Indeed, if the increases in the slip resistances of the different slip systems are roughly equal, the percentages increases would be higher for the easy slips systems (compared to the harder slip systems) and thereby lower the single crystal plastic anisotropy, as revealed in the measurements shown in ***Figure 15(a)*** Clearly, further studies are warranted to critically evaluate this hypothesis.

Figure 15(b) presents a comparison between the indentation responses of Ti6242 and Ti6246. As explained earlier, the results from CP Ti are added to these comparisons to serve as a baseline. Given the small changes in the chemical compositions of the α-phases of these alloys (see ***Table 2)***, it is not surprising that the indentation responses are very

similar. The small differences in the trendlines shown in ***Figure 15(b)*** are seen to be smaller than the observed inherent variance in the measurements in the same plots. Therefore, we conclude that the indentation responses of the α-phases in these alloys are very similar to each other.

Aluminum is the most common alloying element in titanium alloys due to its high solubility in both alpha and beta phases. Addition of aluminum is expected to increase the strength of the alloy while lowering its density. However, these effects have not yet been quantified systematically in current literature. ***Figure 15(c)*** presents the measurements of the indentation yield strengths along with their trendlines for CP-Ti, Ti64 and Ti811 alloys. From the chemical compositions of the α-phases in ***Table 2***, it can be seen that the main contributors to the strength differences between these alloys come from the differences in their Al and O contents. Sakai and Fine [205-207] investigated the slip resistances of basal and prismatic slip systems in single crystals of Ti-Al alloys with aluminum composition in the range of 0.25 and 3 wt.% (0.44 and 5.2 at.%), and more recently, Williams et al. [197] performed compression tests at varying temperatures on Ti-Al single crystals with Al contents of 1.4, 2.9, 5 and 6.6 wt.% (2.46, 5.04, 8.55 and 11.54 at.%). Both these studies concluded that the slip resistances of both basal and prismatic $\langle a \rangle$ systems increase as the aluminum content in the Ti-Al alloy rises; however, the prismatic $\langle a \rangle$ systems exhibited a more pronounced effect. Results from the present work are in agreement with their findings as the differences in the mechanical response at all declination angles between CP-Ti and Ti64 and Ti811 can mostly be attributed to the variations in aluminum content. Furthermore, ***Figure 15(c)*** seems to suggest that the Al content in Ti811 increases the pyramidal $\langle c + a \rangle$ slip resistance much more than the basal or prismatic slip resistances.

We also observe that Ti64 presents the highest amount of vanadium among these alloys and presents the lowest crystal-level plastic anisotropy among all materials studied here.

Tin is generally recognized as a strong strengthening agent among its other non-transition peers (i.e., Ga, Ge, Bi, Al) [191] known for exhibiting a strong solid-solution strengthening effect on the α-phase of Ti [191]. The strengthening effect of Sn is particularly noticeable among its substitutional peers (including Al), especially at compositions above 3.5 at.% for temperatures around 300 K [208]. Factors such as the electronegativity difference between solute and solvent, atomic size difference, and lattice stability parameters (e.g., shear modulus) have been suggested to be intimately related to the solid-solution strengthening capability of non-transition alloying elements [191]. ***Figure 15(d)*** presents a comparison between the indentation responses between CP-Ti, Ti64 and Ti5-2.5. It can be observed that a difference of 0.95 at.% in Sn between Ti64 and Ti5-2.5 is enough to increase the c-axis indentation yield strength of the Ti5-2.5 by 11.4% despite the fact that Ti64 has a higher concentration of aluminum and oxygen.

Table 3. *Aluminum equivalence values calculated for all the primary-α compositions in wt.%, of all alloys in this work. Al_eq equation taken from[2].*

Alloy	Al_Equivalence
Ti811	9.63
Ti6242	9.719167
Ti5-2.5	6.662042
Ti6246	10.00675
Ti64	9.0495
CP-Ti	1.55

Rosenberg [209] described an aluminum equivalence relationship based on a creep stability threshold defined as 10% elongation and 20% reduction area after exposures of alloyed titanium to creep. He studied the individual effects of alloying elements on the stability of pure Ti and established that 3 wt.% Sn is equivalent to 1 wt.% Al in terms of their embrittling effects. Similarly, the effect of Zn and O were found to be additive with their effect being $1/6$ and 10 times that of Al, respectively. Recent work has investigated the relationship between these aluminum equivalences and mechanical properties such as flow stress [210, 211], tensile strength and fracture toughness [212]. Aluminum equivalences were computed for all the primary-α compositions in ***Table 3*** using the equation established in prior literature [2]. The dependence of the indentation yield strengths at declination angles Φ = 0° and Φ = 90° on Al equivalencies are presented in ***Figure 16***. It is seen that the indentation yield strengths showed a positive correlation with Al equivalencies, but a negative correlation with Mo equivalencies. More specifically, it was also noted that both correlations are stronger for the pyramidal $\langle c+a \rangle$ slip resistance, which dominates the indentation yield strength measurements at Φ = 0°, compared to the prismatic $\langle a \rangle$ and basal slip resistances, which dominate the indentation yield strength measurements at Φ = 90°. In other words, it re-emphasizes our earlier conclusion that the pyramidal $\langle c+a \rangle$ slip resistance exhibits higher sensitivity to composition, compared with the prismatic $\langle a \rangle$ and basal slip resistances. It is also noted that several of the correlations are relatively weak. This is to be somewhat expected as the Al equivalencies described above were not designed to correlate with the indentation yield strengths. However, the observed correlations suggest that there may be opportunities to establish similar equivalencies for CRSS values. This could be the focus of future work in this area.

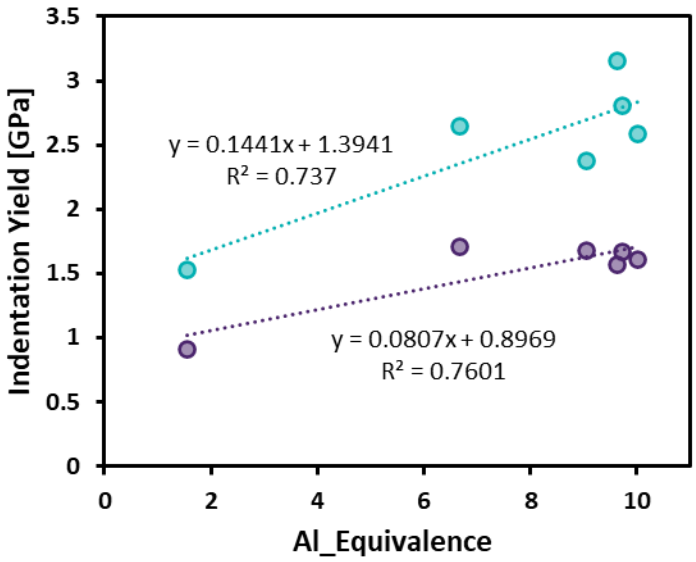

Figure 16. *Dependence of the indentation yield strengths at declination angles Φ = 0° and Φ = 90° on Al_equivalence values computed for the primary-α compositions of the alloys studied in this work.*

The results from this task served as modeling calibration data for the estimation of the intrinsic properties of the primary-α phase of the titanium alloys mentioned in this work, by implementation of the protocols described in section 2.3. The results from this two-step Bayesian framework applied to the data presented here, were published under the Title *"Mechanical Responses of Primary-α Ti Grains in Polycrystalline Samples: Part II—Bayesian Estimation of Crystal-Level Elastic-Plastic Mechanical Properties from Spherical Indentation Measurements"* by Castillo and coworkers [7]. A brief summary of the results is presented here as demonstration of the capabilities and veracity of the nano-indentation measurements of this work.

The finite element model of the indentation experiment was based on the following equations describing the crystal level plasticity on a deformable body and a rigid semi-spherical indenter under frictionless contact:

$$L^P = \sum_a \dot{\gamma}^a \, S^a, S^a = \, m^a \otimes n^a \qquad 14)$$

$$\dot{\gamma}^a = \dot{\gamma}_0 \left| \frac{\tau^a}{S^a} \right|^{1/m} sign(\tau^a) \qquad 15)$$

Due to the high levels of plastic anisotropy between different slip families in the hcp crystal presented in ***Table 4*** and the significant larger parameter space covering the expected ranges for each of these systems, a substantial increase of the FE model size and the necessary number of simulations was observed when using a commonly known FE mesh in which the elements are made progressively coarser as we move away from the primary indentation deformed zone towards the free boundaries of the sample. In order to address the above-mentioned difficulties, an improved FE model with higher computational efficiency was adopted. This new model introduced infinite elements (instead of coarser elements) designed to simulate the effect of an infinite elastic domain [7]. Similar approaches had been previously suggested in prior work [213-215] where significant reductions of the computational costs were acknowledged.

Table 4*. Slip families and slip elements considered for the crystal plasticity finite element simulations of the spherical indentation experiment [7].*

Slip System	Initial slip parameter	Slip elements	Number of slip systems
Prismatic	S_{pr}	$\{10\bar{1}0\}\langle 11\bar{2}0\rangle$	3
Basal	S_{ba}	$\{0001\}\langle 11\bar{2}0\rangle$	3
Pyramidal $\langle a\rangle$	S_{pyr-a}	$\{10\bar{1}1\}\langle 11\bar{2}0\rangle$	6
Pyramidal $\langle c+a\rangle$	S_{pyr-ca}	$\{10\bar{1}1\}\langle 11\bar{2}3\rangle$	12

For this work, a primary deformation zone of size 0.76 x 0.76 x 0.14 µm under the non-deformable indenter of radius 15.2 µm (consistent with the actual experimental procedures) was constructed using 13500 C3D8 elements on ABAQUS [216]. The deformation zones outside of the primary indentation were meshed using 2700 CIN3D8 elements (eight-noded hexahedral infinite elements). This new method required 101 to 136 minutes using 8 CPU cores on the Georgia Tech's Hive computer cluster to simulate the spherical indentation experiments on crystal if different declination angles. Indentation stress-strain curves were generated by imposing loading-unloading cycles along the indentation process in simulation of the ones happening in the actual indentation experiment.

Predicted equivalent plastic strain contours on a longitudinal section through the sample were plotted for each of the slip families included in the simulation. From such predictions, it can be concluded that the declination angle has a large influence on the slip activities in the primary deformation zone if the spherical indentation. Indentation parallel to the c-axis is dominated by pyramidal < c + a > slip activity along with contributions from the basal slip, and the basal and prismatic slip account responsible for the deformation

at declination angles between 45˚ and 90˚. This observations, along with the harder slip resistance of the pyramidal < c + a > slip, and the easier slip of the prism system, are responsible for the high and low indentation yield strengths at the extremes of the declination angle range covered in this set of simulations. These remarks are indeed consistent with the results from the spherical indentation experiments conducted in this work, and with prior literature reports [194].

The prediction of the elastic constants are presented in ***Figure 17***, and show lower levels of uncertainty for the C_{44}, followed by C_{33} and C_{11}. On the other hand, the relatively high uncertainty for C_{12} and C_{13} indicate a smaller influence of these elastic parameters on the indentation modulus across the orientation space. These estimations were found to be in good agreement with previously reported values [217-219], especially those computed for CP-Ti. Elastic constants reported for Ti6242 are also observed to fall within the standard deviation of the values reported in the present results. It is intuitive to think that a higher number of experimental measurements tend to strengthen the predictions of the intrinsic properties. This is in fact proved by the case of Ti64 which had the most available number of experiments (67) and Ti811 with the fewest (31). Additionally, the distributions of these measurements is of mayor importance, due to the high sensitivity of some of the single-crystal elastic parameters at declination angles regimes close to 0°. This also coincides with a higher uncertainty in the prediction of indentation yield strength in the $[10\bar{1}0]$ direction at which a fewer number of indentation measurements were attained.

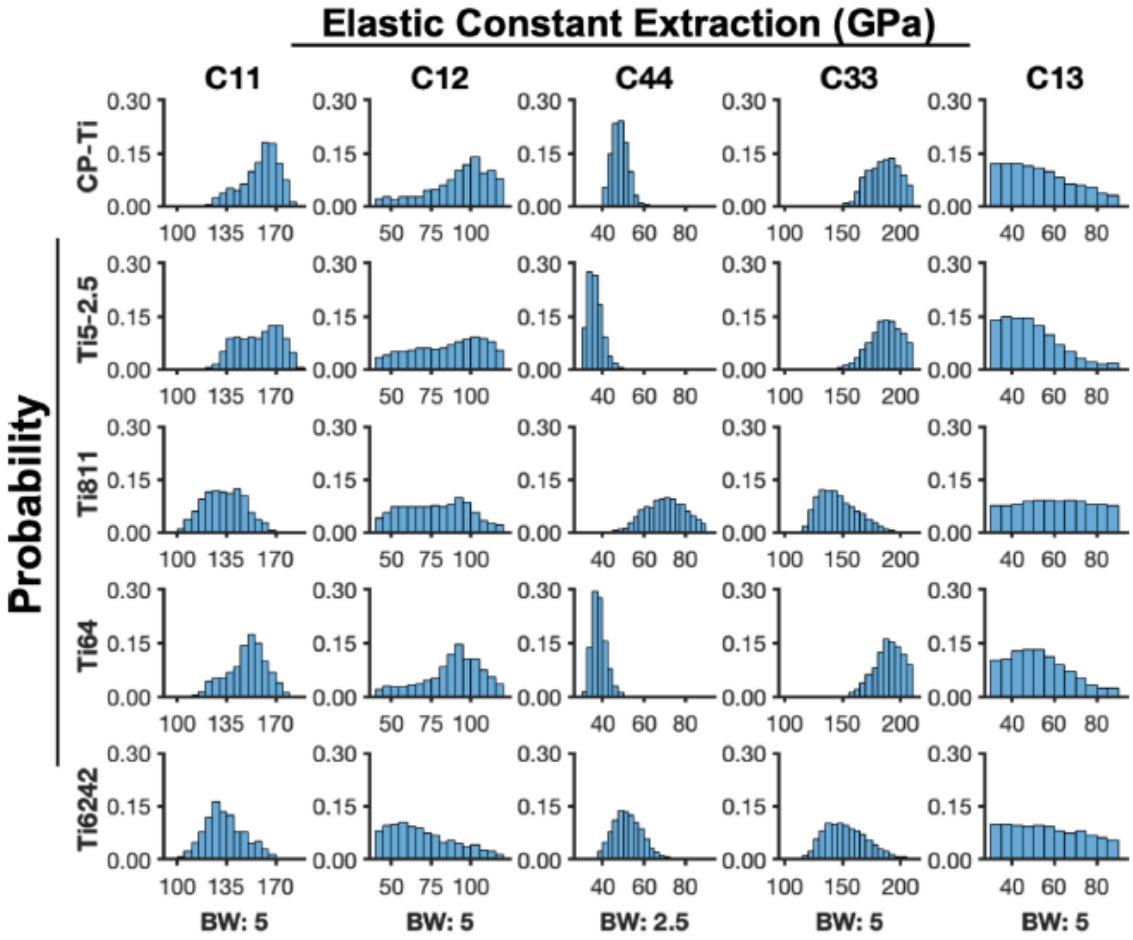

	C11 (GPa)	C12 (GPa)	C44 (GPa)	C33 (GPa)	C13 (GPa)
CP-Ti	159 ± 13	92 ± 19	48 ± 4	185 ± 13	53 ± 16
Ti5-2.5	158 ± 15	85 ± 22	37 ± 4	186 ± 13	49 ± 13
Ti811	133 ± 14	77 ± 20	70 ± 9	146 ± 17	60 ± 17
Ti64	150 ± 14	88 ± 18	38 ± 3	189 ± 12	53 ± 14
Ti6242	134 ± 14	70 ± 20	52 ± 7	153 ± 19	57 ± 17

Figure 17*. Distributions of the single-crystal elastic constants extracted for alloys in this work, and the corresponding mean and standard deviations.[7]*

The calculated slip resistances for each sample and their resulting distributions are presented in ***Figure 18***. The uncertainty for each of the slip systems is observed to be constant across all alloys and is reflective of the influence on the indentation yield to changes in the initial slip resistance parameters. Prismatic exhibiting the lowest uncertainty, basal and pyramidal $< c + a >$ with slightly higher uncertainty and pyramidal $< a >$ exhibiting the highest relative uncertainty. In general, good agreement is found between estimates obtained in this study and those reported in literature. For instance, the pyramidal $< c + a >$ slip ratios estimated for CP-Ti and Ti64, and the basal slip ratio for CP-Ti, all fall between the values previously reported. Finally, literature values reported for the basal slip ratio of Ti6242 and Ti64 are within a standard deviation of the estimated from this work

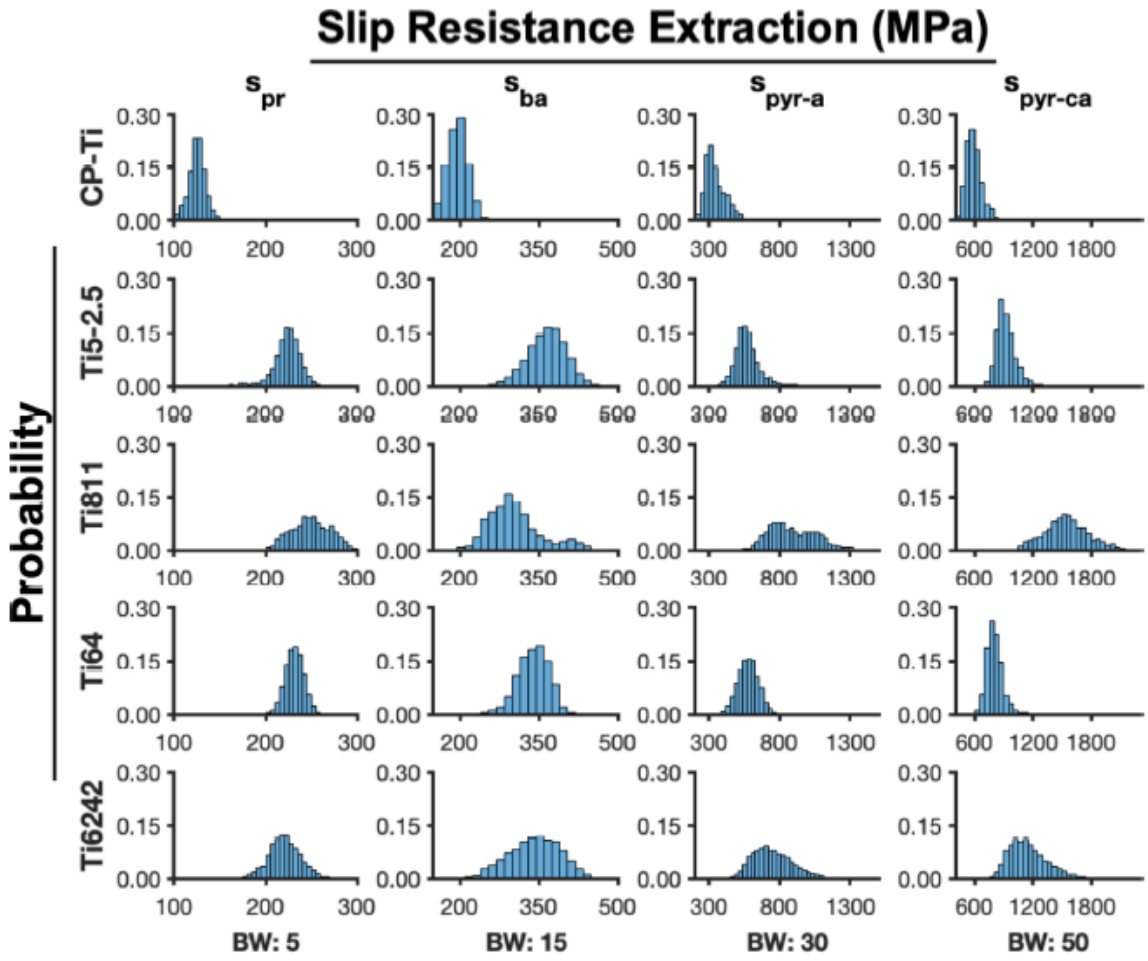

	s_{pr} (MPa)	s_{ba} (MPa)	s_{pyr-a} (MPa)	S_{pyr-ca} (MPa)
CP-Ti	125 ± 9	195 ± 20	346 ± 69	589 ± 77
Ti5-2.5	223 ± 15	366 ± 36	573 ± 96	921 ± 96
Ti811	249 ± 21	304 ± 49	894 ± 165	1546 ± 220
Ti64	231 ± 10	340 ± 30	579 ± 72	804 ± 82
Ti6242	221 ± 18	342 ± 49	748 ± 135	1150 ± 189

Figure 18*. Distributions of the single-crystal slip resistances extracted for alloys in this work, and the corresponding mean and standard deviations [7].*

CHAPTER 4 High-Throughput Grain-Scale Mechanical and Microstructure Characterization of Fully Basket-Weave Morphologies

4.1 Introduction

α-β Ti alloys have attracted significant interest from the scientific community due to their superior mechanical properties at lower densities and corrosion resistance, with many potential applications in the aerospace, bioimplant and nuclear energy industries [1, 8, 9, 12, 220]. The α-phase exhibits a hexagonal closed packed (hcp) crystal structure that is stable at low temperatures, while the β-phase exhibits a body-centered cubic (bcc) crystal structure stable at high temperatures. Thermo-mechanical processing of these alloys often produces diverse microstructures in which the a and b phases exhibit rich morphologies, which in turn control the overall mechanical response of the alloy [1, 82, 168, 221-223]. The different grain-scale morphologies observed in α-β Ti alloys can be classified as globular, lamellar, and basket-weave [9, 165, 166]. Since the α-β Ti alloys allow a broad range of alloying combinations, thermo-mechanical processing of these alloys often results in a rich and diverse set of microstructures exhibiting a broad range of mechanical properties [191, 224-227]. The β-transus temperature refers to the temperature at which an α-β Ti alloy fully transforms into β-phase. When the alloy is thermo-mechanically processed above the β-transus temperature and subsequently cooled at relatively high cooling rates, the microstructures exhibit a fully basket-weave morphology, which is comprised of secondary-α laths of multiple orientations in the prior β-grain.

The process-structure-property relationships in α-β Ti alloys have been studied in a number of prior experimental [11, 12, 90, 228-232] and modeling [233, 234] efforts. Although these studies have provided valuable insights, these still exist many fundamental

gaps in our understanding of these relationships. For example, while it is well understood that microstructural parameters such as lath thickness, lath aspect ratio, α volume fraction, β-grain size, and the average grain/colony size influence the bulk elastic-plastic properties of alloys [234-236], their precise roles are not yet quantitatively established. One of the main hurdles in establishing this core knowledge base comes from the high interdependence among the microstructural features mentioned above. It has not been possible to modify systematically one microstructural parameter at a time (i.e., keeping the others fixed) in the synthesis of these alloys, making it difficult to determine quantitatively the role of each microstructural parameter on the bulk mechanical response of the alloy.

The ability to capture and define the grain-scale mechanical response from the different Ti morphologies presents a great value in the materials design field, not only because it reduces the number of microstructural features, but also because it opens the door to the prediction of bulk properties using computational models that take as variables the grain-level properties of the different constituents in the microstructures. These models not only offer the versatility of evaluating an infinite range of microstructures, but also come without the costs and time struggles that are always associated with experimental procedures. Ideally, for a basket-weave morphology, a testing method that can simultaneously capture the contribution and interaction between a and b laths into the grain-scale elastic and plastic behaviors is desired. Tensile [90, 233] and micro-hardness [231, 236] experimental protocols have been previously used to characterize fully basket-weave Ti morphologies. From these, only the later can be used to obtain grain-scale measurements, however, it only provides one value that corresponds to the material's flow stress after some level of plastic deformation has already been achieved, lacking substantial

information about the deformation process. Even though compression tests on micropillars [17-21] and bending tests on micro-cantilever beams [182, 183] have been used in Ti single crystals with morphologies other than basket-weave, the use of Focused-Ion Beam (FIB) for the specimen construction has been associated with potential harmful impact on the experimental measurements [22].

Furthermore, the currently used protocols for the quantification of the complex microstructures in these alloys require multiple manual steps, often involving the counting of intercept lengths on randomly placed straight lines on the micrographs [235, 237]. Even though various standards have been stablished for microstructural characterization based on images [137, 238-240] and multiple software packages [235, 241, 242] are now available to assist in these protocols, they still incur significant time and effort. This is because the protocols require segmentation of the images before the desired microstructure statistics can be extracted reliably. And even in cases where the protocols can be validated, multiple specimens can be associated with similar values of these features while the microstructures are still quite different, as they generally lack orientation information which is known to heavily influence on the mechanical responses [6]. As a result, there is often large variance in the reported values of the different microstructure measures identified earlier, even for a specific alloy with a specified processing history.

In this work, we address these challenges identified above by using the recently developed protocols by Kalidindi and Pathak [34, 36] which have exhibited tremendous potential at capturing the grain-scale mechanical response of several materials in the form of indentation stress-strain (ISS) curves obtained from load displacement data measured in spherical indentation experiments. One of the advantages of this methodology is its multi-

resolution nature, that allows control on the material volume to be evaluated [38-41, 46, 243]. This is of much relevance for this work as we wish to capture the response from an adequate number of laths that represent the behavior of the grain, while allowing multiple tests within the grain for repeatability evaluation. These are well stablished protocols that have probed to generate highly consistent and reproductible measurements in both cubic [39, 43, 44] and hexagonal [5, 41, 243] crystal structures, and are relatively simple to conduct in high-throughput sequences that require the same sample preparation steps as for microscopy purposes. A recent study used these experimental protocols on titanium's primary-a globular grains from five different chemistries [243]. This study was successful at evaluating the grain-scale mechanical properties of this phase as a function of the HCP crystal orientation, as well as determining of the corresponding critically resolved shear stresses (CRSS) and the elastic constants [7].

Additionally, we suggest that the microstructure characterization challenges be approached using the Materials Knowledge System (MKS) protocols [99, 151, 153, 244-246] which utilizes two-point statistics for a complete and systematic quantification of the material structure [138, 245, 247]. This calculation provides the probability of finding two unique local states (a- and b-phases for our present case study) separated by a vector r. Specifically, the Rotationally Invariant adaptation of these spatial correlations will be employed [6], as basket weave microstructures are known by presenting high levels of directionality. Following this step, a low dimensional representation of such statistics is normally implemented in the constructions of any model. Two-point statistics have successfully been employed previous microstructure classifications on several materials classes [244, 245, 248] for the construction of process-structure and structure-property

linkages [95, 151, 152] . A more detailed explanation of this protocol will be provided later in section 4.2.4.

In this paper, we exploit the benefits of advanced grain-scale microstructure quantification and multiresolution mechanical characterization protocols on ten unique fully basket-weave samples from four different titanium chemistries. Specifically, we will first implement the spherical indentation experimental and analytical procedures to characterize the mechanical properties of these specimens. And finally, we employ the steps defined by the MKS framework for the quantification and unsupervised classification of these microstructures.

4.2 Methods and Materials

4.2.1 Materials and Sample Preparation

The materials selected for this study were alpha-beta Ti alloys Ti6Al-2Sn-4Zr-6Mo, Ti6Al-2Sn-4Zn-2Mo, Ti-8Al-1Mo-1V and Ti-6Al-4V. All of these alloys are of great relevance for the aerospace and gas turbine industry due to their hardenability and strength retention at high operating temperatures. As a consequence of the difference in their allying elements content, they have shown to present very distinct microstructures and mechanical responses for similar process parameters [249, 250] which is ideal for the present study. Specimens with $length \times width \times height$ dimensions of $10.0\,\text{mm} \times 2.0\,\text{mm} \times 20.0\,\text{mm}$, $10.0\,\text{mm} \times 10.0\,\text{mm} \times 5.0\,\text{mm}$, $20.0\,\text{mm} \times 10.0\,\text{mm} \times 10.0\,\text{mm}$ and $10.0\,\text{mm} \times 5.0\,\text{mm} \times 8.0\,\text{mm}$ respectively, were cut from larger bulk pieces. Prior to heat treatment, all specimens were individually encapsulated in quarts tubes backfilled with argon to create oxygen depleted environments. Fully basket-weave morphologies were

desired to keep the same average chemical compositions across all specimens of the same alloy group. For this reason, all samples were heat treated at temperatures above their beta transus to produce fully transformed samples, and then cooled at various cooling rates to achieve a variety of basket-weave morphologies. Following the cooling step, each sample was reheated to a second temperature below the β-transus and held to allow equilibrium phases to form. The samples were then air cooled. Details of the heat treatments conducted in this study are provided in ***Table 5***. Heat treatments were conducted using a Thermo Fisher Scientific, Lindberg/Blue 1100 °C Box furnace.

Table 5*. Summary of the heat treatments heat treatments applied to Ti6242, Ti6246, Ti811 and Ti64 specimens to produce the fully basket-weave microstructures used in this study.*

		Heat Treatments	
	Sample	**Primary Treatment**	**Secondary Treatment**
Ti6242	**I**	1030 °C – 30 min - Cooled on K-wool	700 °C - 4 hrs - Air Cooled
	II	1030 °C - 30 min - Cooled on Concrete	700 °C - 10 hrs - Air Cooled
	III	1030 °C - 30 min - Water Quenched	700 °C - 4 hrs - Air Cooled
Ti6246	**IV**	1010 °C - 30 min - Furnace Cooled	-
	V	1010 °C - 30 min - Boiling Water	700 °C - 12 hrs - Air Cooled
	VI	1010 °C - 30 min - Cooled on K-wool	600 °C - 12 hrs - Air Cooled
Ti811	**VII**	1175 °C - 30 min - Cooled on Concrete	700 °C - 12 hrs - Air Cooled
	VIII	1175 °C - 30 min - Water Quenched	700 °C - 4 hrs - Air Cooled
Ti64	**IX**	1020 °C - 30 min - Boiling Water	700 °C - 12 hrs - Air Cooled
	X	1020 °C - 30 min - Water Quenched	700 °C - 4 hrs - Air Cooled

As mentioned before, sample preparation for the indentation experiments uses the same standard metallography procedures as for imaging purposes. A flat and defect-free surface is desired as sample preparation and surface roughness have been observed to influence the

quality of the spherical indentation results [187]. Chemo-mechanical preparation of the samples typically consists of two stages: grinding and polishing. In the first one, silicon carbide papers starting from 800 grid, and systematically decreasing up to 2400 grid are used. The polishing sequence starts with 9, 3, and 1 μm diamond suspension, and finalizes with 12 hours of vibro-polishing in a mixture consisting of 1 part of 0.06 μm colloidal silica, 1 part of hydrogen peroxide and 4 parts of water.

4.2.2 Mechanical Characterization

Spherical indentation experiments were conducted at room temperature on a Nano-Indenter G200 by Keysight. Maximum load was kept constant for all experiments at 10 N and the experiments were performed at a nominal strain rate of 0.05 s^{-1}. ***Figure 19*** presents the schematics of the spherical indentation geometry, along with an example of a typical load-displacement and the equivalent indentation stress-strain curves from an experiment conducted on fully basket-weave specimen. For this specific sample, the maximum indentation depth was recorded as 3139 nm. A spherical indenter with diamond tip of radius 500 μm was used for all experiments in this study. This indenter size was selected as it allowed to capture the response from multiple laths within the basket-weave grains. For all tests conducted here, the contact radius between the indenter and the material was calculated to be between 22.7 and 30.5 μm at the point where permanent deformation had already been imposed. SEM images of indentation imprints on two different samples are provided in ***Figure 20*** as graphical illustrations of these of these length scales. The estimation of this contact area is based on the Hertzian theory of contact [37] as described in section 2.1.2. Due to grain sizes from these samples ranging between 100 μm to 1000 μm in diameter, indentation experiments were always positioned well away from the grain

boundaries to avoid the influence from neighboring grains and grain boundaries in the results. In cases where the grains were large enough, multiple indentation tests were conducted within the same grain to evaluate repeatability of the results. The distance between indents within the same grain was always kept at a minimum of ten times the expected contact radius at yield. A minimum of 40 valid tests were carried out for each specimen.

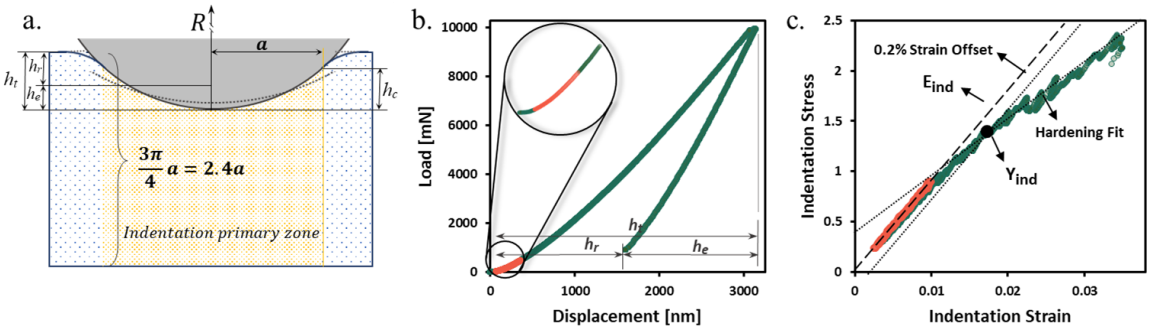

Figure 19. *a) Schematic of the spherical indentation experiment depicting the maximum-depth and final geometries. b) Load-displacement curve from an experiment on a fully basket-weave sample with recorded CSM signal and c) its corresponding indentation stress-strain curve. The selected elastic segment is highlighted in orange for comparison.*

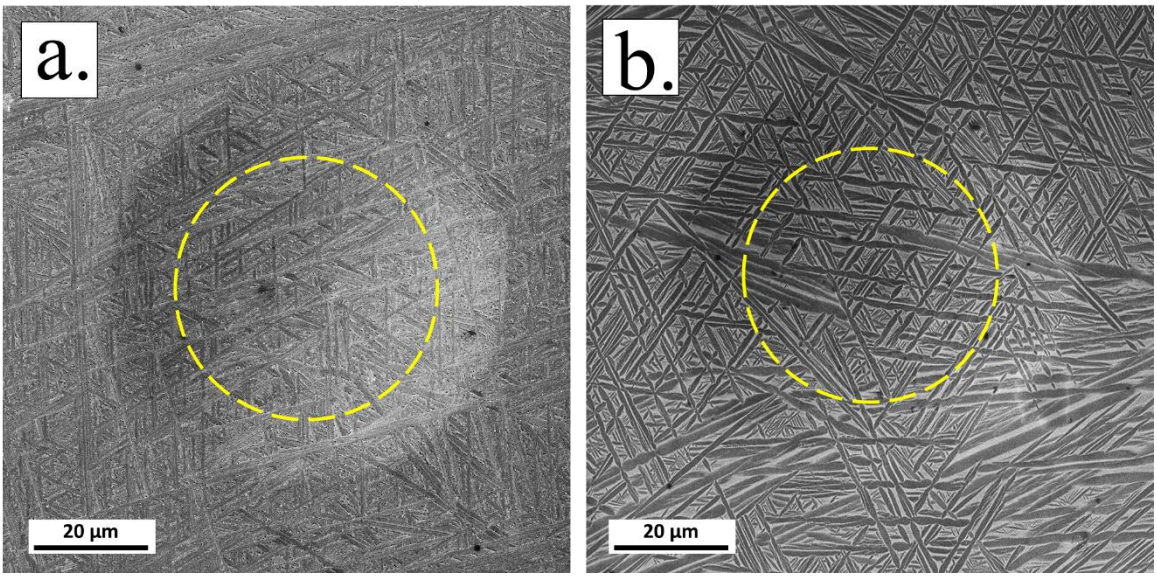

***Figure 20**. SEM images of the indentation imprints for two of the samples in this study, showing the size of the contact area at yield, highlighted by the yellow circles. a) Test on sample I with contact radius at yield of 23.024 µm and b) test on sample IV with contact radius at yield of 22.462 µm.*

4.2.3 Microstructure Characterization

A Tescan Mira3 field emission scanning electron microscope (FE-SEM) was used to capture back-scattered electron (BSE) and electron back-scattered diffraction (EBSD) microstructure images as the first step in the microstructure characterization process. In order to collect high resolution images of the small features in the microstructures, an accelerating voltage of 15 kV was used for BSE images, while accelerating voltage of 20 kV was used to enhance contrast of Kikuchi patterns in the EBSD characterization. The image dimensions were kept constant for all BSE scans at $2048\ x\ 2048$ pixels. All images were collected with the same view-fields ($30\ x\ 30\ \mu m$) in order to simplify the

interpretation of the rotationally invariant 2-point correlations. At least 20 BSE images were collected from each sample, each of them corresponding to a unique random grain, where overlap and edge effects were avoided.

4.2.4 Microstructure Quantification

The first stage in the microstructure quantification process was to convert the grayscale BSE images into binary representations using a series of imaging processing steps based in the protocols described by Iskakov and Kalidindi [4]. The first of these steps corresponds to the application of a Gaussian filter (`imgaussfilt` function in MATLAB) to decrease the pixel-to-pixel noise in the images. A standard deviation $\sigma = 0.75$ was used for all images. The second step involved the calculation of locally adapted thresholds. These varying thresholds are calculated based on the local mean intensity in the neighborhood of each pixel [251]. In this case, the "adaptthresh" function is used immediately before the "imbinarize" function from the same image processing toolbox to complete the binarization step. Since the microstructures studied here represent very distinct basket-weave morphologies, the sensitivity and neighborhood size were manually chosen for each set of images in order to properly capture the details of each microstructure.

In order to determine the most appropriate combination of sensitivity and neighborhood size parameter for the thresholding step, a systematic evaluation of the resulting segmented image was conducted in which precision and recall scores were assigned to each thresholding parameter combination. For this evaluation, a ground truth segmentations of the to-be-segmented image is necessary. One ground truth image was manually obtained from a randomly selected image from each specimen, and was created by utilizing the

layering capabilities of the openly commercial software Adobe Photoshop©, where each pixel was manually classified into one of the two local states, secondary-α-Ti and β-Ti. Although a tedious and time-consuming job, this step offers the expert initial step into a more quantitative assessment of the segmentation results. This is of great value when no exact solution can be obtained from more analytical options such as thermodynamical predictions of the volume fractions, lath thickness or lath aspect ratios. These microstructural parameters are of great importance in the present work and therefore the correct segmentation of the micro-images is of critical importance. It is important to mention here that, although other approaches for the determination of the α- and β-phases volume fractions (such as x-ray diffraction [252]), traditional stereological procedures on SEM and optical microscopy images are still the choice of preference for the construction of this type of microstructure-property relationships [90].

The Precision Score offers the success rate of segmentation by comparing the segmented image to the ground truth. The ratio is mathematically defined as the number of correctly segmented pixels over the total amount of segmented pixels (regardless of whether they are correct or wrong). On the other hand, the Recall Score grades how close the segmented image is to the grown truth by finding the ratio between the number of correctly segmented pixels over the total number of pixels in the ground truth [Abel]. Ideally, both of these numbers should be close or equal to 1 for a perfect segmentation. ***Figure 21*** shows as schematic of this assessment in which the ground truth corresponds to the left part of the square (i.e., relevant elements), and the segmented image is represented by the circle (i.e., selected elements). These scores were calculated for varying values of the sensitivity and neighborhood size and plotted in the same figure to determine the best

combination of parameters. In addition to these quantitative evaluations, overlay and contour techniques were used for visual inspection of the segmented micrographs. In the segmented microstructures, the regions shown in black corresponds to secondary-α-Ti phase, and the white regions represents β-Ti.

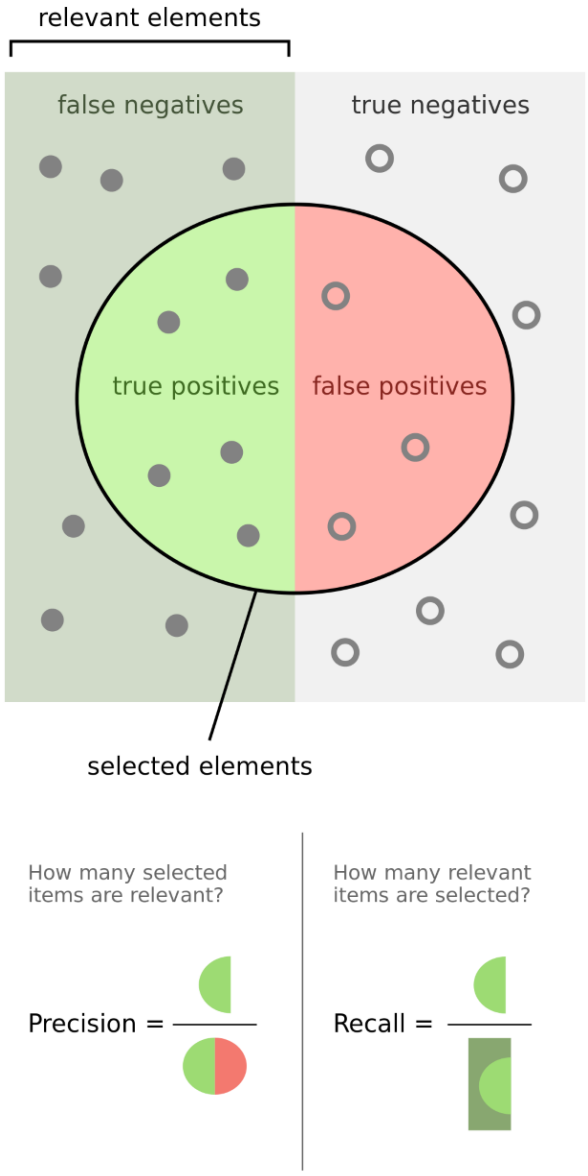

Figure 21. *Graphical explanation of the precision and recall scores that grades the segmentation quality by comparing the segmented image to a ground truth of the same micrograph.*

The second stage of the microstructure quantification process refers to the computation of microstructure statistics. The simplest one being 1-point statistics, provides the probability of finding a specific local state, h, in any random location on the microstructure. This is equivalent to the commonly known area fraction of such local state. The next degree of calculation corresponds to 2-point spatial correlations, also known as 2-point statistics [153]. In this case, the probability of finding two unique local states, h and h', separated by a vector r, is determined. The main advantage of this approach over the more of traditional stereological procedures, is a more complete morphological characterization that captures information defining chape, size and distributions between the present phases.

Due to the relative directionality between the secondary-α laths in the basket-weave morphology, a method capable of preserving this relative directionality while discarding the observers reference frame sensitivity, was necessary. As previously explained in more detail in section 2.2.3, the rotationally invariant two-point spatial correlations are obtained by simply taking the conventional two-point spatial statistics calculated from the segmented microstructural image and applying a series of coordinate transformations, DFT's and inverse DFT's, to remove the effects of a potential observers rotation (or simply the intrinsic rotation from each basket-weave grain), and to shift the dominant information of the microstructure to align with $\psi = 0°$, where ψ represents a relative angular difference between the points in the dataset [6]. By applying these modifications. We remove one dimension prior to subjecting the statistics from all segmented images to the Principal Component Analysis.

4.2.5 Principal Component Analysis

Principal Component Analysis (PCA) is the process of transforming the rotationally invariant two-point statistics (or the conventional two-point statistics) from the previous step, into a new coordinate system in which the coordinate axes (i.e., principal components) are orthogonal to each other and ordered in terms of the variance represented by each component. This means that the first component (PC1) carries the largest amount of variance between the data, being followed by PC2 with the second largest variance. As a result, PCA provides a data-driven low-dimensional representation of the original data. Principal component analysis has been previously adopted in the process of stablishing process-structure-property linkages as it allows for a low dimensional representation of the microstructure statistics [38, 94, 151].

Mathematically, this dimensionality reduction can be expressed as,

$$f[k,r] = \sum_{i=1}^{R^*} \alpha[k,i]\ \phi[i,r] + \bar{f}[r] \qquad 16)$$

Where the rotationally invariant two-point statistics from all microstructures are reorganized into a single array $f[k,r]$ where $k = 1, 2, 3, \dots, K$ numerates all the microstructures in PC space, and every voxel in each correlation map would be an entry in this vector. Here, R^* represents the total number of retained statistical components and $\bar{f}$ is the average of the two-point autocorrelations in the ensemble. $\phi[i,r]$ denotes the direction of the new linearly transformed reference frame (i.e., basis vectors), and $\alpha[k,i]$ are the coordinates, (i.e., PC scores) in the new frame.

4.3 Results and Discussion

α-phase plates form either by nucleating a grain boundaries, by branching out from grain boundary allotriomorphs (GBAs) (high-angle grain boundary areas of the parent β-phase), or by expanding from intragranular locations in an isolated manner or in a group [253]. In the first scenario, the α-phase regions are denoted as primary side plates, whereas in the last two, secondary-α plates are formed instead. Intragranular plates obey very strict orientation relations as defined by the Burgers orientation relationship [254].

Our interest in this work lays on this type of intergranular morphologies which account for the majority of the grain and microstructure of the sample. Here, a total of 10 fully basket-weave microstructures were chosen from four different chemistries and can be appreciated in ***Figure 22***. Due to the nucleation rate and the growth kinetics of the secondary-α laths during the heat treatment processes, especially the cooling steps, the resulting microstructures exhibit a distribution of lath geometries and sizes across samples. Some of these differences are also applicable to the remaining traces of the original β-phase. All of these microstructures, adhere with the fractal geometry characteristic of basket-weave morphologies defined as continuous partition of the prior β-grain into smaller and smaller volumes of repeated lath patters.

The complexity of these morphologies leads to one of the fundamental objectives of the present task which aims to define and capture the basket-weave “lath microstructure” as a whole, instead of defining microstructural parameters such as the ones named earlier in the introduction of this section [234-236].

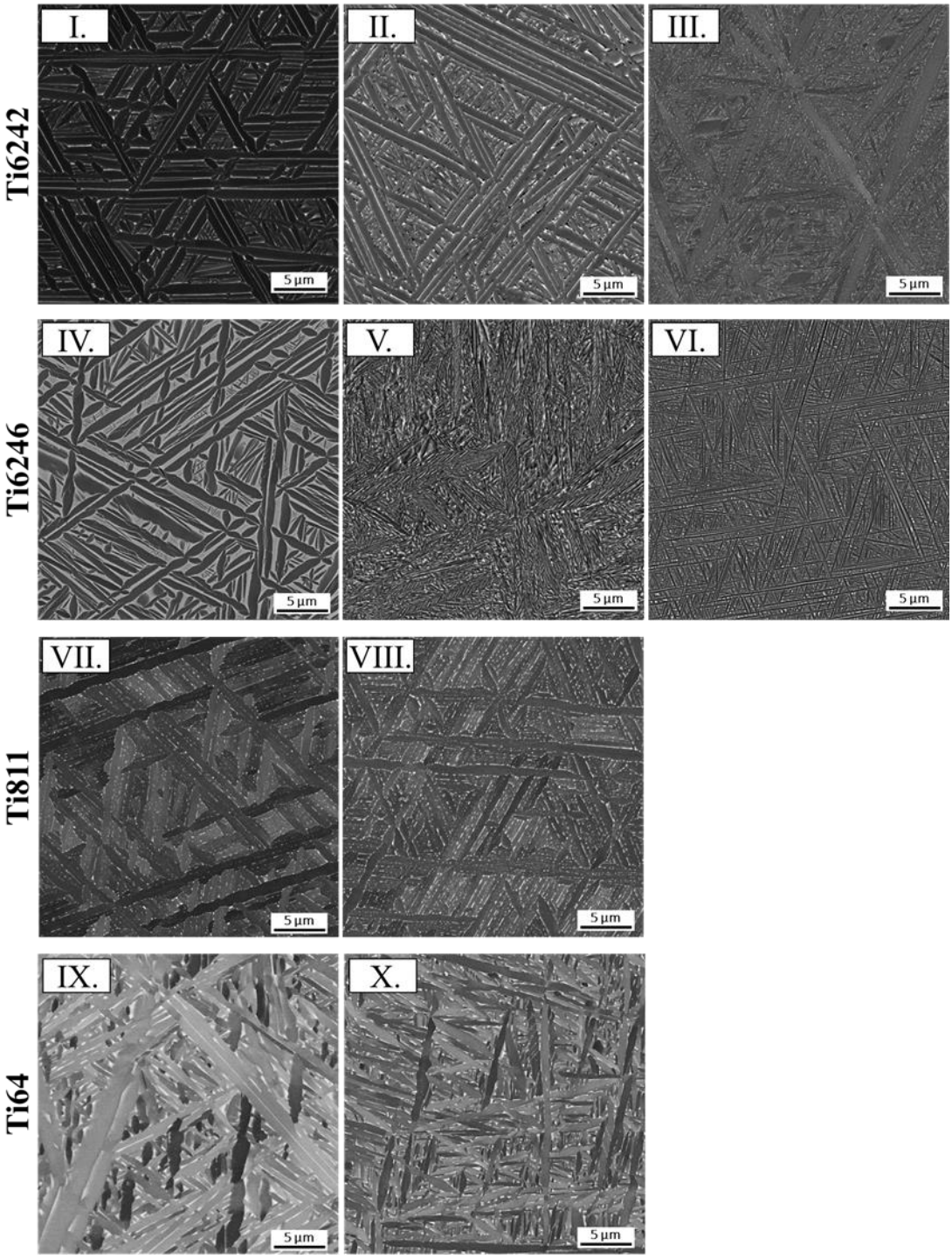

Figure 22. *Representative BSE microstructural images form each fully basket-weave specimen used in this task. All images with view-field of 30µm and size 2048x2048 pixels.*

4.3.1 Orientation Dependence

In Task 1, Grain orientation was found to present a remarkable influence on the resulting grain-level mechanical behavior of the primary-α phase of Ti alloys. In this task we wish to explore the dependability of the basket-weave morphology on the different secondary-α variants present in a grain, and quantify it to be compared with the previously found results. It is worth to stop here for a moment and mention that, although the Burgers orientation relation [254] has been widely accepted to govern the orientation relationship between the prior-β and the newly transformed secondary-α laths, this rule is not operative in all cases. Small variations have been observed in the multiple diffusional transformation studies [255-257] leading to more accurate definitions. Relatively recently studies on Ti- and Zr-bases alloys by D. I. Potter [258], yielded an updated orientation defines as:

$$[00\bar{1}]_{\beta} \parallel [2\bar{1}\bar{1}0]_{\alpha}\,;\; [110]_{\beta} \parallel [0001]_{\alpha}\,;\; [1\bar{1}0]_{\beta} \parallel [0\bar{1}10]_{\alpha}$$

Which can only be stablished if the small angle between $[110]_{\beta}$ and $[0001]_{\alpha}$ is well determined. This means that whether the Potter or Burger condition is met, depends on the correct measurement of this angle. Although it is not in the scope of this work to determine the veracity of any of these relationships, we consider that it is worth clarifying this information before we present the results as the data presented here can potentially be used in computational simulations that predict the mechanical behavior of basket-weave grains based on their orientation characterization, or vice versa.

Another common relationship characteristic of basket weave morphologies corresponds to the 60° misorientation between each of the α-phase variants in the microstructure. ***Figure 23*** presents the EBSD scan from a single crystal in a fully basket-

weave Ti64 sample. The figure on the right corresponds to the misorientation plot resulting from point-point and point-to-origin comparisons, red and blue lines respectively. Specifically relevant to us, the point-to-origin measurements between any two of the secondary-α laths (not only from this EBSD scan, but from all the other microstructures used in this task) were comparable, depicting this orientation relationship between α laths.

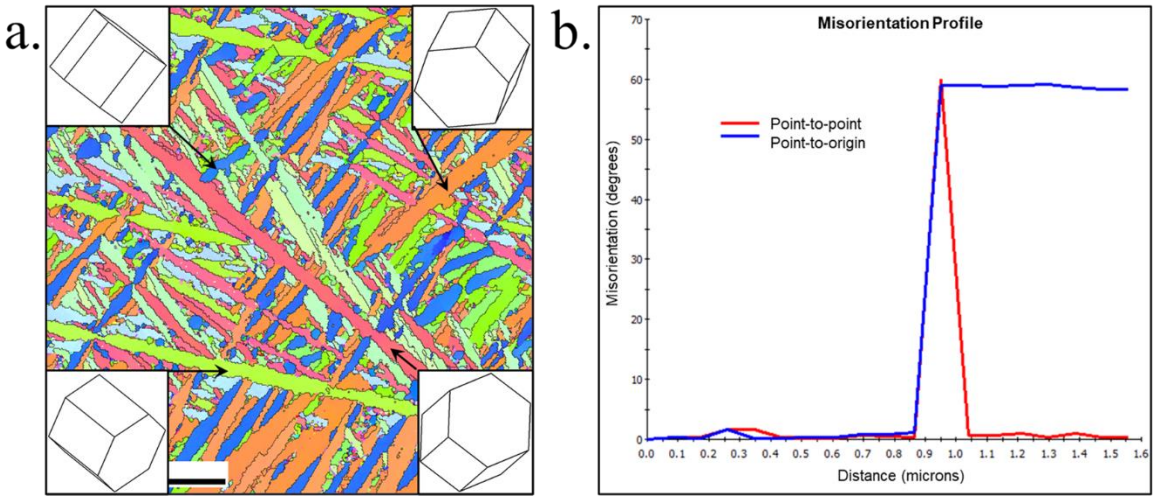

Figure 23*. a). Single grain EBSD scan from a fully basket-weave Ti64 microstructure and lattice orientation schematics of the secondary-α laths. b). Point-to-point and point-to-origin misorientation plot between each of the secondary-α variants.*

Continuing with the orientation characterization of our specimens, single-grain EBSD scans were collected from randomly selected grains for which spherical indentation experiments were later conducted. ***Figure 24*** contains a total of 8 EBSD scans from two different samples and their corresponding inverse pole figure triangles. This analysis allowed for a more cost and time effective way to verify that grains containing a wide variety of orientations were being captured.

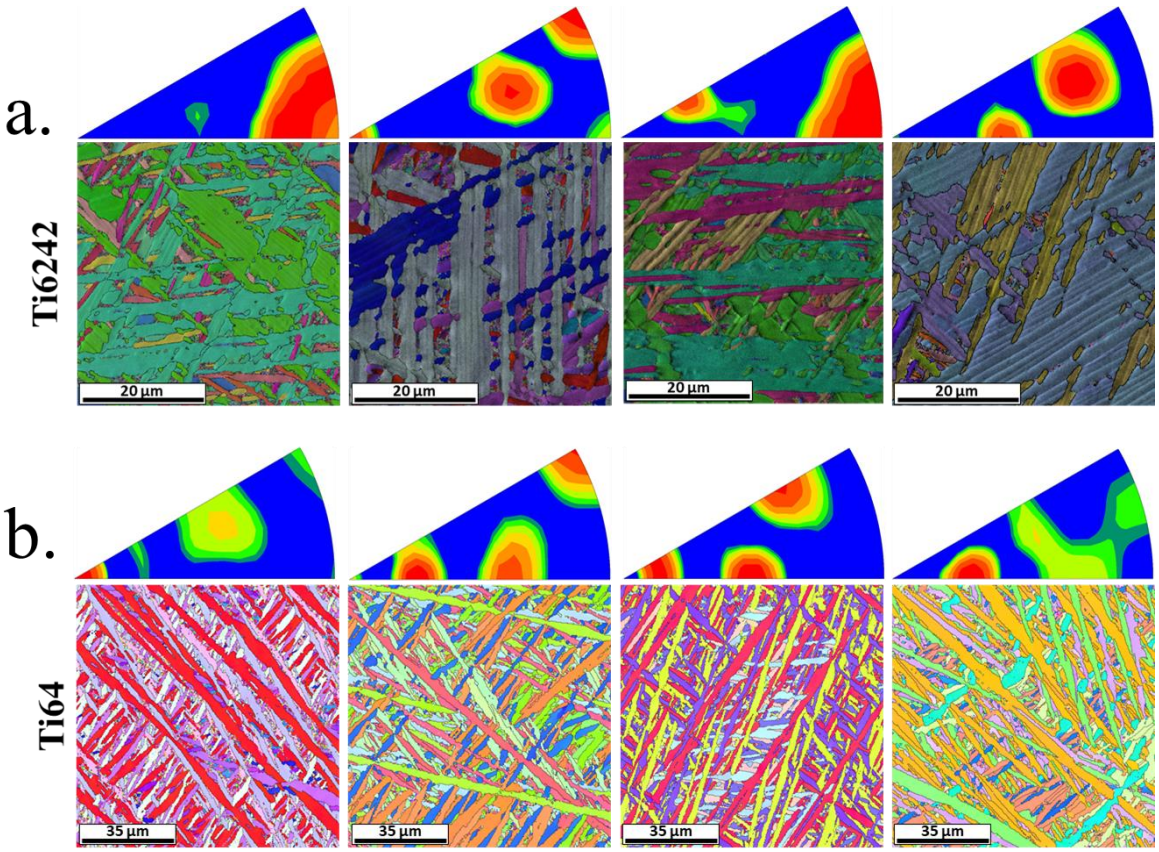

Figure 24. *EBSD scans from four unique grains and their respective inverse pole figure triangles from a). Ti6242 and b). Ti64 specimens.*

The main benefit from these evaluations is perhaps that they allowed for the verification of the spherical indentation results. Based on the results from Task 1, one would expect indentation strength values from grains with predominant presence of the [0001] secondary-α lath orientations, to be higher than those from grains with predominantly $[10\bar{1}0]$ or $[2\bar{1}\bar{1}0]$ orientations. This theory is in fact confirmed when we look at the indentation stress-strain curves from three unique grains with predominant orientations on each of the three corners of an hcp inverse pole triangle in ***Figure 25***.

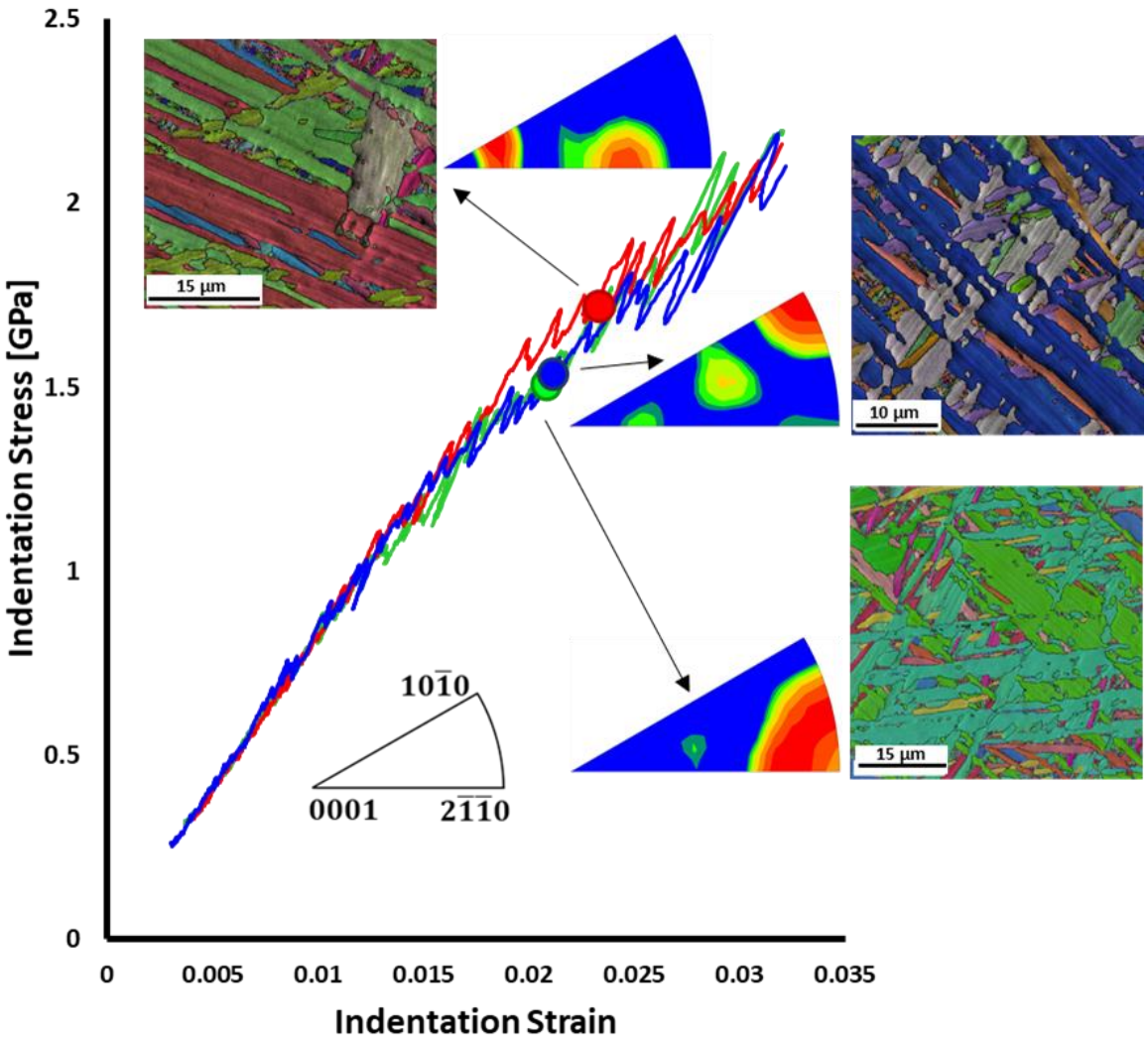

Figure 25. *Indentation stress-strain curves from three unique grains in Sample I evidencing the influence of the grain-level texture in the corresponding mechanical properties.*

All the indentation stress-strain curves in this task are using the same definition of indentation yield which corresponds to the intersection from a 0.2% offset parallel from the elastic line and the back-extrapolation of the points depicting plastic deformation as explained in ***Figure 19 (c)***. Therefore, the mechanical behavior from a grain that has a more pronounced frequency in the $\Phi = 0°$ corner, is represented by the red line in ***Figure 25*** that corresponds itself to a higher indentation yield value (red circle). Similarly, the

indentation yield from the grains with $\Phi = 90°$ are evidenced with blue and green circles having lower values.

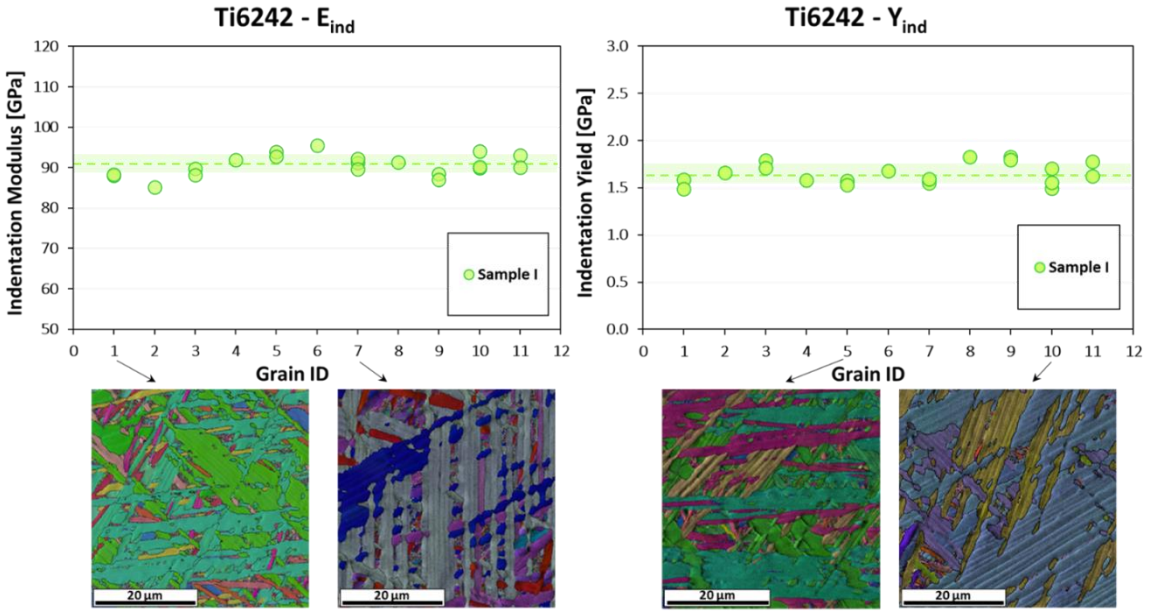

Figure 26. *Experimentally measured indentation modulus and indentation yield values from different grains of sample I. Means and standard deviations of the measurements are also plotted for reference. At the bottom, EBSD images corresponding to four unique grains.*

Now that the influence of the grain-level orientation has been evidenced, we now compare the variance between the mechanical properties of multiple grains within the same sample. ***Figure 26*** presents the indentation modulus and indentation yield strength values from 11 unique grains in Sample I, each of them with their unique orientation combinations of secondary-α variants. When the size of the grain allowed for it, more than one indentation test was performed within the same grain for the evaluation of repeatability, as it is the case of grains 1, 3, 5, 7, 9, 10 and 11. In this figure, the mean and standard deviation of the data points are also presented in the form of a broken line and a box in a lightshade

of green color behind the experimentally measured data points. For this specific sample, the mean indentation modulus was found to be 90.54 ± 2.44 [GPa] and the mean indentation yield strength 1.63 ± 0.11 [GPa]. For comparison, the standard deviations from the spherical indentation measurements on the Ti6242 primary-α grains in Task I, were measured to be 8.98 [GPa] and 0.38 [GPa] for indentation modulus and indentation yield strength respectively.

This means that the variation in the measurements from the basket-weave grains is reduced to almost a third from that found in Task I, leading to the conclusion that basket-weave mechanical properties are homogenized across all grains in a sample and are less sensitive to the lath orientations. A compilation of all the measurements in this task are presented in ***Table 6*** along with the data variances from the experiments in Task I for comparison (mean values are also provided in light gray color although no meaning or value is expected from them) to strengthen this statement across different alloys. In the case of Ti811 for example, the standard deviation from measurements on α-phase grains is up to four times higher than those from basket-weave grains.

Table 6. *Experimentally measured indentation modulus and indentation yield values and their corresponding means and standard deviations for all the fully basket-weave specimens in this work. The standard deviation from the spherical indentation measurements on the primary-α phases is also provided for comparison.*

Fully Basket-Weave Spherical Indentation Results					
Sample		E_{ind} [GPa]	E_{ind} Std [GPa]	Y_{ind} [GPa]	Y_{ind} Std [GPa]
Ti6242	I	90.54	2.44	1.63	0.11
	II	94.10	4.35	1.97	0.14
	III	98.49	2.05	2.22	0.18
	Primary-α	111.80	8.98	1.80	0.38
Ti6246	IV	99.62	1.81	1.68	0.10
	V	96.30	2.78	2.20	0.11
	VI	106.16	1.41	2.49	0.09
	Primary-α	118.17	8.27	2.09	0.36
Ti811	VII	10587	3.03	1.99	0.15
	VIII	104.86	3.30	2.26	0.22
	Primary-α	116.04	12.28	1.91	0.63
Ti64	IX	105.53	2.80	1.72	0.11
	X	100.21	2.01	2.08	0.13
	Primary-α	109.90	12.15	1.76	0.32

4.3.2 Lath Morphology Dependence

Moving into the lath morphology dependence, an important step for a successful microstructure characterization is the segmentation process. In the search for a qualitative assessment method for the segmentation process, the precision and recall scores are adopted to determine the best combination of sensitivity and neighborhood size parameters

in the segmentation thresholding step. For this step the construction of ground truth segmented images was carried out for one microstructure image from each sample set.

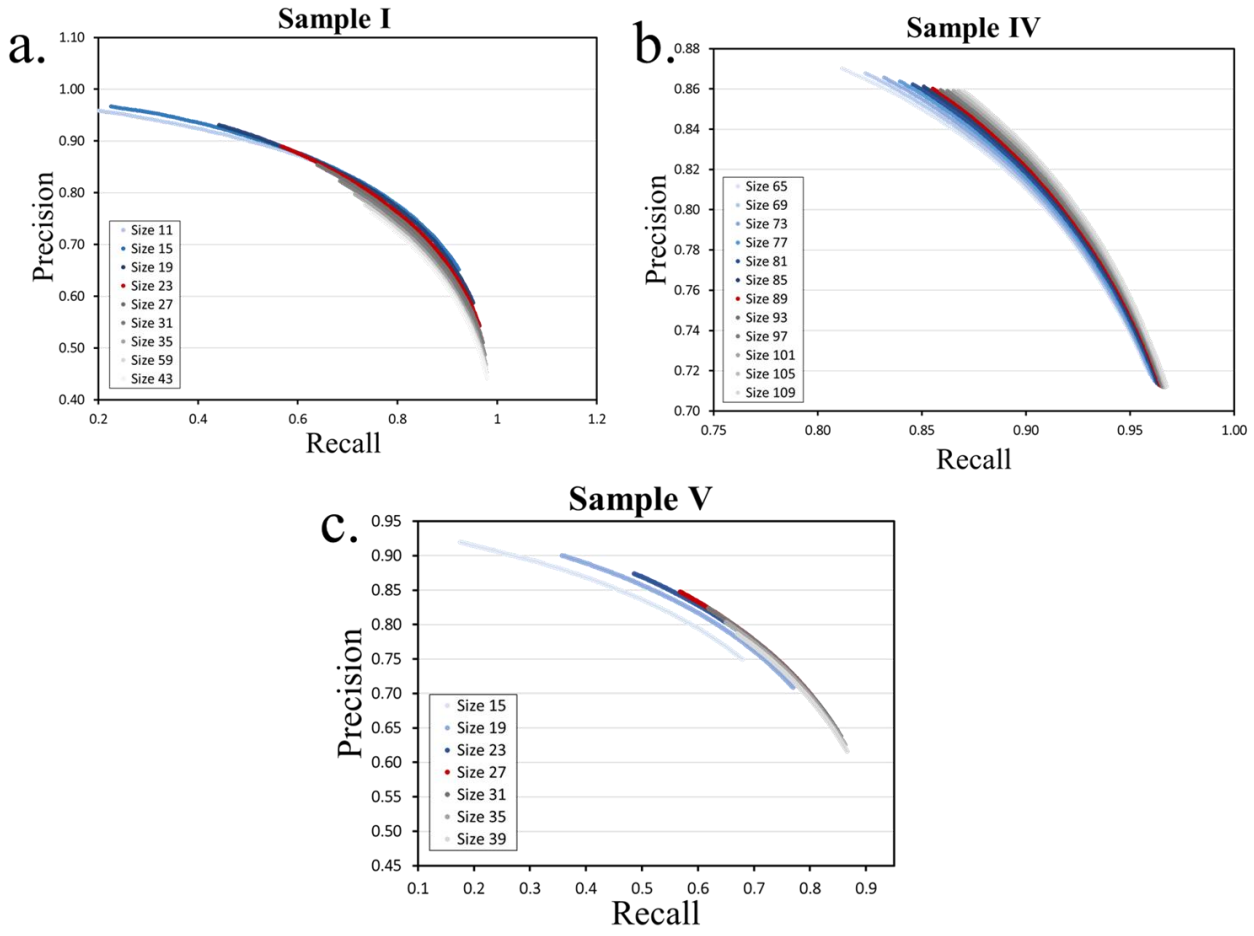

Figure 27. *Precision and recall score trends from the segmentation results of three different microstructure sets: a). Sample I, b). Sample IV and c). Sample V. Each line represents systematic variations of the sensitivity and neighborhood size parameters of the adaptthresh segmentation function in MATLAB.*

Figure 27 contains the precision and recall score evaluations of samples I, IV, and V. These graphs serve as guides from which the adaptthresh parameters that maximize the precision and recall scores are to be selected. In a single plot, each point along a curve

represents a different sensitivity value and lines of different colors captures the effect of varying the neighborhood size value. In figures ***Figure 27 (a)*** and ***(c)*** for example, the neighborhood size is systematically increased, resulting in increments of both precision and recall values, until a maximum is reached and the lines start to go in the opposite direction with decreasing scores values. This is a clear indication that neighborhoods of sizes 23 and 27 are to be used respectively for each set of images. In ***Figure 27 (b)*** a different behavior is observed, where the rate at which the precision and recall scores increase, slows down significantly. Visual validation between the resulting segmented images from neighborhood sizes 89 and 109 led to the conclusion that increasing number of details were being lost as the neighborhood size increased, however over segmentation of larger areas was compensating for the lost pixels and therefore the precision and recall scores were still increasing. For this reason, the neighborhood size of 89 was chosen instead. Along with this validation protocol, visual validation of the segmented images using techniques such as overlay and edge demarcation was always employed on every image to ensure that segmentation was capturing the correct local states.

A summary of the segmentation results is provided in ***Table 7.*** Since all the samples within the same chemistry group were solution treated at the same temperature above the beta-transus, the volume fractions of samples with the same chemistry are expected to be very close to each other [9]. This behavior is confirmed to be the case for the samples in this study and within the standard deviations of their peers. The only exception is sample IV with an average volume fraction of the β-phase of 30.48 ± 0.63. This can be explained by the fact that this was the only alloy sample that was furnace cooled allowing more time for the complete diffusion of the allowing elements and the formation of the respective

phases. Previous studies have reported that for similar microstructures of the same alloy type, the β-phase volume fraction can take values of up to 50% [259-261] which validate the results obtained here.

Table 7. *Summary of microstructure statistics from segmentation on SEM-BSE images captured from randomly selected grains in fully basket-weave samples.*

Fully Basket-Weave Image Segmentation Results			
Sample		**β-phase %**	**α-phase %**
Ti6242	**I**	9.47 ± 0.95 %	90.53 %
	II	8.22 ± 0.73 %	91.78 %
	III	9.35 ± 0.74 %	90.65 %
Ti6246	**IV**	30.48 ± 0.63 %	69.52 %
	V	22.65 ± 0.92 %	77.35 %
	VI	23.21 ± 1.32 %	76.79 %
Ti811	**VII**	9.58 ± 0.91 %	90.42 %
	VIII	9.14 ± 0.85 %	90.86 %
Ti64	**IX**	5.87 ± 0.49 %	94.13 %
	X	5.00 ± 0.29 %	95.00 %

On the other hand, the different cooling rate at which the samples were subjected to, were intended to significantly vary the secondary-α lath microstructures. Low cooling rates such as furnace cooling or air cooling on k-wool, are responsible for coarse and low-aspect-ratio laths, while high cooling rates (e.g., water quenching) results in finer laths with larger aspect ratios [90, 233, 234, 236].

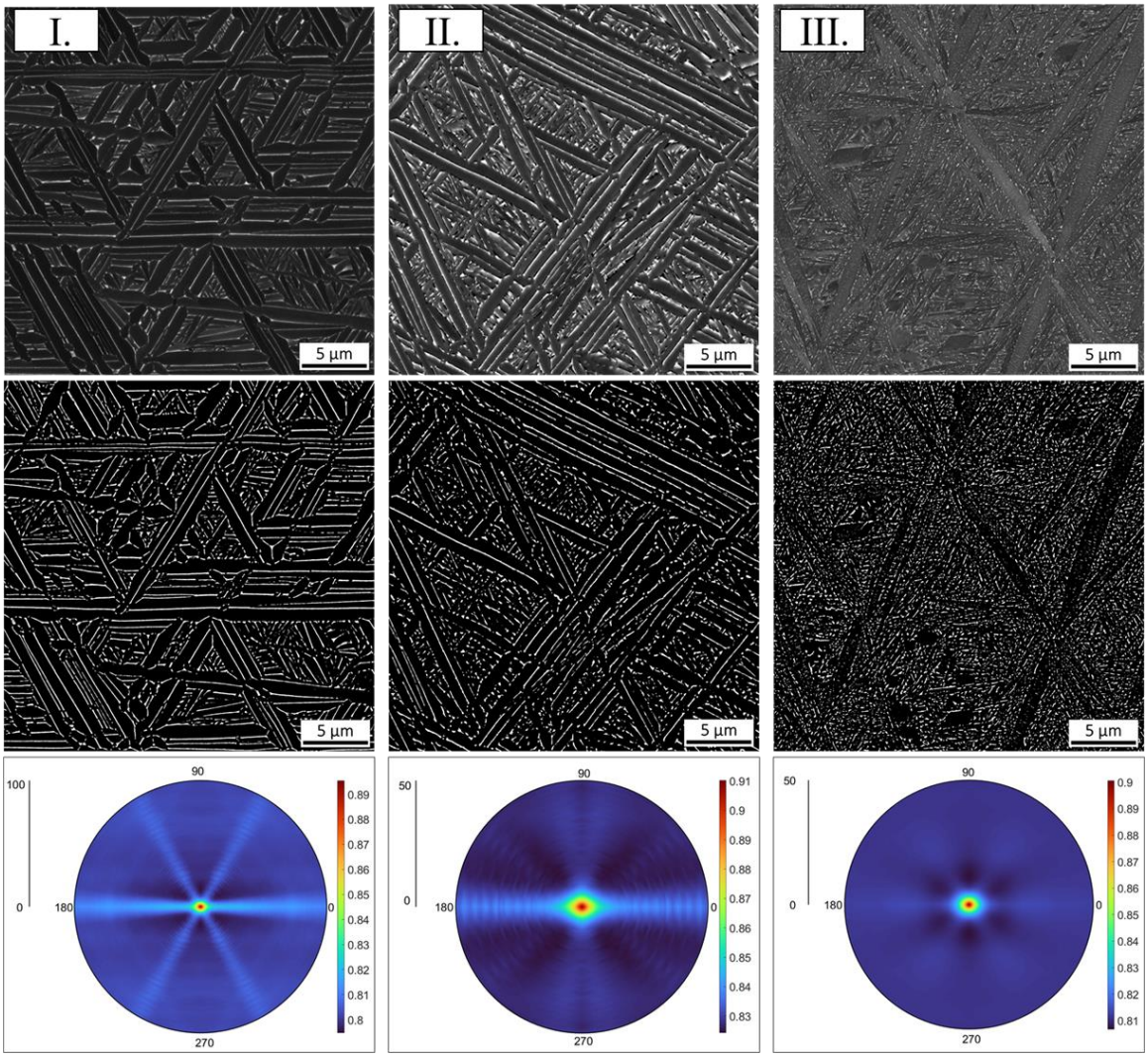

Figure 28. *Representative BSE images of Samples I, II and III, with their corresponding segmented images in the second row and the rotationally invariant 2-point correlations plot of the secondary-α laths (black regions) in the bottom row.*

The first row of ***Figure 28, 29, 30 and 31*** present original representative SEM-BSE images from all the samples used for this task. A total of 20 images was collected for each microstructure from randomly chosen grains. As mentioned before, basket-weave microstructures present repetitive lath morphology patterns that repeat themselves at smaller length scales. This is known as fractal microstructures and can be evidenced at

every one of these images and their respective segmented representation in the middle row of these figures.

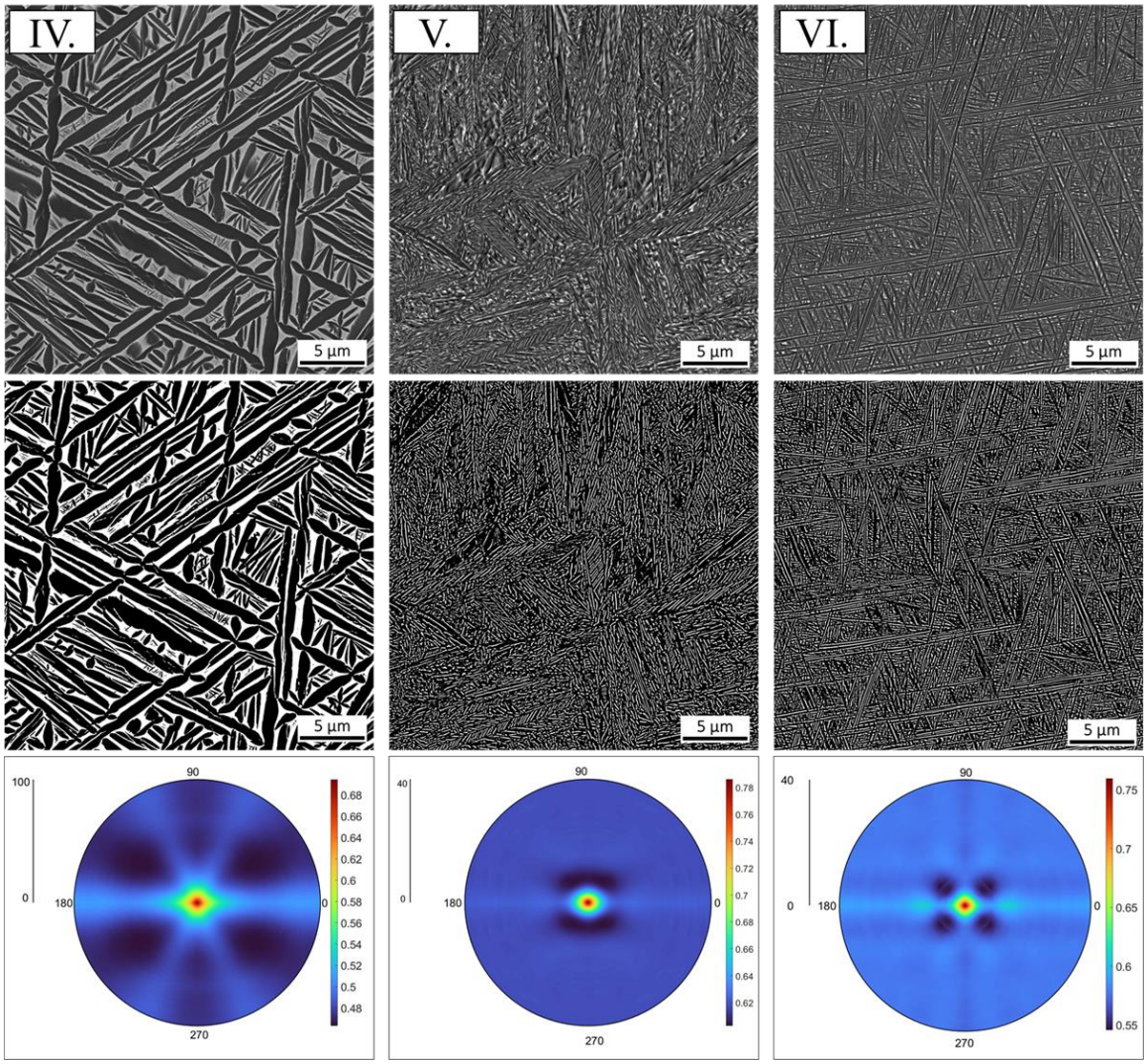

Figure 29. *Representative BSE images of Samples IV, V and VI, with their corresponding segmented images in the second row and the rotationally invariant 2-point correlations plot of the secondary-α laths (black regions) in the bottom row.*

Due to the complexity of these microstructures in terms of length scales, patterns and relative directionality between laths, defining a single descriptor such as lath-thickness to define the microstructure, can be seen as a considerable oversimplifying approach. Instead, rotationally invariant 2-point statistics (RI2PS) is chosen to fully capture the microstructure

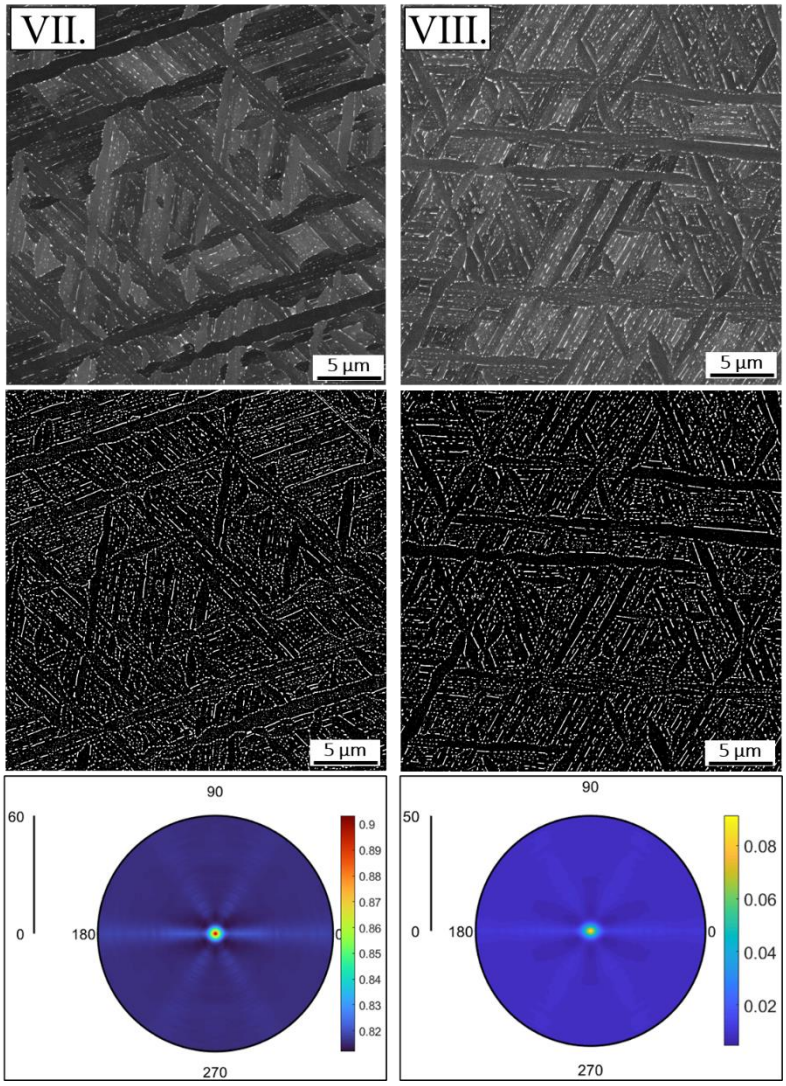

Figure 30. *Representative BSE images of Samples VII and VIII, with their corresponding segmented images in the second row and the rotationally invariant 2-point correlations plot of the secondary-α laths (black regions) in the bottom row.*

statistics and to conserve the relative angular differences between the salient morphological features (e.g., laths), while annulling the dependance on the observer reference frame. All images were collected with the same view-fields and pixel sizes to facilitate the segmentation process and the interpretation of the RI2PS of the secondary-α phase, for which their visualizations are presented in the bottom row of the same figures. In 2-point

statistics, long vectors don't represent significant information due to the correlations degenerating to the square of the area fraction as the vector size increases. For this reason, the statistics need to pre-truncated prior to carrying out Principal Component Analysis.

Although the same truncation level is necessary to obtain a fair comparison in PCA,

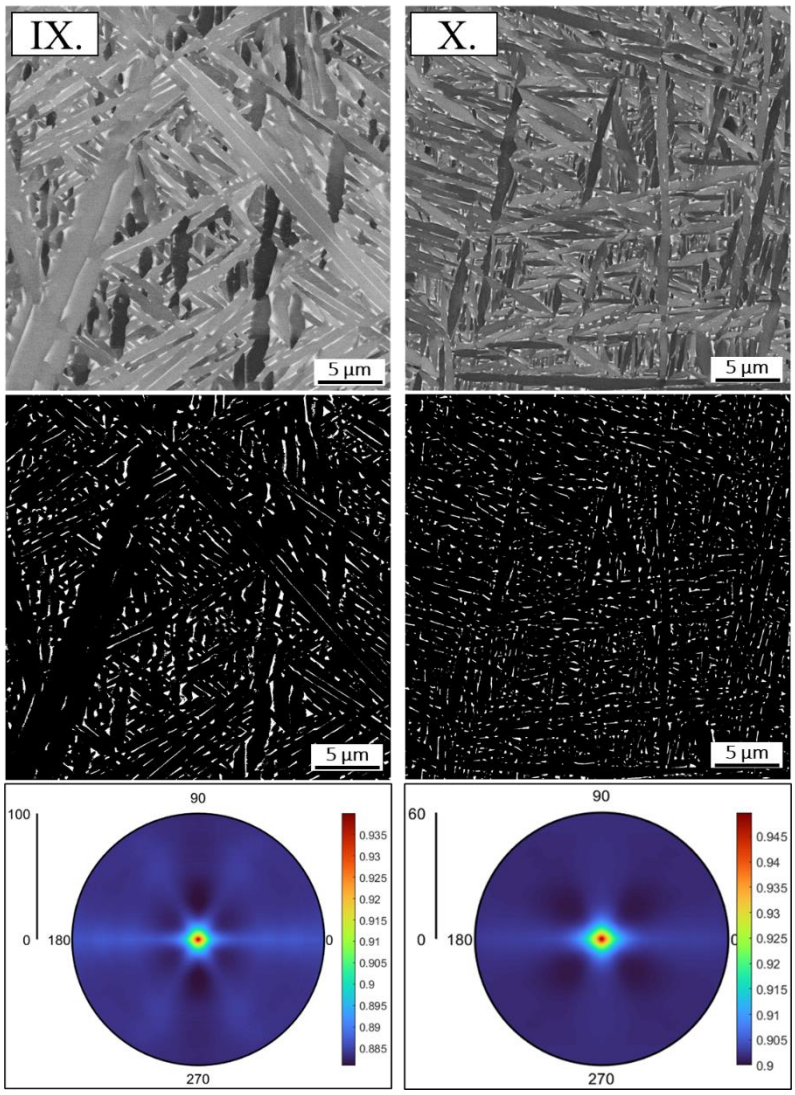

Figure 31. *Representative BSE images of Samples IX and X, with their corresponding segmented images in the second row and the rotationally invariant 2-point correlations plot of the secondary-α laths (black regions) in the bottom row.*

the RI2PS plots presented here have been truncated to different vector lengths to better

visualize the details captured by these correlations. The crisscross or triangular pattern is perhaps the more accepted and popularly known morphology of the basket-weave microstructures. However, an additional morphology has been previously reported in literature to have a more quadrilateral structure [233, 236, 253]. This type of morphology can be well appreciated in ***Figure 31*** for sample X, where the RI2PS plot shows four clear peaks instead of six like in the other visualizations. The effect of this arrangement on the mechanical properties of materials, compared to those from triangular patters, has not been studied up to date to the best of the knowledge of the present author, and is not in the scope of the present work.

The mechanical properties, and therefore the application of titanium based α/β alloys have been observed to principally depend on the characteristics of their microstructures [168, 222]. Particularly to basket-weave morphologies, while there has been a great effort to relate the processing parameters to the resulting microstructure [12, 228, 262], less effort has been targeted towards studying the relationship between microstructural features and the mechanical properties of these alloys. Although some authors have attempted this task [90, 229, 234] there hasn't been yet a physically based model developed to date to relate these characteristics. This is due mostly to the tremendous level of complexity in this type of morphologies involving a range of length scales, in addition to their interdependence between many of the microstructural features, making it impossible to isolate the effect of a single parameter. For example, Kar et al. [234] determined that while values for the yield strength as a function of lath thickness can be plotted, the values colony size factor, prior

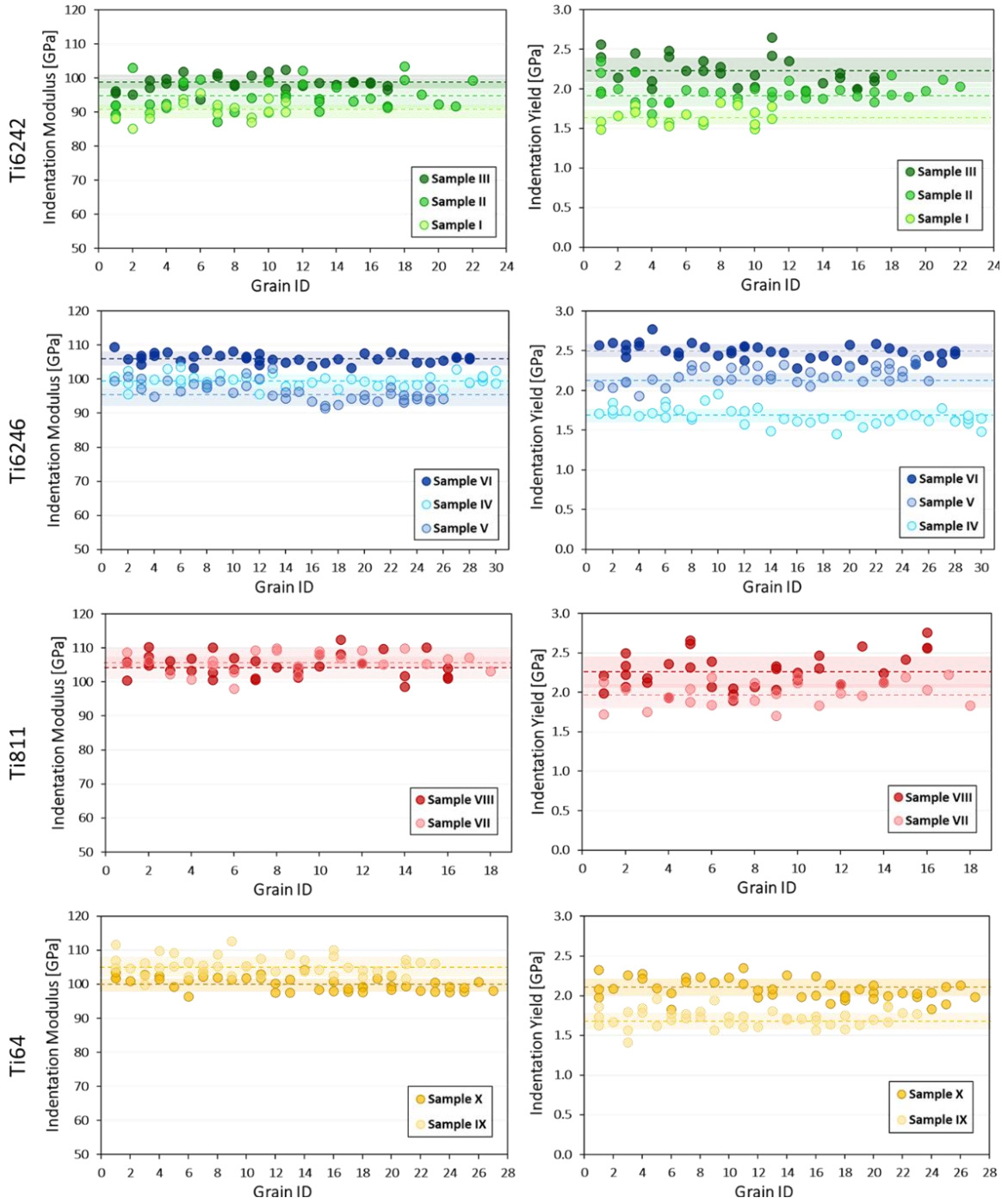

Figure 32. *Experimentally measured grain-scale indentation modulus and indentation yield values from all the fully basket-weave specimens in this study. Means and standard deviations are also plotted for reference.*

β-grain factor, and volume fraction of total α are also simultaneously changing due to their interdependent response to the heat treatment.

The results presented in ***Figure 32*** correspond to the indentation modulus and indentation yield strength values from spherical indentation experiments conducted within individual grains in the samples. By doing this kind of experiments, microstructural features such as grain size, tortuosity of the grain boundary and width of grain-boundary-α are removed from the analysis, decreasing the number of variables in the structure-property relationship, in addition to the already constant volume fraction of α- and β-phases as discussed above. These experimental results are in accordance with previous conclusions by the scientific community [90, 167, 233-236] where coarser laths such as the ones observed in samples I and IV are normally predicted to exhibit lower strengths compared to the higher yield strengths from microstructures with finer laths such as the ones from samples III and VI .

We refer the reader once again to ***Table 6*** where the mean values and standard deviations corresponding to the measurements illustrated in ***Figure 32***. The effect of lath thickness is better captured by the indentation yield strength plots along with ***Figure 22*** containing all the microstructural images. The standard deviation values for all the samples is fairly constant, evidencing that in all cases, a representative volume of material, containing the response form a significant number of laths, was tested. Indentation modulus mean values on the other hand, seem to be a lot closer to each other, evidencing less sensitivity to the lath microstructure. For both mechanical properties, the variation captured by the standard deviation is significantly smaller compared to the results from task I,

manifesting a much lower sensitivity to the crystallographic orientation differences between the grains tested.

PCA was then performed on the ensemble containing the autocorrelations (on the alpha phase) for a total of 207 images. The variance percentage captured by each of the principal components in this evaluations is plotted in ***Figure 33***. It is observed that PC1 and PC2 combined, capture the 99.94 % of all the variance contained in the microstructure statistics. ***Figure 34*** presents the PC representations of the statistics from each microstructure set, with PC1-PC2 and PC1-PC3 principal components in the axis.

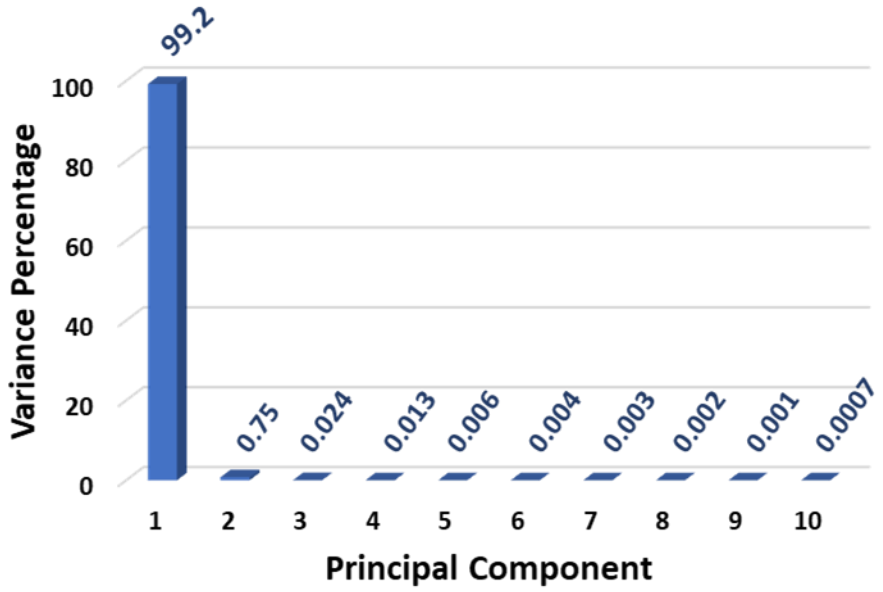

Figure 33. *Variances captured by each of the 10 firsts PC components from the principal component analysis on the basket-weave microstructural information.*

Keeping in mind that other than the microstructures statistics themselves, no other information was previously fed to the PC analysis, this evaluations is observed to be successful at classifying the unique microstructures in an unsupervised way. PC1 can be

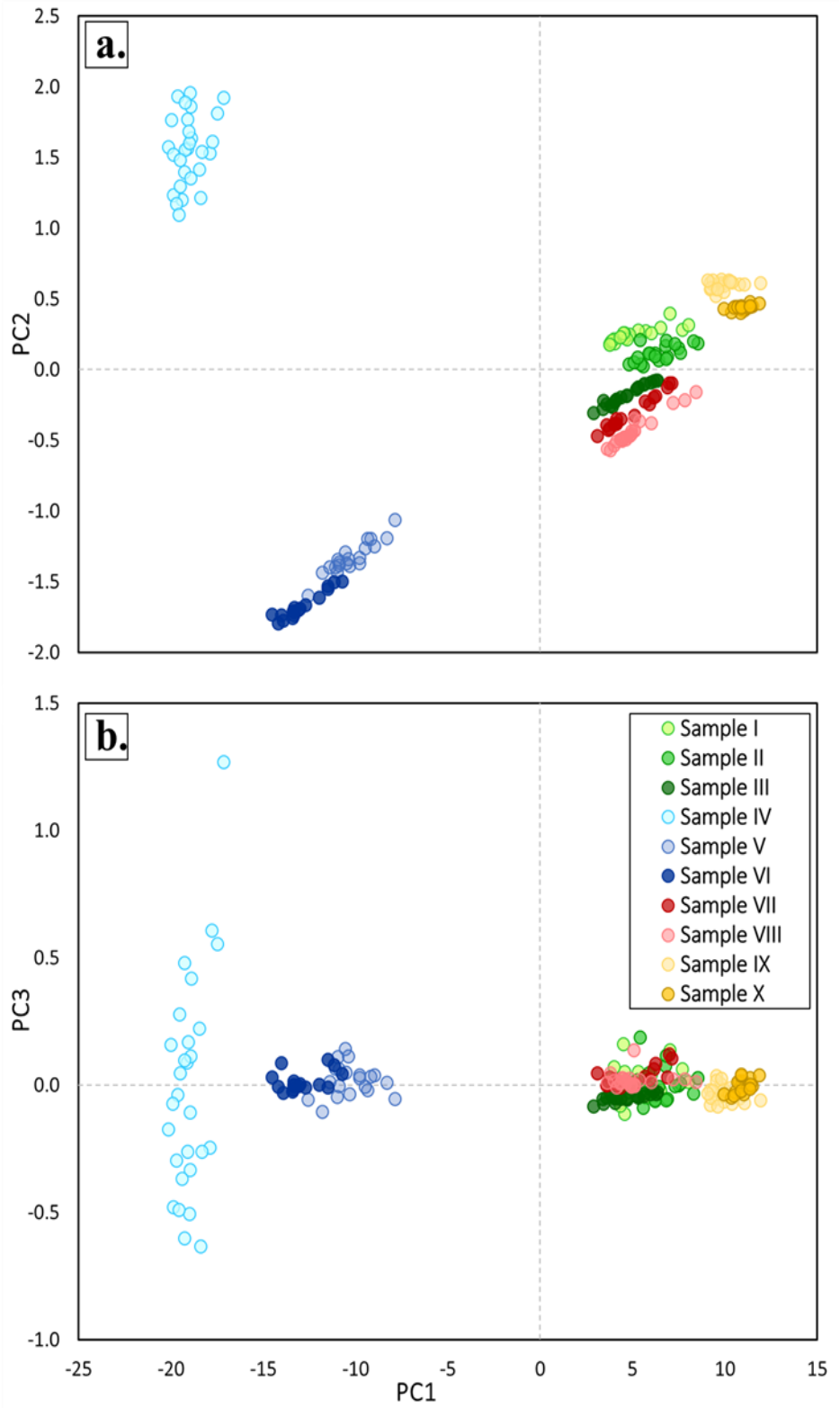

Figure 34. *Low-dimensional representation of all the basket-weave microstructural images obtained from PCA. Data points of the same color represent the same chemistry where darker share of the color is associated with higher indentation yield. In a). PC1 and PC2 components, and in b). PC1 and PC3 components. Here, PC1 is associated with the volume fraction classification in the alloys and PC2 is representative of the secondary-α lath thickness.*

well interpreted to correlate with changes in the volume fractions (and therefore the alloy type) where increasing values of the PC1 coordinates are representative of increasing volume fractions of the secondary-α phase. In this figure, different alloys types are represented by the same color, and different shades of the same color indicate distinct samples of the same chemistry. Additionally, PC2 is observed to capture the lath morphology differences between samples. Here, higher values of the PC2 coordinates indicate the presence of coarser α-laths which can be simultaneously associated with decreasing indentation yield strength values represented by lighter shades of the same color (e.g. Samples I, IV, VII and IX).

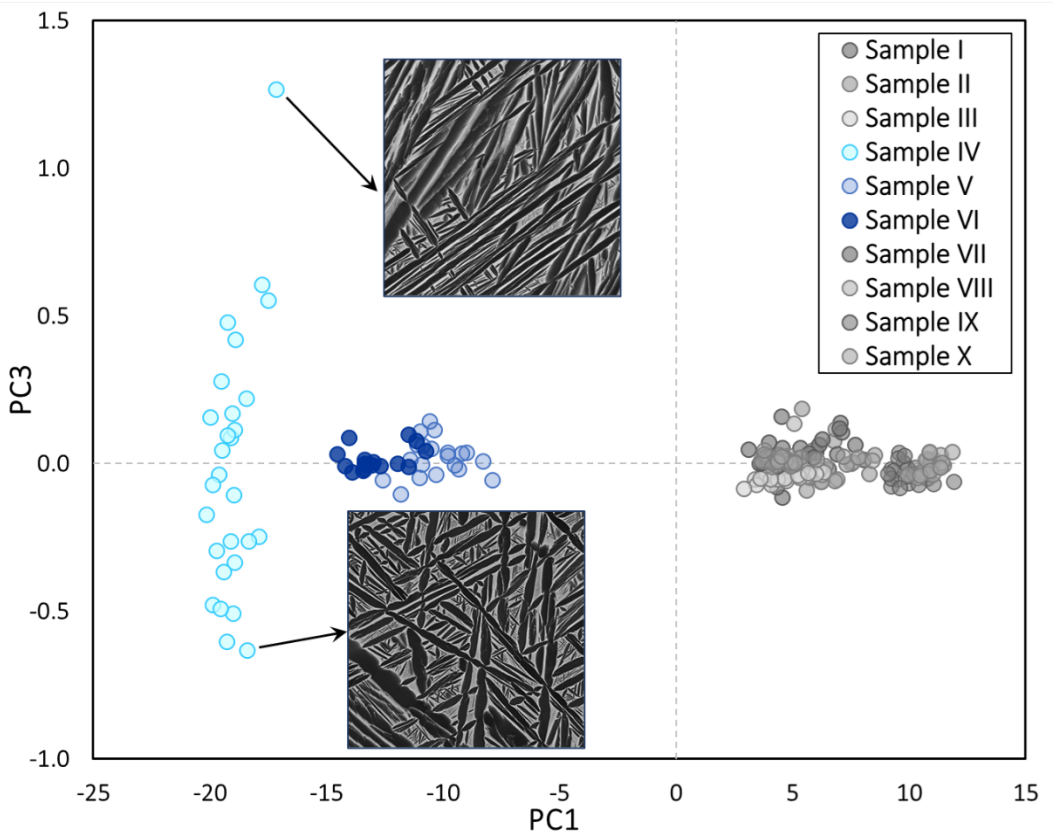

Figure 35. *Plot depicting the microstructural variations captured by PC3 where the microstructure on top presents more parallel distributions between laths, and the image at the bottom the more characteristic crisscross pattern of the basket-weave morphology.*

From ***Figure 34(b),*** PC3 doesn't seem to capture too much information agreeing with the very small 0.024 % of the data variance contained by this principal component. However, when looking carefully at the data points locate at the extremes of this axis in ***Figure 35***, we can recognize that the arrangements/directionality between laths is being also classified and compared among the other images within the same alloy kind. This is of tremendous importance as we are now being able to fully define and autonomously classify every microstructure in very simplified plots, while capturing microstructural features such as volume fractions, lath morphologies and lath directionalities.

Ideally, in order to thoroughly train a model that could potentially predict the properties of a specimen based on the microstructure information, a lot more microstructures and chemistries would need to be added to this analysis, to have enough training and predicted data points. In the case of chemical information, dimensionality reductions of the alloying elements such as the aluminum and molybdenum equivalences (i.e., Al_eq, Mo_eq) could be potentially used, as their values have been observed to correlate with strength values [243].

CHAPTER 5 Multiresolution Spherical Indentation on a Bimodal Titanium Alloy

5.1 Introduction

Bimodal alloy refers to the class of materials that simultaneously present two crystallographic states or phases in their microstructure. In many cases, these phases can be arranged in more than one distinct morphology. Examples of these classes included two-phase steels, alpha-beta brasses, and alpha-beta titanium alloys. These type of microstructures offer great technological advantages as they offer balanced combinations of properties that can be tuned through heat-treatment processes that control the morphologies and their volume fractions. For instance, in α-β titanium alloys, a bimodal microstructure consisting of approximately 30 vol.% of equiaxed primary-α grains and 70 vol.% of lamellar α-β morphology, has been recognized to provide an optimal combination of creep and fatigue properties for compressor disks operating at high temperatures [2].

Great effort has been put into predicting the effective properties of this type of microstructures based on the individual behavior of the constituents. However, the complex interaction and deformation behavior between phases has been recognized to be present a challenge in this understanding since neither the strains, nor the stresses are unform in a given two-phase (or multi-phase) material [263-266]. Additionally, factors such as grain/particle sizes, morphologies of the phases, texture and crystallographic relationships, stress-strain behavior of the components and inhomogeneous stress/strain distributions, must be incorporated in any rationalization of the two-ductile phase deformation, making of this a rather difficult task.

The “Law of Mixtures” or “Rule of Mixtures” has been put to test by several researchers on a wide variety of materials leading to the conclusion that this rule cannot always be applied, or that it can only be applied for some tensile properties [267-269]. For example, the law of mixtures was shown successful at predicting the 0.2% yield strength of ferrite-martensite steels [270-272], but less fortunate results were obtained for the tensile properties of titanium [264, 266, 273, 274] and zircalloy-4-oxygen alloys [275]. The greatest failure of this rule is the assumption of constant stress or strain. In the present work, this law is merely used as a point of reference and not a rule.

In this task, the spherical nano-indentation protocols are applied at two distinct length-scales over a bimodal titanium microstructure composed by globular-α and basket-weave grains. Grain-scale and effective indentation yield strengths are estimated experimentally, and microstructure characterization is conducted using image segmentation and high-order statistics. This information is later utilized to evaluate the performance of the Rule of Mixtures (ROM) and compare it to the measured effective property. The ability to measure the grain-scale strength of the constituents, presents a great advantage into the future of modeling and predicting the effective performance of materials. This assessment aims to provide an insight into methodologies that can substantially reduce the cost, time and effort currently necessary for the evaluation of new materials and heterogeneous materials systems.

5.2 Methods and Materials

5.2.1 Materials and Sample Preparation

For this task, it was ideal to select a material that was used in common for tasks I and II, to use the previously obtained information as validation data of the here obtained mechanical and microstructural results. The material chosen for this study was Ti-6Al-2Sn-4Zr-2Mo due to its heat treatment versatility to produce desired microstructures. The actual composition of the alloy was determined to be Ti–5.93Al–2.01Sn–4.05Zr–1.88Mo–0.12Si in weight percent, while the interstitial contents of oxygen, carbon, iron, and nitrogen were 0.107, 0.023, 0.05, and 0.001, respectively as reported by this study using the same exact material [276]. Specimens of dimensions $10.0\,\text{mm} \times 20.0\,\text{mm} \times 2.0\,\text{mm}$ were EDM cut and placed into quartz tubes which were subsequently backfilled with Argon to protect the samples from oxidating during the heat treatment process. The main objective to be accomplished with heat treatment was to obtain a microstructure with grains from both morphologies large enough to allow spherical indentation with the same indenter tip while capturing the mechanical response from a representative number of laths in the basket-weave grains. Although several heat treatments were designed, only one of them produced a microstructure that could satisfy the previously mentioned goals. The specimen was heat-treated at 986°C (10°C below the beta transus for a bimodal microstructure) for 6 hours, followed by a water-quenching step to achieve the basket-weave morphology. Subsequently, the sample was subjected to a stress-relieve process at 700°C for 4 hours and finalized with air-cooling. Heat treatment was conducted in a Thermo Fisher Scientific, Lindberg/Blue 1100 °C Box furnace.

Although the sample preparation typically used for spherical indentation employs very standard microscopy procedures, this step became of significant importance in this step. Since a much smaller indenter tip was used on basket-weave grains, where the topology differences between the phases are more notable at this length scale, it was essential to minimize the height inequalities caused by the mechanical and chemical polishing procedures. Some of these modifications involved the force reduction during the mechanical steps, a decrease in the hydrogen peroxide amount (from 1 to 0.5 parts in the vibro-polishing step and polishing times were increased instead. These chemo-mechanical processes were performed using the Struers' Tegramin Automatic Grinding Machine and the Buehler's Vibremet 2 Vibratory polisher, with carbide papers starting from 800 grit down to 2400 grid.

5.2.2 Mechanical Characterization

Mechanical characterization was conducted at room temperature on a Nano-Indenter G200 by Keysight. Two different tip sizes were used for this task: a 15.2 μm radius tip was employed for the grain scale characterization of primary-α and basket-weave grains, whereas a 500 μm tip was used to measure bulk mechanical properties. In the first scenario, the top indentation depth was kept constant at 500 nm, and for experiments with the larger tip, the equipment reached its maximum force limit at 10 N. For indentations on the primary-α grains, the average contact radius at yield was calculated to be 556.2 nm. It is essential to mention that this is only a mean value as stronger orientations of the alpha grain will evidence smaller contact areas at yield, and softer grains will result in larger contact radius values. For basket-weave grains, the average contact radius at yield was estimated

to be 642 nm, which captured the contribution from multiple secondary-α laths within the grain. In the case of bulk measurements on the sample, the average contact radius at yield was determined to be 23.259 μm (i.e., 23259 nm), meaning that the behavior of a representative number of grains from both morphologies was acquired.

For this task, in order to keep the protocol constant for all the measurements, the indentation yield strength was determined by the intersection of the indentation stress-strain curve with a straight line parallel to the elastic segment and with a 0.2% indentation-strain offset. This approach was used since the indentation stress-strain curves from the different morphologies and length scales presented slightly different shapes that didn't allow the standardization of a back extrapolation segment. Additionally, although the sample preparation was carefully monitored to decrease surface roughness, difference between the rate at which each titanium phase gets polished, unavoidably results in surface topography. To correct for this issue, the load-displacement segment corresponding to the elastic deformation is chosen from higher segments along the curve to eliminate data points that contain erroneous information from the surface of the material. Indentation stress-strain curved from the three sets of analysis are provided in ***Figure 36*** depicting the large range of indentation properties by the primary-α grains.

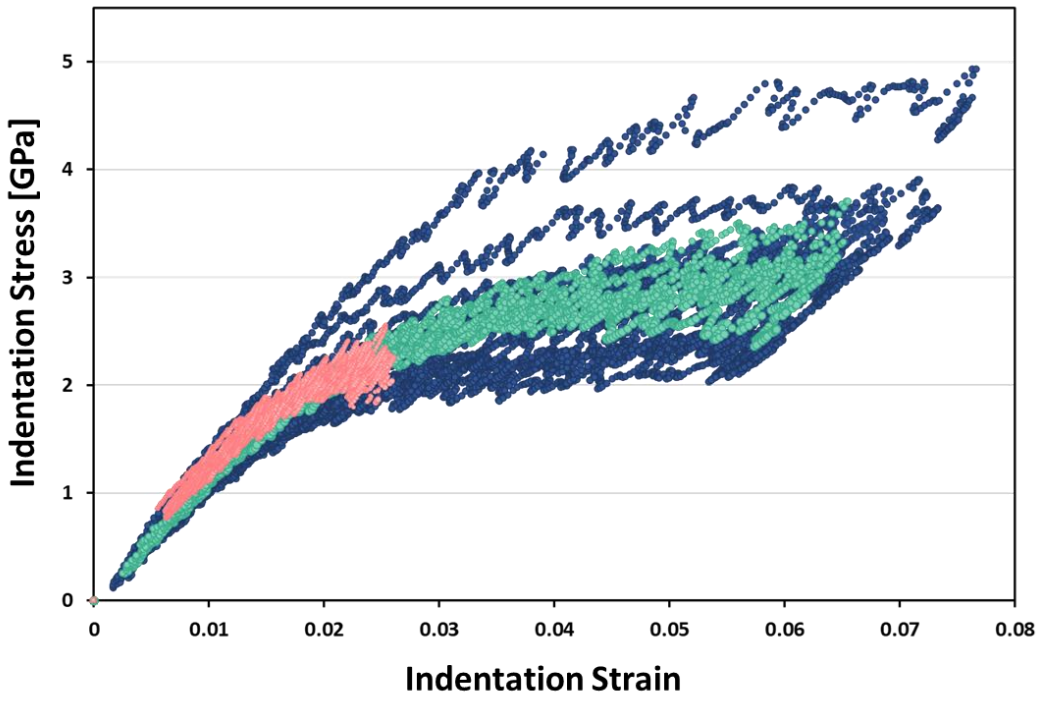

Figure 36. *Examples of the indentation stress-strain curves from the experiments on primary-α grains in blue, on basket-weave grains in green, and bulk measurements in pink.*

5.2.3 Microstructure Characterization

BSE and EBSD techniques were used for the microstructure characterization of this bimodal sample. The basket-weave morphology was captured by imaging 20 unique and randomly selected grains and keeping a constant view-field of 10 µm. Images of 100 µm view-field were acquired for the bulk microstructure characterization. An accelerating voltage of 15 kV was used for the collection of BSE images, while EBSD characterization used an accelerating voltage of 20 kV. In all cases, the resolution of the images was kept constant at $2048\ x\ 2048$ pixels.

BSE images were later analyzed through a series of image processing steps with the objective of labeling each relevant feature of interest and to obtain important statistical

information. [90-93]. This process is referred to as Image Segmentation and is more specifically defined as the process of designating each pixel in 2D microstructures (or voxel in 3D microstructures) as element of a feature of interest or local state. The sequence of steps used during the segmentation process substantially influences the resulting quantification of microstructure, and therefore the understanding of the deformation behavior itself.

For this specific microstructure, two different segmentation sequences were conducted. The first one, on the 100 μm length scale images, with the purpose of determining the volume fraction of primary-α and basket-weave grains. This part started with global noise correction with the imgaussfilt function of the image processing toolbox of MATLAB and a sensitivity value of 0.9. Next, a constant threshold value of 85 was used for the `imquantize` function. As a consequence of this step, many small areas within the basket-weave grains we also segmented, and in order to remove them, the function `bwareaopen` is used in the segmented image.

The second segmentation sequence, applied on the images from the basket-weave grains with view field of 10 μm, also started with the global correction step, but was then followed by a varying thresholding step in which the threshold level is evaluated based on the sensitivity and neighborhood size parameters which are inputs form the user (`adaptthresh` and `imbinarize` functions). Once again, the `bwareaopen` function is employed to remove small segmented areas or single pixels.

Once the basket-weave images were segmented, the rotationally invariant 2-point statistics of these microstructures are estimated. The 2-point statistics analysis denotes the probability of finding local states *h* and *h'* which are separated by a vector of length *r* [99].

In equation 1, $|S_r|$ represents the normalization factor which represents the number of trials that were computed for each unique vector r (therefor the probability). In order to make this analysis computationally efficient, discrete Fourier transforms are (DFTs) are used [64, 94, 245]. The rotationally invariant adaptation of these statistics removes the sensitivity to the observer's reference frame, while maintaining the directionality microstructure statistics inherent to the basket-weave morphology. Basically, the 2-point statistics in Cartesian coordinates are converted to their polar representation, and then the whole frame is rotated by an angle ψ so that the dominant information of the microstructure is aligned to the horizontal axis of the new plot. This rotation is completed while maintaining the relative orientation differences within the statistics (θ) (for a more detailed explanation of this statistical analysis step, please reflect to section 2.2.3 of this document).

For the orientation characterization of the primary-α phase, 20 EBSD scans were collected of adjacent and slightly over-imposing areas with dimensions 150 µm x 150 µm. An imaging step of 0.5 µm was used for all scans. Using the TSL OIM Analysis 8 software, the images were carefully arranged next to recreate a single scan of approximately 680 µm x 545 µm shown in ***Figure 37(a)***. Since the objective was to determine the orientation texture of the alpha phase, the image quality parameter was used to filter out the pixels that mostly likely belonged to the basket-weave grains. Only scan data points with image quality higher than 45000 were used to construct ***Figure 37(b)***, where the original average image quality of the scan was 68519. The inverse pole triangle depicting the overall harmonic texture can be appreciated in the bottom-right corner of this figure from which the predominant presence of the $[0001]$ and $[10\bar{1}0]$ primary-α orientations can be observed.

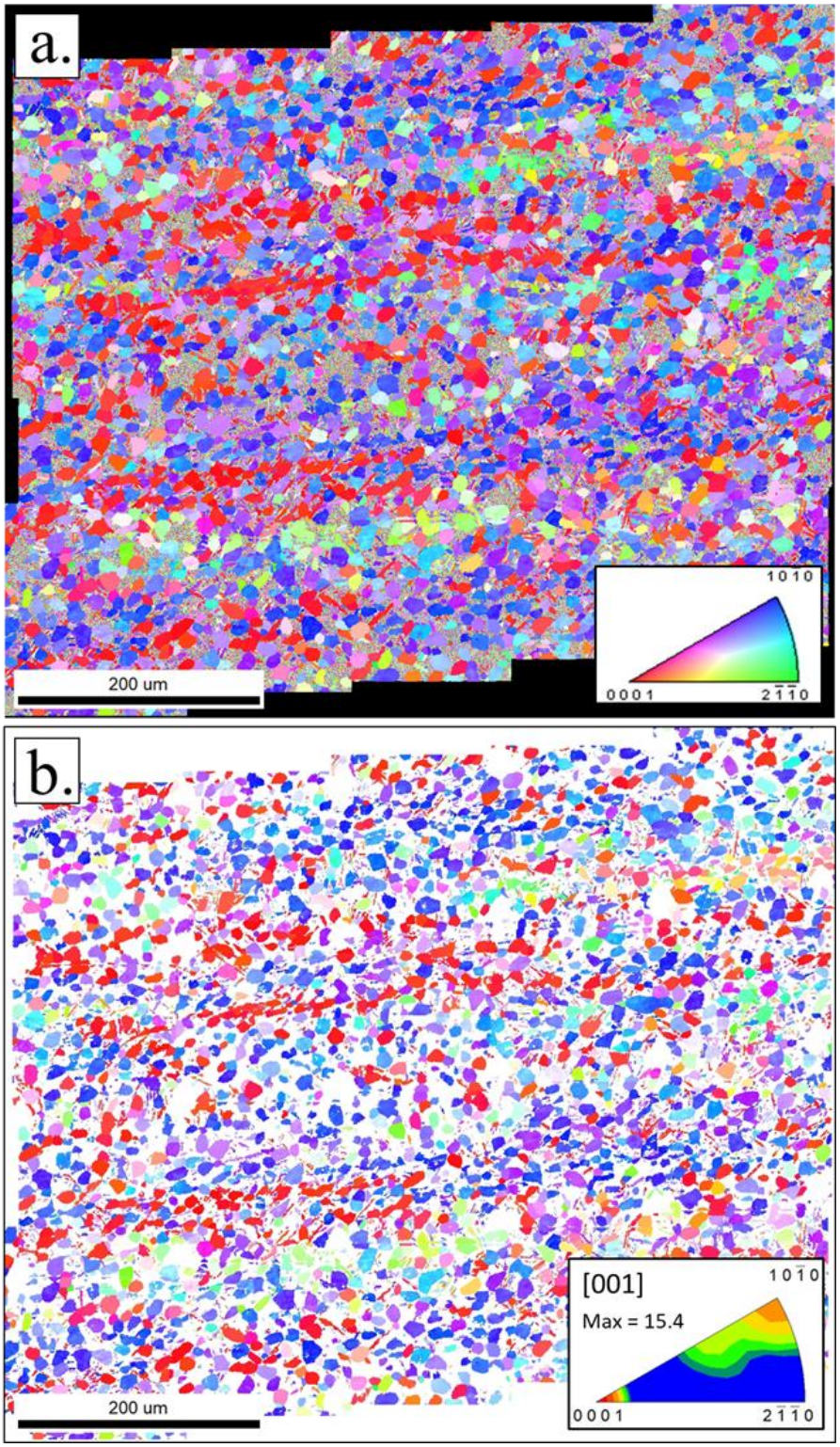

Figure 37*. a). Compilation of 20 EBSD scans from a Ti6242 bimodal microstructure with primary-α and basket-weave grains. Areas with low image quality correspond to basket-weave grains. b). Inverse Pole Figure map of the primary-α grains only with a harmonic texture IPF triangle at the bottom-right corner.*

Despite the fact that horizontal bands of the [0001] and [10$\bar{1}$0] primary-α orientations are observed to remain from the original manufacturing process of the metal sheet, effective values of the indentation modulus and yield strength were expected to be collected based on the predicted contact area at yield and by performing numerous indentation experiments in randomly selected locations to later perform an average operation of the results.

In order to obtain a volume average property of the primary-α phase, the hcp declination angle range was divided into smaller regions of width 10°, for a total of 9 segments. The partition fractions for each of these segments are summarized in ***Figure 38*** and are representative of the volume fractions of the grains belonging to each orientation sub-range. These values were therefore used to determine the overall volume fractions of the α-phase grains that belong to these orientation regions.

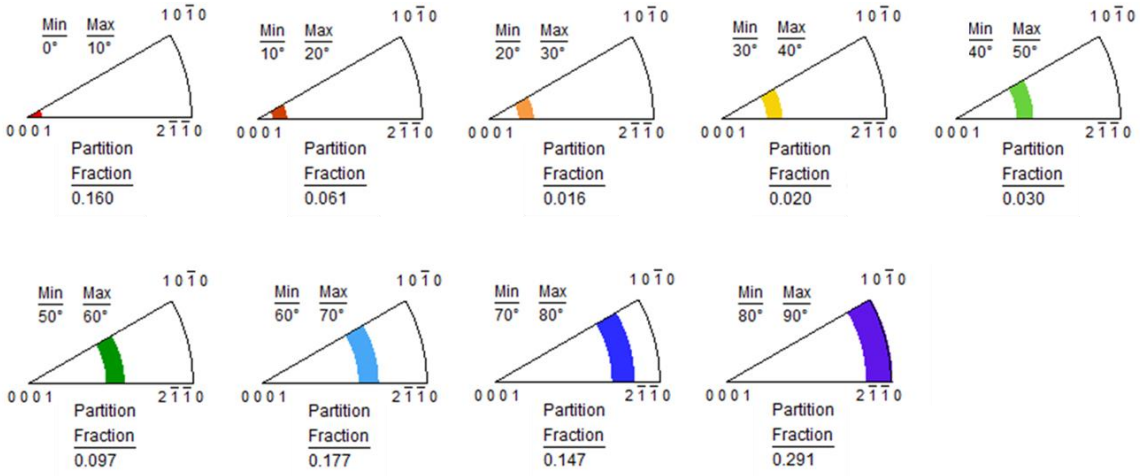

Figure 38. *Partition regions corresponding to increments of 10° in declination angle for the primary-α distributions, and their corresponding partition fractions.*

5.2.4 Composite Theories

5.2.4.1 Rule of Mixtures

The traditional rule of mixtures (ROM) is based on the model proposed by Voigt [277] which estimates the elastic properties of a multi-phase material having as inputs the properties of the constituents and their respective volume fractions, and can be mathematically expressed by:

$$P_{eff} = f_{\alpha}P_{\alpha} + f_{BW}P_{BW} \qquad 17)$$

where P_{eff} denotes the effective property of the system (could be any strass-strain property such as yield strength or strain hardening), f is the volume fraction of a constituent and P is the property (indentation yield strength in this case) where the subscripts α and BW correspond to the α- and basket-weave morphologies. respectively.

The evident simplicity of this linear model is widely attractive in the attempt of estimating the strength of materials. However, multiple modifications of this model have been suggested in an effort to account for the un-realistic isostrain assumption of this relationship [278-280]. Other authors have opted for the application of corrections to the constituent properties that can capture the effect of grain size and texture [281].

5.3 Results and Discussion

The segmentation protocols on the basket-weave microstructural images lead to the results presented in ***Figure 39***. An average volume fraction of the remaining prior-β phase

was found to be 10.11 ± 1.65% (i.e., 89.89% of the secondary-α phase). ***Figure 39(c)*** corresponds to the RI2PS representation of the secondary-α phase (black phase) of the microstructure in the same plot. Once again, the highest intensity peak in these statistics is aligned with the horizontal axis to remove the viewer's frame directionality, and the relative directionality between laths is evidenced. To better interpret the RI2PS plots, we can understand that the probability of finding vectors with head and tail in the secondary-α phase of length approximately 25 pixels and in the $\psi = 30°$ is very low. Further, vectors of all lengths are likely to be found at $\psi = 0°, 60°$ and $120°$. This also plot also served as visual confirmation of the triangular pattern between the alpha laths.

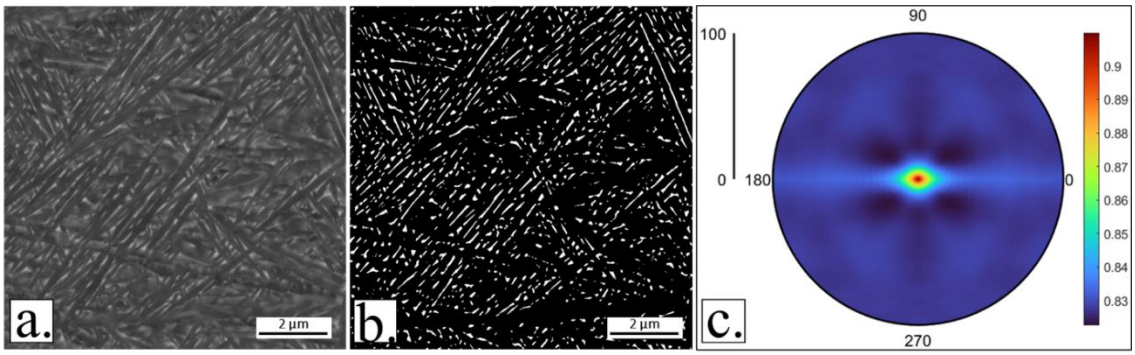

Figure 39. *a). Representative BSE image of the basket-weave grains in the bimodal sample with view-field of 10 µm, b). the corresponding segmented image and c). the rotationally invariant 2-point correlations plot of the secondary-α laths (black regions).*

Segmentation of the bulk material results in the primary-α phase representing the 42.3 ± 4.1% of the microstructure, and a remaining 57.7% of the basket-weave morphology grains. ***Figure 40(a)*** presents the original BSE image of this Ti6242 bimodal

microstructure, two images that serve in the visual validation process of the protocol in ***Figure 40(b)*** and ***(c)***, and the final binary microstructure in ***(d).***

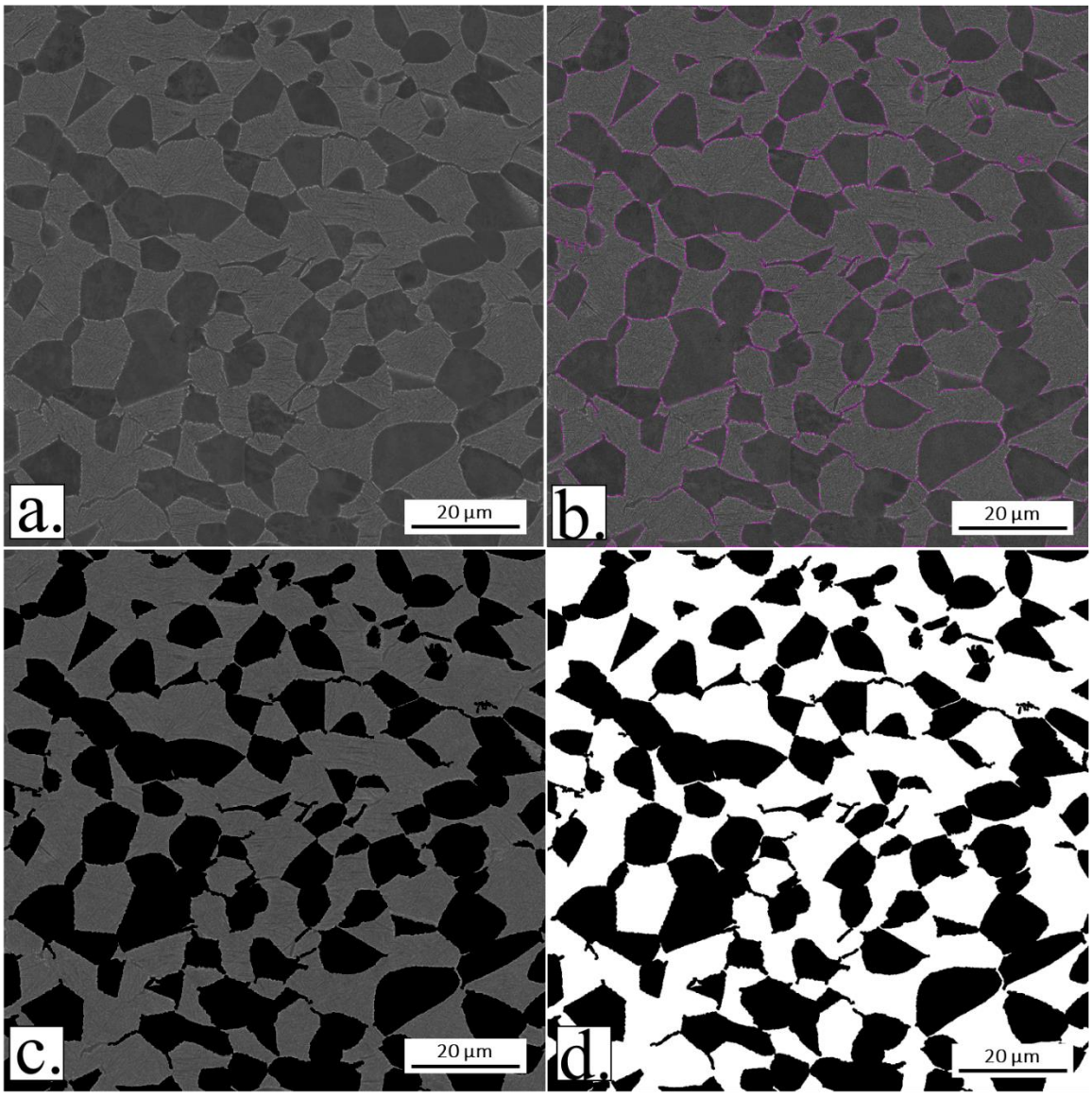

Figure 40*. a). Original BSE image of the bimodal microstructure with view-field 100 µm, b). edge of the segmented regions highlighted in magenta color, c). overlay of the basket-weave regions on a black background and d). the final segmented image in which basket -weave and primary-α morphologies are colored by white and black regions respectively.*

The primary-α partitions summarized in ***Table 8*** evidence the predominant $[10\bar{1}0]$ orientation. These results also explain the large number of experimental data points close to the 0° and 90° ranges of declination angles, and the few data points in the center of this orientation spectrum.

Table 8.*Volume fractions corresponding to the priamry-α partitions.*

Primary-α Orientation Distribution	
Φ Segment	**Partition fraction**
Φ = 0° - 10°	16 %
Φ = 10° - 20°	6.1 %
Φ = 20° - 30°	1.6 %
Φ = 30° - 40°	2 %
Φ = 40° - 50°	3 %
Φ = 50° - 60°	9.7 %
Φ = 60° - 70°	17.7 %
Φ = 70° - 80°	14.7 %
Φ = 80° - 90°	29.2 %

These results, along with the bulk segmentation statistics and the experimental results from ***Figure 41*** were used to define a new set of local states. The basket weave morphology is associated with a single mean value of indentation modulus and indentation yield, whereas the primary-α phase, spanning over a wide range properties, is divided into the previously described partitions, each of them with their own set of indentation properties. By defining these local states, we are able to re-formulate a rule of mixtures expression that accounts for the orientation dependence of the α-phase. The indentation properties for each of the primary-α partitions are obtained after fitting the experimental data to a

regression analysis that accounts for the symmetries in the hcp crystal (same protocol used for the construction of the trend line sin Task I of this work).

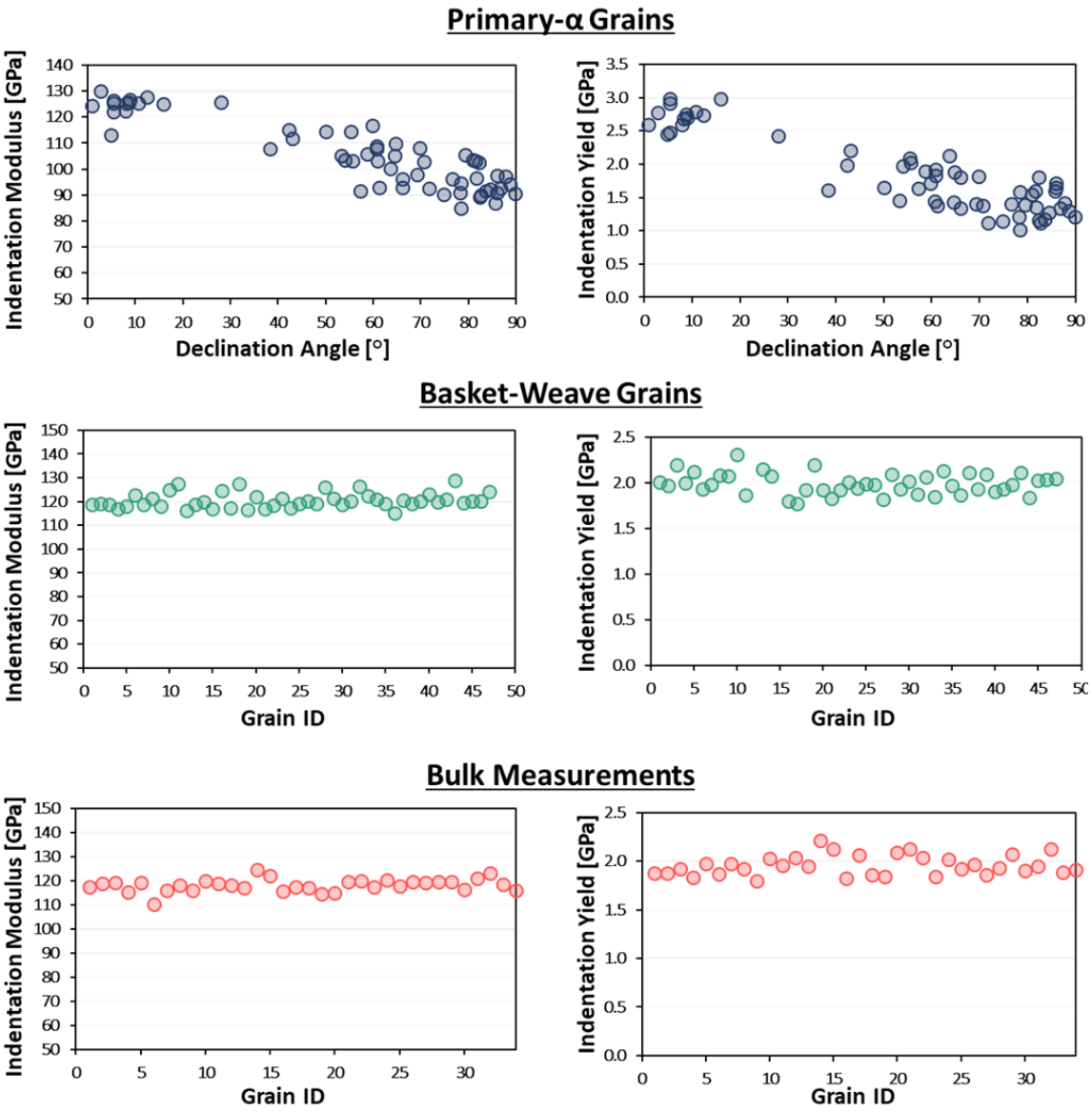

Figure 41. *Results from the spherical indentation experiments performed on the primary- α and basket-weave grains of this Ti6242 bimodal specimen, along with the experiments measuring the effective mechanical properties of the same material. Results from the primary-α evaluation are plotted as a function of the declination angle (Φ).*

From ***Figure 41***, the mean indentation yield for the basket-weave grains was found to be 1.99 ± 0.11 GPa, and for the bulk measurements 2.03 ± 0.10 GPa. The basket-weave measurements are comparable to those previously obtained from grains in fully basket-weave samples in Task II (***Figure 32***), and the results from the globular-α grains are also comparable to those obtained in Task I for the Ti6242 chemistry. Additionally, the bulk indentation yield strength mean value is comparable to results from similar microstructures and alloy type reported in literature [282]. For this kind of comparison, a constrain factor of 2 is used to convert from indentation yield strength (0.2% offset) to tensile yield (0.2% offset) based on several previous studies that have used experimental and simulation methods to determine the most appropriate scaling factor [40, 46, 65, 66].

Table 9. *Volume fractions and mean indentation yield values from all the defined local states in the Ti6242 bimodal microstructure.*

Bimodal Microstructure Statistics		
Local State	**Vol. Fraction**	**Mean Y_{ind} [GPa]**
Basket-Weave	57.7 %	1.99
Φα = 0° - 10°	6.8 %	2.72
Φα = 10° - 20°	2.6 %	2.65
Φα = 20° - 30°	0.7 %	2.49
Φα = 30° - 40°	0.8 %	2.30
Φα = 40° - 50°	1.3 %	2.09
Φα = 50° - 60°	4.1 %	1.89
Φα = 60° - 70°	7.5 %	1.74
Φα = 70° - 80°	6.2 %	1.67
Φα = 80° - 90°	12.3 %	1.68

The overall volume fraction from each of the local states, and their respective indentation yield, are presented in ***Table 9***. By using a modified version of ***Eq. 16*** in which all 10 local states are terms in the linear relationship, the predicted effective indentation yield strength is calculated to be 1.98 ± 0.17 GPa. Although this estimation is slightly below the measured bulk indentation strength of the sample, it is higher than the ROM prediction using only the two original local states (basket-weave and primary-α phases) which estimates indentation yield at 1.92 ± 0.13. This is explained by the large number of experimental data points at the high declination regime (low indentation yield values), making the primary-α mean to shift downwards. These results show that incorporating the texture information and regression analysis from the experimental data, are necessary steps for a statistical estimation of the bulk indentation yield of the bimodal material by means of the rule of mixtures. This is especially true for microstructures where the behavior of one or both of the local states has a very strong dependence on orientation. Overall, we can say that rule of mixtures presents as a good method for estimating the indentation yield of bimodal microstructures, when the grain-scale and meso-scale measurements are accomplished using consistent protocols such as spherical indentation.

CHAPTER 6 Conclusions

i. The benefits of the spherical indentation stress-strain protocols for reliable and consistent grain-scale evaluation of mechanical responses of the α-phase component in a multitude of alpha-beta titanium alloys has been demonstrated in this work. The results allowed a systematic study of the effects of chemistry and crystal orientation on the indentation moduli and the indentation yield strengths measured in individual primary alpha grains in the studied alloys. For all alloys, the indentation properties parallel to the c-axis were higher than those measured perpendicular to the c-axis, with the differences significantly amplified for the indentation yield strength compared to the indentation moduli. This is attributed to the higher stiffness along the c-axis, and the need to activate pyramidal $\langle c + a \rangle$ slip in the indentation parallel to the c-axis. The results also clearly demonstrated that the indentation moduli reduced while the indentation yield strengths increased with the addition of the different alloying elements.

ii. It was seen that the substitutional additions generally impacted the pyramidal $\langle c + a \rangle$ slip resistance more than the prismatic $\langle a \rangle$ and basal slip resistances. It was generally observed that the slip resistances in the α-phase increased with an increase in the Al-equivalence, prompting the possibility that the equivalencies can be refined to specifically address CRSS values of the different slip families in α-Ti alloys. The data set obtained from the present study, largest of its kind aggregated to date, is shared with the broader materials

research community through the NIST Data Repository platform. https://hdl.handle.net/11256/989

iii. Rotationally invariant 2-point statistics and principal component analysis was shown successful as autonomously classifying grain-scale microstructures of fully basket-weave morphologies in titanium alloys. In addition to a classification based on volume fractions, this evaluation was able to capture morphology differences such as lath thickness and relative orientation/alignment of the laths. These protocols, in addition to the grain-level spherical indentation measurements, offer a one-of-a-kind opportunity for the construction of a structure-property linkage with a reduced number of microstructural features. In this case, parameters such as colony size factor, prior β-grain factor, and grain boundary-α fractions, are eliminated from the assessment, allowing for a more comprehensive relationship.

iv. Spherical indentation protocols was used at different length-scales on the same bimodal sample and the experimentally obtained results were used for the evaluation of the "Rule of Mixtures" in this material class. Regression analysis on the experimental data and texture information corrections were incorporated in the linear model, resulting in a predicted indentation yield strength laying within a 2.4% error from the effective measured property. Consistency in the experimental protocols across length-scales is of great value for future homogenization models and simulations on the deformation of dual-phase materials.

6.1 Future Work

- As expansion of this work, additionally chemistries are to be explored at all the length scales here evaluated. The inclusion of near-β and β-titanium alloys to the evaluation of globular-α and basket-weave grains will strengthen the construction of any future model or simulation.
- For the specific case of the basket-weave morphology assessment, the addition of more unique microstructures will also strengthen the prediction of properties. A wider range of microstructures could be obtained through Jominy bars that allow for controlled cooling rates and treatment conditions when the available material volume allows for such experimental procedure.
- The evaluation of aluminum equivalence factors as strength indicators is highly encouraged as it could offer important assistance in the process of incorporating chemical information as a variable in any model. Molybdenum equivalence values could be used for the case of near-β and β-titanium alloys where the presence of β-stabilizer alloying elements is more pronounced.
- The evaluation of bimodal microstructures with varying morphologies and volume fractions of the constituents is recommended for the development of a robust homogenization model based on multiresolution spherical indentation measurements.

REFERENCES

1. Collings, E.W., *The Physical Metallurgy of Titanium Alloys*. 1984: American Society for Metals.
2. Polmear, I., D. StJohn, J.-F. Nie, and M. Qian, *Light alloys: Metallurgy of the light metals*. Fifth ed. 2017, Netherlands: Elsevier Science, Butterworth-Heinemann.
3. Pilchak, A.L., J. Shank, J.C. Tucker, S. Srivatsa, P.N. Fagin, and S.L. Semiatin, *A dataset for the development, verification, and validation of microstructure-sensitive process models for near-alpha titanium alloys.* Integrating Materials and Manufacturing Innovation, 2016. **5**(1): p. 259-276.
4. Iskakov, A. and S.R. Kalidindi, *A Framework for the Systematic Design of Segmentation Workflows.* Integrating Materials and Manufacturing Innovation, 2020. **9**(1): p. 70-88.
5. Weaver, J.S., M.W. Priddy, D.L. McDowell, and S.R. Kalidindi, *On capturing the grain-scale elastic and plastic anisotropy of alpha-Ti with spherical nanoindentation and electron back-scattered diffraction.* Acta Materialia, 2016. **117**: p. 23-34.
6. Cecen, A., Y.C. Yabansu, and S.R. Kalidindi, *A new framework for rotationally invariant two-point spatial correlations in microstructure datasets.* Acta Materialia, 2018. **158**: p. 53-64.
7. Castillo, A.R., A. Venkatraman, and S.R. Kalidindi, *Mechanical Responses of Primary-α Ti Grains in Polycrystalline Samples: Part II—Bayesian Estimation of Crystal-Level Elastic-Plastic Mechanical Properties from Spherical Indentation Measurements.* Integrating Materials and Manufacturing Innovation, 2021. **10**(1): p. 99-114.
8. Ahmed, Y.M., K. S. M. Sahari, M. Ishak, and B.A. Khidhir, *Titanium and its Alloy.* International Journal of Science and Research (IJSR), 2012.
9. *Titanium Physical Metallurgy Processing and Applications*, ed. F.H. Froes. 2015, U.S.A.: ASM International.
10. Lakes, R., *Materials with Structural Hierarchy.* Nature, 1993. **361**: p. 511-515.
11. Weiss, I., E H. Froes, D. Eylon, and G.E. Welsch, *Modification of Alpha Morphology in Ti-6Al-4V by Thermomechanical Processing.* Metallurgical Transactions A, 1986. **17A**: p. 935–1946.
12. Williams, J. and E. Starke, *The role of thermomechanical processing in tailoring the properties of aluminum and titanium alloys.* Deformation, Processing and Structure, 1984: p. 1267-1276.
13. Oliver, W.C. and G.M. Pharr, *Measurement of Hardness and Elastic Modulus by Instrumented Indentation - Advances in Understanding and Refinements to Metrology.* Journal of Materials Research, 2014. **19**: p. 3-20.
14. Uchic, M.D. and D.M. Dimiduk, *A methodology to investigate size scale effects in crystalline plasticity using uniaxial compression testing.* Materials Science and Engineering: A, 2005. **400-401**: p. 268-278.
15. Sharpe, W.N., J.B. JR., K. Jackson, and G. Coles, *Tensile Testing of MEMS Materials - Recent Progress.* Journal of Materials Science, 2005. **38**: p. 4075-4079.
16. Wu, B., A. Heidelberg, and J.J. Boland, *Mechanical properties of ultrahigh-strength gold nanowires.* Nat Mater, 2005. **4**(7): p. 525-9.
17. Yu, Q., Z. W. Shan, J. Li, X. Huang, L. Xiao, J. Sun, and E. Ma, *Strong crystal size effect on deformation twinning.* Nature, 2010. **463**(7279): p. 335-338.

18. Xiao, L.I.N., Q. Yu, Q. Sun, and J. U. N. Sun, *Size effect on deformation mode in micron-sized Ti-5Al single crystal loaded along [2 1̄ 1] and [0001].* International Journal of Modern Physics, 2012. **24**(15-16): p. 2466-2471.
19. Sun, Q., Q. Guo, X. Yao, L. Xiao, J. R. Greer, and J. Sun, *Size effects in strength and plasticity of single-crystalline titanium micropillars with prismatic slip orientation.* Scripta Materialia, 2011. **65**(6): p. 473-476.
20. Jun, T.S., G. Sernicola, F.P.E. Dunne, and T.B. Britton, *Local deformation mechanisms of two-phase Ti alloy.* Materials Science and Engineering A, 2016. **649**: p. 39-47.
21. Zhang, Z., T.-S. Jun, T.B. Britton, and F.P.E. Dunne, *Intrinsic anisotropy of strain rate sensitivity in single crystal alpha titanium.* Acta Materialia, 2016. **118**: p. 317-330.
22. Kiener, D., C. Motz, M. Rester, M. Jenko, and G. Dehm, *FIB Damage of Cu and possible consequences for miniaturized mechanical tests.* Materials Science and Engineering: A, 2007. **459**(1-2): p. 262-272.
23. Chandler, H., *Hardness testing*. 1999: ASM international.
24. Miyake, K., S. Fujisawa, A. Korenaga, T. Ishida, and S. Sasaki, *The Effect of Pile-Up and Contact Area on Hardness Test by Nanoindentation.* Japanese Journal of Applied Physics, 2004. **43**(7B): p. 4602-4605.
25. McElhaney, K., J.J. Vlassak, and W.D. Nix, *Determination of indenter tip geometry and indentation contact area for depth-sensing indentation experiments.* Journal of Materials research, 1998. **13**(5): p. 1300-1306.
26. Zhang, P., S.X. Li, and Z.F. Zhang, *General relationship between strength and hardness.* Materials Science and Engineering: A, 2011. **529**: p. 62-73.
27. Alcala, J., A. Giannakopoulos, and S. Suresh, *Continuous measurements of load-penetration curves with spherical microindenters and the estimation of mechanical properties.* Journal of Materials Research, 1998. **13**(5): p. 1390-1400.
28. Giannakopoulos, A.E. and S. Suresh, *Determination of Elastoplastic Properties by Instrumented Sharp Indentation.* Scripta Materialia, 1999. **40**: p. 1191-1198.
29. Bucaille, J.L., S. Stauss, E. Felder, and J. Michler, *Determination of plastic properties of metals by instrumented indentation using different sharp indenters.* Acta Materialia, 2003. **51**(6): p. 1663-1678.
30. Morris, J.R., H. Bei, G.M. Pharr, and E.P. George, *Size effects and stochastic behavior of nanoindentation pop in.* Physical Review Letters, 2011. **106**(16).
31. Nix, W.D. and H. Gao, *Indentation size effects in crystalline materials a law for strain gradient plasticity.* Journal of the Mechanics and Physics of Solids, 1998. **46**: p. 411.425.
32. Ma, X., F. Li, Z. Sun, J. Hou, J. Li, and X. Fang, *Strain rate dependence of the indentation size effect in Ti–10V–2Fe–3Al alloy.* Materials Science and Technology, 2019. **35**(9): p. 1107-1113.
33. Demir, E., D. Raabe, N. Zaafarani, and S. Zaefferer, *Investigation of the indentation size effect through the measurement of the geometrically necessary dislocations beneath small indents of different depths using EBSD tomography.* Acta Materialia, 2009. **57**(2): p. 559-569.
34. Pathak, S. and S.R. Kalidindi, *Spherical nanoindentation stress–strain curves.* Materials Science and Engineering: R: Reports, 2015. **91**: p. 1-36.
35. Leclerc, N., A. Khosravani, S. Hashemi, D.B. Miracle, and S.R. Kalidindi, *Correlation of Measured Load-Displacement Curves in Small Punch Tests with Tensile Stress-Strain Curves.* Acta Materialia, 2020. **204**.

36. Kalidindi, S.R. and S. Pathak, *Determination of the effective zero-point and the extraction of spherical nanoindentation stress–strain curves.* Acta Materialia, 2008. **56**(14): p. 3523-3532.
37. Hertz, H., D.E. Jones, and G.A. Schott, *Miscellaneous papers*. 1896: Macmillan and Company.
38. Khosravani, A., A. Cecen, and S.R. Kalidindi, *Development of high throughput assays for establishing process-structure-property linkages in multiphase polycrystalline metals: Application to dual-phase steels.* Acta Materialia, 2017. **123**: p. 55-69.
39. Khosravani, A., L. Morsdorf, C.C. Tasan, and S.R. Kalidindi, *Multiresolution mechanical characterization of hierarchical materials: Spherical nanoindentation on martensitic Fe-Ni-C steels.* Acta Materialia, 2018. **153**: p. 257-269.
40. Weaver, J.S., A. Khosravani, A. Castillo, and S.R. Kalidindi, *High throughput exploration of process-property linkages in Al-6061 using instrumented spherical microindentation and microstructurally graded samples.* Integrating Materials and Manufacturing Innovation, 2016. **5**(1): p. 192-211.
41. Weaver, J.S. and S.R. Kalidindi, *Mechanical characterization of Ti-6Al-4V titanium alloy at multiple length scales using spherical indentation stress-strain measurements.* Materials & Design, 2016. **111**: p. 463-472.
42. Kalidindi, S.R., S. Mohan, and A. Rossi, *Mechanical characterization of mesoscale interfaces using indentation techniques.* Journal of the Minerals, Metals & Materials Society, 2016. **69**(1): p. 22-29.
43. Kalidindi, S.R. and S.J. Vachhani, *Mechanical characterization of grain boundaries using nanoindentation.* Current Opinion in Solid State and Materials Science, 2014. **18**(4): p. 196-204.
44. Pathak, S., J. Michler, K. Wasmer, and S.R. Kalidindi, *Studying grain boundary regions in polycrystalline materials using spherical nano-indentation and orientation imaging microscopy.* Journal of Materials Science, 2011. **47**(2): p. 815-823.
45. Rossi, A., A. Castillo, C. Przybyla, and S.R. Kalidindi, *Study of Local Mechanical Responses in an Epoxy–Carbon Fiber Laminate Composite Using Spherical Indentation Stress–Strain Protocols.* Integrating Materials and Manufacturing Innovation, 2019. **8**(4): p. 495-508.
46. Mohan, S., N. Millan-Espitia, M. Yao, N.V. Steenberge, and S.R. Kalidindi, *Critical Evaluation of Spherical Indentation Stress-Strain Protocols for the Estimation of the Yield Strengths of Steels.* Experimental Mechanics, 2021. **61**: p. 641-652.
47. Khosravani, A., N. Thadhani, and S.R. Kalidindi, *Microstructure Quantification and Multiresolution Mechanical Characterization of Ti-Based Bulk Metallic Glass-Matrix Composites.* Jom, 2021.
48. Khosravani, A., C.M. Caliendo, and S.R. Kalidindi, *New insights into the microstructural changes during the processing of dual-phase steels from multiresolution spherical indentation stress–strain protocols.* Metals, 2019. **10**(1).
49. Patel, D.K. and S.R. Kalidindi, *Estimating the slip resistance from spherical nanoindentation and orientation measurements in polycrystalline samples of cubic metals.* International Journal of Plasticity, 2017. **92**: p. 19-30.
50. Patel, D.K., H.F. Al-Harbi, and S.R. Kalidindi, *Extracting single-crystal elastic constants from polycrystalline samples using spherical nanoindentation and orientation measurements.* Acta Materialia, 2014. **79**: p. 108-116.
51. Castillo, A. and S.R. Kalidindi, *A bayesian framework for the estimation of the single crystal elastic parameters from spherical indentation stress-strain measurements.* Frontiers in Materials, 2019. **6**.

52. Chudoba, T., N. Schwarzer, and F. Richter, *Determination of Elastic Properties of Thin Films by Indentation Measurements With a Spherical Indenter.* Surface and Coatings Technology, 2000. **127**: p. 9-17.
53. Linss, V., N. Schwarzer, T. Chudoba, M. Karniychuk, and F. Richter, *Mechanical properties of a graded B–C–N sputtered coating with varying Young's modulus: deposition, theoretical modelling and nanoindentation.* Surface and Coatings Technology, 2005. **195**(2-3): p. 287-297.
54. Richter, F., M. Herrmann, F. Molnar, T. Chudoba, N. Schwarzer, M. Keunecke, K. Bewilogua, X.W. Zhang, H.G. Boyen, and P. Ziemann, *Substrate influence in Young's modulus determination of thin films by indentation methods: Cubic boron nitride as an example.* Surface and Coatings Technology, 2006. **201**(6): p. 3577-3587.
55. Chudoba, T., M. Griepentrog, A. Dück, D. Schneider, and F. Richter, *Young's modulus measurements on ultra-thin coatings.* Journal of Materials Research, 2004. **19**(1): p. 301-314.
56. Ullner, C., *Requirement of a Robust Method for the Precise Determination of the Contact Point in the Depth Sensing Hardness Test.* Measurement, 2000. **27**: p. 43-51.
57. Grau, P., G. Berg, W. Fränzel, and H. Meinhard, *Recording hardness testing. Problems of measurement at small indentation depths.* physica status solidi (a), 1994. **146**(1): p. 537-548.
58. Liang, Y.-H., Y. Arai, K. Ozasa, M. Ohashi, and E. Tsuchida, *Simultaneous measurement of nanoprobe indentation force and photoluminescence of InGaAs/GaAs quantum dots and its simulation.* Physica E: Low-dimensional Systems and Nanostructures, 2007. **36**(1): p. 1-11.
59. Fischer-Cripps, A.C., *Critical review of analysis and interpretation of nanoindentation test data.* Surface and Coatings Technology, 2006. **200**(14-15): p. 4153-4165.
60. Lim, Y.Y. and M. Munawar Chaudhri, *Indentation of elastic solids with a rigid Vickers pyramidal indenter.* Mechanics of Materials, 2006. **38**(12): p. 1213-1228.
61. Pathak, S., J. Shaffer, and S. Kalidindi, *Determination of an effective zero-point and extraction of indentation stress–strain curves without the continuous stiffness measurement signal.* Scripta Materialia, 2009. **60**(6): p. 439-442.
62. Vachhani, S.J. and S.R. Kalidindi, *Grain-scale measurement of slip resistances in aluminum polycrystals using spherical nanoindentation.* Acta Materialia, 2015. **90**: p. 27-36.
63. Pathak, S., S.R. Kalidindi, and N.A. Mara, *Investigations of orientation and length scale effects on micromechanical responses in polycrystalline zirconium using spherical nanoindentation.* Scripta Materialia, 2016. **113**: p. 241-245.
64. Iskakov, A., Y.C. Yabansu, S. Rajagopalan, A. Kapustina, and S.R. Kalidindi, *Application of spherical indentation and the materials knowledge system framework to establishing microstructure-yield strength linkages from carbon steel scoops excised from high-temperature exposed components.* Acta Materialia, 2018. **144**: p. 758-767.
65. Patel, D.K. and S.R. Kalidindi, *Correlation of spherical nanoindentation stress-strain curves to simple compression stress-strain curves for elastic-plastic isotropic materials using finite element models.* Acta Materialia, 2016. **112**: p. 295-302.
66. Donohue, B.R., A. Ambrus, and S.R. Kalidindi, *Critical evaluation of the indentation data analyses methods for the extraction of isotropic uniaxial mechanical properties using finite element models.* Acta Materialia, 2012. **60**(9): p. 3943-3952.
67. Grau, P., G. Berg, W. Franzel, and H. Meinhar, *Problems of measurement at small indentation depths.* Physica Status Solidi, 1994. **146**: p. 537-548.

68. Li, X. and B. Bhushan, *A review of nanoindentation continuous stiffness measurement technique and its applications.* Materials Characterization, 2001. **48**: p. 11-36.
69. Vachhani, S.J., R.D. Doherty, and S.R. Kalidindi, *Effect of the continuous stiffness measurement on the mechanical properties extracted using spherical nanoindentation.* Acta Materialia, 2013. **61**(10): p. 3744-3751.
70. Pharr, G.M., W.C. Oliver, and F.R. Brotzen, *On the generality of the relationship among contact stiffness, contact area, and elastic modulus during indentation.* Journal of Materials Research Society, 1992. **7**(3): p. 613-617.
71. Herrmann, K., N.M. Jennett, W. Wegener, J. Meneve, K. Hasche, and R. Seemann, *Progress in determination of the area function of indenters used for nanoindentation.* Thin Solid Films, 2000. **377-378**: p. 394-400.
72. Moody, N.R., W.W. Gweberich, N. Burnham, and S.P. Baker. *Fundamentals of nanoindentation and nanotribology*. in *No. CONF-980405*. 1998. Warrendale, PA, USA: Materials Research Society.
73. Field, J.S. and M.V. Swain, *A simple predictive model for spherical indentation.* Journal of Materials Research, 2011. **8**(2): p. 297-306.
74. Field, J.S. and M.V. Swain, *Determining the mechanical properties of small volumes of material from submicrometer spherical indentations.* Journal of Materials Research, 2011. **10**(1): p. 101-112.
75. Pathak, S., D. Stojakovic, and S.R. Kalidindi, *Measurement of the local mechanical properties in polycrystalline samples using spherical nanoindentation and orientation imaging microscopy.* Acta Materialia, 2009. **57**(10): p. 3020-3028.
76. Vachhani, S.J., R.D. Doherty, and S.R. Kalidindi, *Studies of grain boundary regions in deformed polycrystalline aluminum using spherical nanoindentation.* International Journal of Plasticity, 2016. **81**: p. 87-101.
77. Pathak, S., J.L. Riesterer, S.R. Kalidindi, and J. Michler, *Understanding pop-ins in spherical nanoindentation.* Applied Physics Letters, 2014. **105**(16).
78. Sudharshan Phani, P., K.E. Johanns, E.P. George, and G.M. Pharr, *A stochastic model for the size dependence of spherical indentation pop-in.* Journal of Materials Research, 2013. **28**(19): p. 2728-2739.
79. Wang, M.G. and A.H.W. Ngan, *Indentation strain burst phenomenon induced by grain boundaries in niobium.* Journal of Materials Research, 2011. **19**(8): p. 2478-2486.
80. Lorenz, D., A. Zeckzer, U. Hilpert, P. Grau, H. Johansen, and H.S. Leipner, *Pop-in effect as homogeneous nucleation of dislocations during nanoindentation.* Physical Review B, 2003. **67**(17).
81. Ahn, T.H., C.S. Oh, K. Lee, E.P. George, and H.N. Han, *Relationship between yield point phenomena and the nanoindentation pop-in behavior of steel.* Journal of Materials Research, 2011. **27**(1): p. 39-44.
82. Lutjering, G., *Property optimization through microstructural control in titanium and aluminum alloys.* Materials Science and Engineering, 1999. **A263**: p. 117-126.
83. Filip, R., K. Kubiak, W. Ziaja, and J. Sieniawski, *The effect of microstructure on the mechanical properties of two-phase titanium alloys.* Journal of Materials Processing Technology, 2003. **133**: p. 84–89.
84. Patel, A., O. Kravchenko, and I. Manas-Zloczower, *Effect of Curing Rate on the Microstructure and Macroscopic Properties of Epoxy Fiberglass Composites.* Polymers (Basel), 2018. **10**(2).

85. Nagarajan, B., D. Kumar, Z. Fan, and S. Castagne, *Effect of deep cold rolling on mechanical properties and microstructure of nickel-based superalloys.* Materials Science and Engineering: A, 2018. **728**: p. 196-207.
86. Pierman, A.P., O. Bouaziz, T. Pardoen, P.J. Jacques, and L. Brassart, *The influence of microstructure and composition on the plastic behaviour of dual-phase steels.* Acta Materialia, 2014. **73**: p. 298-311.
87. Uchic, M.D., M.A. Groeber, D.M. Dimiduk, and J.P. Simmons, *3D microstructural characterization of nickel superalloys via serial-sectioning using a dual beam FIB-SEM.* Scripta Materialia, 2006. **55**(1): p. 23-28.
88. Santofimia, M.J., L. Zhao, R. Petrov, and J. Sietsma, *Characterization of the microstructure obtained by the quenching and partitioning process in a low-carbon steel.* Materials Characterization, 2008. **59**(12): p. 1758-1764.
89. Otto, F., A. Dlouhý, K.G. Pradeep, M. Kuběnová, D. Raabe, G. Eggeler, and E.P. George, *Decomposition of the single-phase high-entropy alloy CrMnFeCoNi after prolonged anneals at intermediate temperatures.* Acta Materialia, 2016. **112**: p. 40-52.
90. Collins, P.C., B. Welk, T. Searles, J. Tiley, J.C. Russ, and H.L. Fraser, *Development of methods for the quantification of microstructural features in α+β-processed α/β titanium alloys.* Materials Science and Engineering: A, 2009. **508**(1-2): p. 174-182.
91. Paredes-Orta, C.A., J.D. Mendiola-Santibañez, F. Manriquez-Guerrero, and I.R. Terol-Villalobos, *Method for grain size determination in carbon steels based on the ultimate opening.* Measurement, 2019. **133**: p. 193-207.
92. Smith, T.M., P. Bonacuse, J. Sosa, M. Kulis, and L. Evans, *A quantifiable and automated volume fraction characterization technique for secondary and tertiary γ′ precipitates in Ni-based superalloys.* Materials Characterization, 2018. **140**: p. 86-94.
93. Payton, E.J., P.J. Phillips, and M.J. Mills, *Semi-automated characterization of the γ′ phase in Ni-based superalloys via high-resolution backscatter imaging.* Materials Science and Engineering: A, 2010. **527**(10-11): p. 2684-2692.
94. Yabansu, Y.C., P. Steinmetz, J. Hötzer, S.R. Kalidindi, and B. Nestler, *Extraction of reduced-order process-structure linkages from phase-field simulations.* Acta Materialia, 2017. **124**: p. 182-194.
95. Paulson, N.H., M.W. Priddy, D.L. McDowell, and S.R. Kalidindi, *Reduced-order structure-property linkages for polycrystalline microstructures based on 2-point statistics.* Acta Materialia, 2017. **129**: p. 428-438.
96. Montes de Oca Zapiain, D., E. Popova, F. Abdeljawad, J.W. Foulk, S.R. Kalidindi, and H. Lim, *Reduced-Order Microstructure-Sensitive Models for Damage Initiation in Two-Phase Composites.* Integrating Materials and Manufacturing Innovation, 2018. **7**(3): p. 97-115.
97. Zhou, W., R. Apkarian, Z.L. Wang, and D. Joy, *Fundamentals of scanning electron microscopy (SEM)*, in *Scanning microscopy for nanotechnology*. 2006, Springer. p. 1-40.
98. Behrooz, A., J.-C. Tseng, J. Meganck, and M. Hopkinton, *Image resolution in MicroCT: principles and characterization of the quantum FX and quantum GX systems.* Preclin. Vivo Imaging, 2016: p. 1-5.
99. Kalidindi, S.R., *Hierarchical materials informatics: novel analytics for materials data*. 2015: Elsevier.
100. Niezgoda, S.R., D.M. Turner, D.T. Fullwood, and S.R. Kalidindi, *Optimized structure based representative volume element sets reflecting the ensemble-averaged 2-point statistics.* Acta Materialia, 2010. **58**(13): p. 4432-4445.

101. Campbell, A., P. Murray, E. Yakushina, S. Marshall, and W. Ion, *New methods for automatic quantification of microstructural features using digital image processing.* Materials & Design, 2018. **141**: p. 395-406.
102. Payton, E., P. Phillips, and M. Mills, *Semi-automated characterization of the γ′ phase in Ni-based superalloys via high-resolution backscatter imaging.* Materials Science and Engineering: A, 2010. **527**(10-11): p. 2684-2692.
103. Higham, D.J. and N.J. Higham, *MATLAB guide* Philadelphia, PA: SIAM, 2016. **(Vol. 150)**.
104. Perez, F., B.E. Granger, and J.D. Hunter, *Python: an ecosystem for scientific computing.* Computing in Science & Engineering, 2010. **13**(2): p. 13-21.
105. Yang, D. and Z. Liu, *Quantification of microstructural features and prediction of mechanical properties of a dual-phase Ti-6Al-4V alloy.* Materials, 2016. **9**(8): p. 628.
106. Peregrina-Barreto, H., I. Terol-Villalobos, J. Rangel-Magdaleno, A. Herrera-Navarro, L. Morales-Hernández, and F. Manríquez-Guerrero, *Automatic grain size determination in microstructures using image processing.* Measurement, 2013. **46**(1): p. 249-258.
107. Barrett, J.F. and N. Keat, *Artifacts in CT: recognition and avoidance.* Radiographics, 2004. **24**(6): p. 1679-1691.
108. Ishitani, T., C. Kamiya, and M. Sato, *Influence of random noise on the contrast-to-gradient image resolution in scanning electron microscopy.* Journal of electron microscopy, 2005. **54**(2): p. 85-97.
109. Likar, B., J.a. Maintz, M.A. Viergever, and F. Pernus, *Retrospective shading correction based on entropy minimization.* Journal of Microscopy, 2000. **197**(Pt 3): p. 285-295.
110. Sosa, J.M., D.E. Huber, B. Welk, and H.L. Fraser, *Development and application of MIPAR™: a novel software package for two-and three-dimensional microstructural characterization.* Integrating Materials and Manufacturing Innovation, 2014. **3**(1): p. 123-140.
111. Davies, E.R., *Computer and machine vision: theory, algorithms, practicalities*. 2012: Academic Press.
112. Verma, R. and J. Ali, *A comparative study of various types of image noise and efficient noise removal techniques.* International Journal of advanced research in computer science and software engineering, 2013. **3**(10).
113. Van De Ville, D., M. Nachtegael, D. Van der Weken, E.E. Kerre, W. Philips, and I. Lemahieu, *Noise reduction by fuzzy image filtering.* IEEE transactions on fuzzy systems, 2003. **11**(4): p. 429-436.
114. Sarode, M.V. and P.R. Deshmukh, *Reduction of speckle noise and image enhancement of images using filtering technique.* International Journal of Advancements in Technology, 2011. **2**(1): p. 30-38.
115. Peters, R.A., *A new algorithm for image noise reduction using mathematical morphology.* IEEE transactions on Image Processing, 1995. **4**(5): p. 554-568.
116. Buades, A., B. Coll, and J.-M. Morel. *A non-local algorithm for image denoising*. in *2005 IEEE Computer Society Conference on Computer Vision and Pattern Recognition (CVPR'05)*. 2005. IEEE.
117. Gonzalez, R.C. and R.E. Woods, *Digital Image Processing*. 2 ed. 2002, Englewood Cliffs, NJ: Prentice-Hall.
118. Zuiderveld, K., *Contrast limited adaptive histogram equalization.* Graphics gems, 1994: p. 474-485.
119. Kalidindi, S.R., S.R. Niezgoda, G. Landi, S. Vachhani, and T. Fast, *A novel framework for building materials knowledge systems.* Computers, Materials, & Continua, 2010. **17**(2): p. 103-125.

120. Dutta, S., K. Barat, A. Das, S.K. Das, A. Shukla, and H. Roy, *Characterization of micrographs and fractographs of Cu-strengthened HSLA steel using image texture analysis.* Measurement, 2014. **47**: p. 130-144.
121. Gupta, S., A. Panda, R. Naskar, D.K. Mishra, and S. Pal, *Processing and refinement of steel microstructure images for assisting in computerized heat treatment of plain carbon steel.* Journal of Electronic Imaging, 2017. **26**(6): p. 063010.
122. Papa, J.P., V.H.C. De Albuquerque, A.X. Falcão, and J.M.R. Tavares. *Fast automatic microstructural segmentation of ferrous alloy samples using optimum-path forest*. in *International Symposium Computational Modeling of Objects Represented in Images*. 2010. Springer.
123. Moon, K.H., A.C. Falchetto, and J.H. Jeong, *Microstructural analysis of asphalt mixtures using digital image processing techniques.* Canadian Journal of Civil Engineering, 2014. **41**(1): p. 74-86.
124. Shafei, B. and G. Steidl, *Segmentation of images with separating layers by fuzzy c-means and convex optimization.* Journal of visual communication and image representation, 2012. **23**(4): p. 611-621.
125. Otsu, N., *A threshold selection method from gray-level histograms.* IEEE transactions on systems, man, and cybernetics, 1979. **9**(1): p. 62-66.
126. Tsai, D.-M. and Y.-H. Chen, *A fast histogram-clustering approach for multi-level thresholding.* Pattern Recognition Letters, 1992. **13**(4): p. 245-252.
127. Kapur, J.N., P.K. Sahoo, and A.K. Wong, *A new method for gray-level picture thresholding using the entropy of the histogram.* Computer vision, graphics, and image processing, 1985. **29**(3): p. 273-285.
128. Bradley, D. and G. Roth, *Adaptive thresholding using the integral image.* Journal of graphics tools, 2007. **12**(2): p. 13-21.
129. Serra, J., *Image analysis and mathematical morphol-ogy.* 1982.
130. Soille, P., *Morphological image analysis: principles and applications*. 2013: Springer Science & Business Media.
131. Paulic, M., D. Mocnik, M. Ficko, J. Balic, T. Irgolic, and S. Klancnik, *Intelligent system for prediction of mechanical properties of material based on metallographic images.* Tehnički vjesnik, 2015. **22**(6): p. 1419-1424.
132. Han, Y., C. Lai, B. Wang, and H. Gu, *Segmenting images with complex textures by using hybrid algorithm.* Journal of Electronic Imaging, 2019. **28**(1): p. 013030.
133. Klein, T., M. Schachermayer, F. Mendez-Martin, T. Schöberl, B. Rashkova, H. Clemens, and S. Mayer, *Carbon distribution in multi-phase γ-TiAl based alloys and its influence on mechanical properties and phase formation.* Acta Materialia, 2015. **94**: p. 205-213.
134. Potgieter, J. and M. Cortie, *Determination of the microstructure and alloy element distribution in experimental duplex stainless steels.* Materials characterization, 1991. **26**(3): p. 155-165.
135. Carey, J.P., *Handbook of Advances in Braided Composite Materials.* Woodhead Publishing is an Imprint of Elsevier, 2017(72): p. 3.
136. Joseph, C., C. Persson, and M.H. Colliander, *Influence of heat treatment on the microstructure and tensile properties of Ni-base superalloy Haynes 282.* Materials Science and Engineering: A, 2017. **679**: p. 520-530.
137. *ASTM E562-19e1, Standard Test Method for Determining Volume Fraction by Systematic Manual Point Count*. 2019, ASTM International: West Conshohocken, PA.

138. Fullwood, D.T., S.R. Niezgoda, B.L. Adams, and S.R. Kalidindi, *Microstructure sensitive design for performance optimization.* Progress in Materials Science, 2010. **55**(6): p. 477-562.
139. Altschuh, P., Y.C. Yabansu, J. Hötzer, M. Selzer, B. Nestler, and S.R. Kalidindi, *Data science approaches for microstructure quantification and feature identification in porous membranes.* Journal of Membrane Science, 2017. **540**: p. 88-97.
140. Cecen, A., T. Fast, and S.R. Kalidindi, *Versatile algorithms for the computation of 2-point spatial correlations in quantifying material structure.* Integrating Materials and Manufacturing Innovation, 2016. **5**(1): p. 1-15.
141. Yang, Z., Y.C. Yabansu, R. Al-Bahrani, W.-k. Liao, A.N. Choudhary, S.R. Kalidindi, and A. Agrawal, *Deep learning approaches for mining structure-property linkages in high contrast composites from simulation datasets.* Computational Materials Science, 2018. **151**: p. 278-287.
142. Cecen, A., H. Dai, Y.C. Yabansu, S.R. Kalidindi, and L. Song, *Material structure-property linkages using three-dimensional convolutional neural networks.* Acta Materialia, 2018. **146**: p. 76-84.
143. Olson, G.B., *Computational design of hierarchically structured materials.* Science, 1997. **277**(5330): p. 1237-1242.
144. Li, D.S., M.A. Tschopp, M. Khaleel, and X. Sun, *Comparison of reconstructed spatial microstructure images using different statistical descriptors.* Computational Materials Science, 2012. **51**(1): p. 437-444.
145. Baniassadi, M., S. Ahzi, H. Garmestani, D. Ruch, and Y. Remond, *New approximate solution for N-point correlation functions for heterogeneous materials.* Journal of the Mechanics and Physics of Solids, 2012. **60**(1): p. 104-119.
146. Torquato, S. and H. Haslach Jr, *Random heterogeneous materials: microstructure and macroscopic properties.* Appl. Mech. Rev., 2002. **55**(4): p. B62-B63.
147. Moore, A.W., A.J. Connolly, C. Genovese, A. Gray, L. Grone, N. Kanidoris II, R.C. Nichol, J. Schneider, A.S. Szalay, and I. Szapudi, *Fast algorithms and efficient statistics: N-point correlation functions*, in *Mining the Sky*. 2001, Springer. p. 71-82.
148. Gray, A.G. and A.W. Moore, *N-Body'problems in statistical learning.* Advances in neural information processing systems, 2001: p. 521-527.
149. Kröner, E., J. Gittus, and J. Zarka, *Modelling Small Deformations of Polycrystals.* Elsevier Applied Science Publisher, 1986. **229**.
150. Kröner, E., *Bounds for effective elastic moduli of disordered materials.* Journal of the Mechanics and Physics of Solids, 1977. **25**(2): p. 137-155.
151. Gupta, A., A. Cecen, S. Goyal, A.K. Singh, and S.R. Kalidindi, *Structure–property linkages using a data science approach: Application to a non-metallic inclusion/steel composite system.* Acta Materialia, 2015. **91**: p. 239-254.
152. Gomberg, J.A., A.J. Medford, and S.R. Kalidindi, *Extracting knowledge from molecular mechanics simulations of grain boundaries using machine learning.* Acta Materialia, 2017. **133**: p. 100-108.
153. Niezgoda, S.R., D.T. Fullwood, and S.R. Kalidindi, *Delineation of the space of 2-point correlations in a composite material system.* Acta Materialia, 2008. **56**(18): p. 5285-5292.
154. Zambaldi, C., Y. Yang, T.R. Bieler, and D. Raabe, *Orientation informed nanoindentation of α-titanium: Indentation pileup in hexagonal metals deforming by prismatic slip.* Journal of Materials Research, 2012. **27**(1): p. 356-367.

155. Britton, T.B., H. Liang, F.P.E. Dunne, and A.J. Wilkinson, *The effect of crystal orientation on the indentation response of commercially pure titanium: experiments and simulations.* Proceedings of the Royal Society A: Mathematical, Physical and Engineering Sciences, 2009. **466**(2115): p. 695-719.
156. MacKay, D.J., *Bayesian interpolation.* Neural computation, 1992. **4**(3): p. 415-447.
157. MacKay, D.J., *Hyperparameters: optimize, or integrate out?*, in *Maximum entropy and bayesian methods*. 1996, Springer. p. 43-59.
158. Kalidindi, S.R., C.A. Bronkhorst, and L. Anand, *Crystallographic texture evolution in bulk deformation processing of FCC metals.* Journal of the Mechanics and Physics of Solids, 1992. **40**(3): p. 537-569.
159. Kalidindi, S. and S. Schoenfeld, *On the prediction of yield surfaces by the crystal plasticity models for fcc polycrystals.* Materials Science and Engineering: A, 2000. **293**(1-2): p. 120-129.
160. Bachu, V. and S.R. Kalidindi, *On the accuracy of the predictions of texture evolution by the finite element technique for fcc polycrystals.* Materials Science and Engineering: A, 1998. **257**(1): p. 108-117.
161. Needleman, A., R. Asaro, J. Lemonds, and D. Peirce, *Finite element analysis of crystalline solids.* Computer Methods in Applied Mechanics and Engineering, 1985. **52**(1-3): p. 689-708.
162. Chib, S. and E. Greenberg, *Understanding the metropolis-hastings algorithm.* The american statistician, 1995. **49**(4): p. 327-335.
163. Haario, H., E. Saksman, and J. Tamminen, *Componentwise adaptation for high dimensional MCMC.* Computational Statistics, 2005. **20**(2): p. 265-273.
164. Roberts, G.O. and J.S. Rosenthal, *Examples of adaptive MCMC.* Journal of computational and graphical statistics, 2009. **18**(2): p. 349-367.
165. Lutjering, G., J. C. Williams, and A. Gysler, *Microstructure and Mechanical Properties of Titanium Alloys*. 2000: World Scientific.
166. Gammon, L.M., R. D. Briggs, J. M. Packard, K. W. Batson, R. Boyer, and C.W. Domb, *Metallography and microstructures of titanium and its alloys.* ASM Handbook: Metallography and Microstructures, 2004. **9**: p. 899-917.
167. Sieniawski, J., W. Ziaja, K. Kubiak, and M. Motyk, *Microstructure and Mechanical Properties of High Strength Two-Phase Titanium Alloys*, in *Titanium Alloys - Advances in Properties Control*. 2013.
168. Blenkinsop, P., W.J. Evans, and H.M. Flower, *Titanium'95: Science and Technology: Proceedings of the Eighth World Conference on Titanium Held at the International Convention Centre, Birmingham, UK, 22-26 October 1995*. 1996: Institute of Materials.
169. Wu, X., S. R. Kalidindi, C. Necker, and A.A. Salem, *Modeling anisotropic stress-strain response and crystallographic texture evolution in α-titanium during large plastic deformation using Taylor-Type Models: Influence of initial texture and purity.* Metallurgical and Materials Transactions A, 2008. **39**(12): p. 3046-3054.
170. Zhang, Z., Tea-Sung Jun, T. B. Britton, and F.P.E. Dunne, *Determination of Ti-6242 α and β slip properties using micro-pillar test and computational crystal plasticity.* Journal of the Mechanics and Physics of Solids, 2016. **95**: p. 393-410.
171. Baudoin, P., T. Hama, and H. Takuda, *Influence of critical resolved shear stress ratios on the response of a commercially pure titanium oligocrystal: Crystal plasticity simulations and experiment.* International Journal of Plasticity, 2019. **115**: p. 111-131.
172. Paton, N.E., J. C. Williams, and G.P. Rauscher, *The Deformation of α-phase Titanium.* Titanium science and technology, 1973.

173. Dunst, D. and H. Mecking, *Analysis of experimental and theoretical rolling textures of two-phase titanium alloys.* Zeitschrift fur Metallkunde, 1996. **87**(6): p. 498-507.
174. Wu, X., S. R. Kalidindi, C. Necker, and A. Salem, *Prediction of crystallographic texture evolution and anisotropic stress–strain curves during large plastic strains in high purity α-titanium using a Taylor-Type crystal plasticity model.* Acta Materialia, 2007. **55**(2): p. 423-432.
175. Medina Perilla, J.A. and J. Gil Sevillano, *Two-dimensional sections of the yield locus of a Ti-6%Al-4%V alloy with a strong transverse-type crystallographic a-texture.* Material Science and Engineering, 1995. **A201**: p. 103-110.
176. Fundenberger, J.J., M. J. Philippe, F. Wagner, and C. Esling, *Modeling and prediction of mechanical properties for materials with hexagonal symmetry (zinc, titanium and zirconium alloys).* Acta Materialia, 1997. **45**: p. 4041-4055.
177. Lebensohn, R.A. and G. R. Canova, *A self-consistent approach for modeling texture development of two-phase polycrystals application to titanium alloys.* Acta Materialia, 1997. **45**: p. 3687-3694.
178. Churchman, A.T., *Preparation of single crystals of titanium and their mode of deformation.* Nature, 1953. **171**(4355).
179. Liebertzs, J., S. Stahrs, and S. Haussuh, *Growth and properties of single crystals of FeTi.* Kristall und Technik, 1980. **15**(11): p. 1257-1260.
180. Cass, T.R., R. W. Quinn, and W.R. Spencer, *Growth of hexagonal titanium and titanium-alumium single crystals.* Journal of Crystal Growth, 1968. **2**: p. 413-416.
181. Wang, F.E., A. M. Syeles, W. L. Clark, and W. J. Buehler, *Growth of TiNi single crystals by a modified strain-anneal technique.* Journal of Applied Physics, 1964. **35**(12): p. 3620-3620.
182. Gong, J. and A.J. Wilkinson, *Micro-cantilever testing of ⟨a⟩ prismatic slip in commercially pure Ti.* Philosophical Magazine, 2011. **91**(7-9): p. 1137-1149.
183. Gong, J. and A.J. Wilkinson, *Anisotropy in the plastic flow properties of single-crystal α titanium determined from micro-cantilever beams.* Acta Materialia, 2009. **57**(19): p. 5693-5705.
184. Mante, F.K., G.R. Baran, and B. Lucas, *Nanoindentation studies of titanium single crystals.* Biomaterials, 1999. **20**: p. 1051-1055.
185. Merson, E., R. Brydson, and A. Brown, *The effect of crystallographic orientation on the mechanical properties of titanium.* Journal of Physics: Conference Series, 2008. **126**.
186. Sagadevan, S. and P. Murugasen, *Novel analysis on the influence of tip radius and shape of the nanoindenter on the hardness of materials.* Procedia Materials Science, 2014. **6**: p. 1871-1878.
187. Pathak, S., D. Stojakovic, R. Doherty, and S.R. Kalidindi, *Importance of surface preparation on the nano-indentation stress-strain curves measured in metals.* Materials Research Society, 2009. **24**(3): p. 1142-1155.
188. Taljat, B. and G.M. Pharr, *Development of pile-up during spherical indentation of elastic–plastic solids.* International Journal of Solids and Structures, 2004. **41**(14): p. 3891-3904.
189. Michalske, T.A. and J.E. Houston, *Dislocation nucleation at nano-scale mechanical contacts.* Acta Materialia, 1997. **46**: p. 391-396.
190. *ASTM E1409-13, Standard Test Method for Determination of Oxygen and Nitrogen in Titanium and Titanium Alloys by Inert Gas Fusion*, in *ASTM International*. 2013: West Conshohocken, PA.
191. Collins, E.W. and H.L. Gegel, *Physical principles of solid solution strengthening in alloys*, in *Physics of Solid Solution Strengthening*. 1975, Springer, Boston, MA. p. 147-182.

192. Tessier, F., *Determining the nitrogen content in (oxy)nitride materials.* Materials, 2018. **11**(8).
193. Bunge, H.-J., *Texture analysis in materials science: Mathematical methods*. 2013, United Kingdom: Elsevier Science.
194. Viswanathan, G.B., E. Lee, D.M. Maher, S. Banerjee, and H.L. Fraser, *Direct observations and analyses of dislocation substructures in the α phase of an α/β Ti-alloy formed by nanoindentation.* Acta Materialia, 2005. **53**(19): p. 5101-5115.
195. Kwon, J., M.C. Brandes, P. Sudharshan Phani, A.P. Pilchak, Y.F. Gao, E.P. George, G.M. Pharr, and M.J. Mills, *Characterization of deformation anisotropies in an α-Ti alloy by nanoindentation and electron microscopy.* Acta Materialia, 2013. **61**(13): p. 4743-4756.
196. *The Science, Technology and Application of Titanium: Proceedings of an International Conference organized by the Institute of Metals, the Metallurgical Society of AIME, and the American Society for Metals in Association with the Japan Institute of Metals and the Academy of Sciences, U.S.S.R.*, ed. R.I. Jaffee and N.E. Promisel. 2013: Elsevier Science.
197. J.C. Williams, R.G. Baggerly, and N.E. Paton, *Deformation behavior of HCP Ti-Al alloy single crystals.* Metallurgical and Materials Transactions, 2002. **33 A**: p. 837-850.
198. Zambaldi, C., C. Zehnder, and D. Raabe, *Orientation dependent deformation by slip and twinning in magnesium during single crystal indentation.* Acta Materialia, 2015. **91**: p. 267-288.
199. Li, T.L., Y.F. Gao, H. Bei, and E.P. George, *Indentation Schmid factor and orientation dependence of nanoindentation pop-in behavior of NiAl single crystals.* Journal of the Mechanics and Physics of Solids, 2011. **59**(6): p. 1147-1162.
200. Fast, T., M. Knezevic, and S.R. Kalidindi, *Application of microstructure sensitive design to structural components produced from hexagonal polycrystalline metals.* Computational Materials Science, 2008. **43**(2): p. 374-383.
201. Proust, G. and S. Kalidindi, *Procedures for construction of anisotropic elastic–plastic property closures for face-centered cubic polycrystals using first-order bounding relations.* Journal of the Mechanics and Physics of Solids, 2006. **54**(8): p. 1744-1762.
202. Wu, X., G. Proust, M. Knezevic, and S.R. Kalidindi, *Elastic–plastic property closures for hexagonal close-packed polycrystalline metals using first-order bounding theories.* Acta Materialia, 2007. **55**(8): p. 2729-2737.
203. Paulson, N.H., M.W. Priddy, D.L. McDowell, and S.R. Kalidindi, *Reduced-order microstructure-sensitive protocols to rank-order the transition fatigue resistance of polycrystalline microstructures.* International Journal of Fatigue, 2019. **119**: p. 1-10.
204. Paulson, N.H., M.W. Priddy, D.L. McDowell, and S.R. Kalidindi, *Data-driven reduced-order models for rank-ordering the high cycle fatigue performance of polycrystalline microstructures.* Materials & Design, 2018. **154**: p. 170-183.
205. Sakai, T. and M.E. Fine, *Basal Slip of Ti-Al Single Crystals.* Scripta Metallurgica, 1974. **8**: p. 545-548.
206. Sakai, T. and M.E. Fine, *Failure of Schmid's law in Ti-Al alloys for prismatic slip.* Scripta Metallurgica, 1974. **8**: p. 541-544.
207. Sakai, T. and M.E. Fine, *Plastic-deformation of Ti–Al single-crystals in prismatic slip.* Acta Metallurgica, 1973. **22**: p. 1359-1372.
208. Sasano, H. and H. Kimura, *Solid-solution strengthening of alpha titanium alloys*, in *Titanium 80: Science and Technology*, H. Kimura and O. Izumi, Editors. 1980, The Metallurgical Society of AIME. p. 1147-1154.
209. Rosenberg, H.W., *Titanium alloying in theory and practice*, in *The science, technology and application of titanium*. 1970, Pergamon. p. 851-859.

210. Weiss, I. and S.L. Semiatin, *Thermomechanical processing of alpha titanium alloys - an overview.* Materials Science and Engineering: A, 1999. **263**(2): p. 243–256.
211. Weiss, I. and S.L. Semiatin, *Thermomechanical processing of beta titanium alloys - an overview.* Materials Science and Engineering: A, 1998. **243**(1-2): p. 46-65.
212. Yulana, Y., W. Weiqi, L. Fengli, L. Weiqing, and Z. Yongqiang, *The effect of aluminum equivalent and molybdenum equivalent on the mechanical properties of high strength and high toughness titanium alloys.* Materials Science Forums, 2009. **618, 619**: p. 169-172.
213. Huang, X. and A.A. Pelegri, *Mechanical characterization of thin film materials with nanoindentation measurements and FE analysis.* Journal of Composite Materials, 2006. **40**(15): p. 1393-1407.
214. Lucchini, R., D. Carnelli, M. Ponzoni, E. Bertarelli, D. Gastaldi, and P. Vena, *Role of damage mechanics in nanoindentation of lamellar bone at multiple sizes: experiments and numerical modeling.* Journal of the mechanical behavior of biomedical materials, 2011. **4**(8): p. 1852-1863.
215. Priddy, M.W., N.H. Paulson, S.R. Kalidindi, and D.L. McDowell, *Strategies for rapid parametric assessment of microstructure-sensitive fatigue for HCP polycrystals.* International Journal of Fatigue, 2017. **104**: p. 231-242.
216. ABAQUS, U., *Version 6.14-1.* Dassault Systémes Simulia Corp., Providence, RI, 2014. **4**.
217. Fisher, E. and C. Renken, *Single-crystal elastic moduli and the hcp→ bcc transformation in Ti, Zr, and Hf.* Physical review, 1964. **135**(2A): p. A482.
218. Kim, J.-Y., V. Yakovlev, and S. Rokhlin. *Line-focus acoustic microscopy of Ti-6242 α/β single colony: determination of elastic constants*. in *AIP Conference Proceedings*. 2002. American Institute of Physics.
219. Heldmann, A., M. Hoelzel, M. Hofmann, W. Gan, W.W. Schmahl, E. Griesshaber, T. Hansen, N. Schell, and W. Petry, *Diffraction-based determination of single-crystal elastic constants of polycrystalline titanium alloys.* Journal of applied crystallography, 2019. **52**(5): p. 1144-1156.
220. Blackburn, M. and J. Williams, *A comparison of phase transformations in three commercial titanium alloys(Phase transformations in commercial titanium alloys compared for mechanical properties, emphasizing decomposition of metastable beta phases on quenching, aging or deformation).* ASM Transactions Quarterly, 1967. **60**: p. 373-383.
221. International, A., *Titanium: A Technical Guide. 2nd Edition*. 2000: ASM International.
222. Welsch, G., R. Boyer, and E.W. Collings, *Materials Properties Handbook: Titanium Alloys*. 1993: ASM International.
223. Semiatin, S., V. Seetharaman, and I. Weiss, *Advances in science and technology of Ti alloy processing.* Metals and Materials Society, The Minerals, 1997.
224. Collins, E.W., H.L. Gegel, and J.C. Ho, *Solid solution strengthening and fundamental design of titanium alloys*. 1972: National Technical Information Service U. S. Department of Commerce.
225. Tseng, K.-K., C-C. Juan, S. Tso, H-C. Chen, C-W. Tsai, and J.-W. Yeh, *Effects of Mo, Nb, Ta, Ti, and Zr on mechanical properties of equiatomic Hf-Mo-Nb-Ta-Ti-Zr alloys.* Entropy, 2018. **21**(1).
226. Conrad, H., B. Meester, M. Doner, and K. Okazaki, *Strengthening of alpha titanium by the interstitial solutes C, N, and O.* Plenum Press, New York, 1975.

227. Wilson, N.C., K. McGregor, M.A. Gibson, and S.P. Russo, *The effect of dopant incorporation on the elastic properties of Ti metal.* Modelling and Simulation in Materials Science and Engineering, 2015. **23**(1).
228. Ivasishin, O. and P. Markovsky, *Enhancing the mechanical properties of titanium alloys with rapid heat treatment.* JOM, 1996. **48**(7): p. 48-52.
229. Boyer, R.R. and D.R. Wallem, *Microstructure/Property Relationships of Titanium Alloys*, in *TMS*, S. Ankem and J. Hall, Editors. 1994: Warrendale, PA. p. 125-32.
230. Chakrabarti, A.K. and J. Chesnutt, *Microstructure Fracture Toughness and Fatigue Crack Growth Rate in Titanium Alloys.* Denver, 1987: p. 1987.
231. Gupta, A., R.K. Khatirkar, A. Kumar, and M.S. Parihar, *Investigations on the effect of heating temperature and cooling rate on evolution of microstructure in an α + β titanium alloy.* Journal of Materials Research, 2018. **33**(8): p. 946-957.
232. Wang, Y., J. Zhao, S. Dai, F. Chen, X. Yu, and Y. Zhang, *Influence of cold rolling and ageing treatment on microstructure and mechanical properties of Ti-30Nb-5Ta-6Zr alloy.* J Mech Behav Biomed Mater, 2013. **27**: p. 33-42.
233. Liang, S.X., L.X. Yin, R.J. Jiang, X.Y. Zhang, M.Z. Ma, and R.P. Liu, *Strengthening mechanism of two-phase titanium alloys with basketweave microstructure.* Journal of Alloys and Compounds, 2014. **603**: p. 42-47.
234. Kar, S., T. Searles, E. Lee, G.B. Viswanathan, J. Tiley, R. Banerjee, and H.L. Fraser, *Modeling the Tensile Properties in Processed alpha-beta Ti alloys.* Metallurgical and Materials Transactions A, 2006. **37A**: p. 559-566.
235. Tiley, J., T. Searles, E. Lee, S. Kar, R. Banerjee, J.C. Russ, and H.L. Fraser, *Quantification of microstructural features in α/β titanium alloys.* Materials Science and Engineering: A, 2004. **372**(1-2): p. 191-198.
236. Nag, S., R. Banerjee, and H.L. Fraser, *A novel combinatorial approach for understanding microstructural evolution and its relationship to mechanical properties in metallic biomaterials.* Acta Biomater, 2007. **3**(3): p. 369-76.
237. Pellissier, G., *Stereology and quantitative metallography*. 1972: ASTM International.
238. *ASTM E112-96, Standard Test Methods for Determining Average Grain Size*. 2013, ASTM International: West Conshohocken, PA.
239. *ASTM E930-99, Standard Test Methods for Estimating the Largest Grain Observed in a Metallographic Section (ALA Grain Size)*. 1999, ASTM International: West Conshohocken, PA.
240. *ASTM E1382-97(2015), Standard Test Methods for Determining Average Grain Size Using Semiautomatic and Automatic Image Analysis*. 2015, ASTM International: West Conshohocken, PA.
241. Tschanz, S.A., P.H. Burri, and E.R. Weibel, *A simple Tool for Stereological Assessment of Digital Images: The STEPanizer.* Journal of Microscopy, 2011. **243**(1): p. 47-59.
242. Groeber, M.A., B.K. Haley, M.D. Uchic, D.M. Dimiduk, and S. Ghosh, *3D reconstruction and characterization of polycrystalline microstructures using a FIB–SEM system.* Materials Characterization, 2006. **57**(4-5): p. 259-273.
243. Millan-Espitia, N., S. Mohan, A.L. Pilchak, and S.R. Kalidindi, *Mechanical Responses of Primary-α Ti Grains in Polycrystalline Samples: Part I—Measurements of Spherical Indentation Stress–Strain Curves.* Integrating Materials and Manufacturing Innovation, 2021. **10**(1): p. 82-98.
244. Stephen R. Niezgoda, Anand K. Kanjarla, and Surya R. Kalidindi, *Novel microstructure quantification framework for databasing, visualization, and analysis of microstructure data.* Integrating Materials and Manufacturing Innovation, 2013. **2**(3).

245. Niezgoda, S.R., Y.C. Yabansu, and S.R. Kalidindi, *Understanding and visualizing microstructure and microstructure variance as a stochastic process.* Acta Materialia, 2011. **59**(16): p. 6387-6400.
246. S. R. Kalidindi, S. R. Niezgoda, and A.A. Salem, *Microstructure informatics using higher-order statistics and efficient data-mining protocols.* JOM, 2011. **63**(4): p. 34-41.
247. Fullwood, D.T., S.R. Niezgoda, and S.R. Kalidindi, *Microstructure reconstructions from 2-point statistics using phase-recovery algorithms.* Acta Materialia, 2008. **56**(5): p. 942-948.
248. Choudhury, A., Y.C. Yabansu, S.R. Kalidindi, and A. Dennstedt, *Quantification and classification of microstructures in ternary eutectic alloys using 2-point spatial correlations and principal component analyses.* Acta Materialia, 2016. **110**: p. 131-141.
249. Jun, T.-S., D.E.J. Armstrong, and T.B. Britton, *A nanoindentation investigation of local strain rate sensitivity in dual-phase Ti alloys.* Journal of Alloys and Compounds, 2016. **672**: p. 282-291.
250. Hémery, S. and P. Villechaise, *Comparison of slip system activation in Ti-6Al-2Sn-4Zr-2Mo and Ti-6Al-2Sn-4Zr-6Mo under tensile, fatigue and dwell-fatigue loadings.* Materials Science and Engineering: A, 2017. **697**: p. 177-183.
251. *The Math Works, Inc. MATLAB*. 2021a; Available from: https://www.mathworks.com/help/images/ref/adaptthresh.html.
252. Attallah, M.M., S. Zabeen, R.J. Cernik, and M. Preuss, *Comparative determination of the α/β phase fraction in α+β-titanium alloys using X-ray diffraction and electron microscopy.* Materials Characterization, 2009. **60**(11): p. 1248-1256.
253. Banerjee, S. and P. Mukhopadhyay, *Phase transformations: examples from titanium and zirconium alloys*. 2010: Elsevier.
254. Burgers, W.G., *On the process of transition of the cubic-body-centered modification into the hexagonal-close-packed modification of zirconium.* Physical Review B, 1934. **1**(7-12): p. 561-586.
255. Furuhara, T., A.M. Dalley, and H.I. Aaronson, *Interfacial structure of grain boundary α allotriomorphs in a hypoeutectoid TiCr alloy.* Scripta Metallurgica, 1988. **22**(9): p. 1509-1514.
256. Banerjee, D., A. Gogia, T. Nandi, and V. Joshi, *A new ordered orthorhombic phase in a Ti3Al・Nb alloy.* Acta Metallurgica, 1988. **36**(4): p. 871-882.
257. Perovic, V. and G. Weatherly, *The β to α transformation in a Zr-2.5 wt% Nb alloy.* Acta Metallurgica, 1989. **37**(3): p. 813-821.
258. Potter, D., *The structure, morphology and orientation relationship of V3N in α-vanadium.* Journal of the Less Common Metals, 1973. **31**(2): p. 299-309.
259. A. S. Beranger, X. Feaugas, and M. Clavel, *Low Cycle Fatigue Behavior of an a-b Titanium Alloy Ti6246.* Materials Science and Engineering,, 1993. **A 172**: p. 31-41.
260. Bache, M.R., L. Germain, T. Jackson, and A.R.M. Walker. *Mechanical and Texture Evaluations of Ti 6246 as a Dwell Fatigue Tolerant Alloy*. in *11th world conference on titanium*. 2007.
261. Attallah, M.M., M. Preuss, C. Booncharoen, A. Steuwer, J.E. Daniels, D.J. Hughes, C. Dungey, and G.J. Baxter, *Microstructural and Residual Stress Development due to Inertia Friction Welding in Ti-6246.* Metallurgical and Materials Transactions A, 2012. **43**(9): p. 3149-3161.
262. Lütjering, G., *Influence of processing on microstructure and mechanical properties of (α+β) titanium alloys.* Materials Science and Engineering: A, 1998. **243**(1-2): p. 32-45.

263. Smelser, R., J. Swedlow, and J. Williams, *Analysis of Local Stresses and Strains in Ti-6A1-4V Widmanstätten α+ β Microstructures*, in *Toughness and Fracture Behavior of Titanium*. 1978, ASTM International.
264. Jinoch, J., S. Ankem, and H. Margolin, *Calculations of stress-strain curve and stress and strain distributions for an α-β Ti・8Mn alloy.* Materials Science and Engineering, 1978. **34**(3): p. 203-211.
265. Ankem, S. and H. Margolin, *The role of elastic interaction stresses on the onset of plastic flow for oriented two ductile phase structures.* Metallurgical Transactions A, 1980. **11**(6): p. 963.
266. Ankem, S. and H. Margolin, *Finite element method (FEM) calculations of stress-strain behavior of alpha-beta Ti-Mn alloys: part I. Stress-strain relations.* Metallurgical Transactions A, 1982. **13**(4): p. 595-601.
267. Hayden, H. and S. Floreen, *The influence of martensite and ferrite on the properties of two-phase stainless steels having microduplex structures.* Metallurgical Transactions, 1970. **1**(7): p. 1955-1959.
268. Yegneswaran, A. and K. Tangri, *Investigation of the early stages of deformation of two phase copper-aluminum alloys.* Metallurgical Transactions A, 1983. **14**(11): p. 2407-2413.
269. Yegneswaran, A. and K. Tangri, *Deformation behaviour of two phase materials: Cu-Al system.* Metal science, 1984. **18**(3): p. 161-168.
270. Davies, R., *The deformation behavior of a vanadium-strengthened dual phase steel.* Metallurgical Transactions A, 1978. **9**(1): p. 41-52.
271. Davies, R., *The mechanical properties of zero-carbon ferrite-plus-martensite structures.* Metallurgical Transactions A, 1978. **9**(3): p. 451-455.
272. Davies, R., *Influence of martensite composition and content on the properties of dual phase steels.* Metallurgical Transactions A, 1978. **9**(5): p. 671-679.
273. Ogden, H., F. Holden, and R. Jaffee, *Effect of Alpha Sohites on the Heat-Treatment Response Of Ti-Mn Alloys.* JOM, 1955. **7**(1): p. 105-112.
274. Holden, F., H. Ogden, and R. Jaffee, *Heat treatment and mechanical properties of Ti-Mo alloys.* JOM, 1956. **8**(10): p. 1388-1393.
275. Tseng, D. and K. Tangri, *Deformation behavior of duplex Zircaloy-4-oxygen alloys.* Metallurgical transactions A, 1982. **13**(6): p. 1077-1082.
276. Pilchak, A., W. Porter, and R. John, *Room temperature fracture processes of a near-α titanium alloy following elevated temperature exposure.* Journal of Materials Science, 2012. **47**(20): p. 7235-7253.
277. Voigt, W., *Ueber die Beziehung zwischen den beiden Elasticitätsconstanten isotroper Körper.* Annalen der physik, 1889. **274**(12): p. 573-587.
278. Cho, K. and J. Gurland, *The law of mixtures applied to the plastic deformation of two-phase alloys of coarse microstructures.* Metallurgical Transactions A, 1988. **19**(8): p. 2027-2040.
279. Reuß, A., *Berechnung der fließgrenze von mischkristallen auf grund der plastizitätsbedingung für einkristalle.* ZAMM-Journal of Applied Mathematics and Mechanics/Zeitschrift für Angewandte Mathematik und Mechanik, 1929. **9**(1): p. 49-58.
280. Tamura, Y.T. and H. Ozawa. in *Third International Conference on Strength of Metals and Alloys*. 1973. Institute of Metal and Iron and Steel Institute, London.
281. Ankem, S. and H. Margolin, *A rationalization of stress-strain behavior of two-ductile phase alloys.* Metallurgical Transactions A, 1986. **17**(12): p. 2209-2226.

282. Villechaise, P., B. Max, J. Alexis, C. Larignon, S. Perusin, B. Appolaire, P. Castany, M. Dehmas, C. Delaunay, J. Delfosse, A. Denquin, E. Gautier, L. Germain, N. Gey, T. Gloriant, J.Y. Hascoët, S. Hémery, Y. Millet, D. Monceau, F. Pettinari-Sturmel, M. Piellard, F. Prima, and B. Viguier, *Titanium alloy Ti-6242 for high temperature structural application. Static and dynamic mechanical properties and impact of ageing.* MATEC Web of Conferences, 2020. **321**.